STATE OF THE CLIMATE IN 2024

GLOBAL OCEANS

G. C. Johnson and R. Lumpkin, Eds.

Special Online Supplement to the *Bulletin of the American Meteorological Society* Vol. 106, No. 8, August, 2025

https://doi.org/10.1175/BAMS-D-25-0074.1

Corresponding author: Gregory C. Johnson / gcj3@uw.edu

STATE OF THE CLIMATE IN 2024
Global Oceans

Editors

Jessica Blunden
James Reagan

Chapter Editors

Anthony Arguez
Josh Blannin
Peter Bissolli
Kyle R. Clem
Howard J. Diamond
Matthew L. Druckenmiller
Robert J. H. Dunn
Catherine Ganter
Nadine Gobron
Gregory C. Johnson
Rick Lumpkin
Rodney Martinez
Ademe Mekonnen
Twila A. Moon
Gary A. Morris
Marilyn N. Raphael
Carl J. Schreck III
Laura Stevens
Richard L. Thoman
Kate M. Willett
Zhiwei Zhu

Technical Editor

Lukas Noguchi

BAMS Special Editor for Climate

Timothy DelSole

American Meteorological Society

Cover Credit:
NEMO float after deployment in sea ice from the German icebreaker Polarstern Bremerhaven. Photo courtesy of the Argo Program (https://argo.ucsd.edu)

How to cite this document:
Global Oceans is one chapter from the *State of the Climate in 2024* annual report and is available from https://doi.org/10.1175/BAMS-D-25-0074.1. Compiled by NOAA's National Centers for Environmental Information, *State of the Climate in 2024* is based on contributions from scientists from around the world. It provides a detailed update on global climate indicators, notable weather events, and other data collected by environmental monitoring stations and instruments located on land, water, ice, and in space. The full report is available from https://doi.org/10.1175/2025BAMSStateoftheClimate.1.

Citing the complete report:
Blunden, J. and J. Reagan, Eds., 2025: "State of the Climate in 2024". Bull. Amer. Meteor. Soc., 106 (8), Si–S513 https://doi.org/10.1175/2025BAMSStateoftheClimate.1.

Citing this chapter:
Johnson, G. C. and R. L. Lumpkin, Eds., 2025: Global Oceans [in "State of the Climate in 2024"]. Bull. Amer. Meteor. Soc., 106 (8), S173–S232, https://doi.org/10.1175/BAMS-D-25-0074.1.

Citing a section (example):
Lumpkin, R., M. Le Hénaff, F. P. Tuchen, and R. C. Perez, 2025: Surface currents [in "State of the Climate in 2024"]. Bull. Amer. Meteor. Soc., 106 (8), S204–S207, https://doi.org/10.1175/BAMS-D-25-0074.1.

Editor and Author Affiliations (alphabetical by name)

Beckley, Brian, KBR, Inc., Greenbelt, Maryland; NASA Goddard Space Flight Center, Greenbelt, Maryland

Bellas-Manley, Ashley, Colorado Center for Astrodynamics Research, Cooperative Institute for Research in Environmental Sciences, University of Colorado Boulder, Boulder, Colorado

Carter, Brendan R., Cooperative Institute for Climate, Ocean, and Ecosystem Studies, University of Washington, Seattle, Washington; NOAA/OAR Pacific Marine Environmental Laboratory, Seattle, Washington

Cetinić, Ivona, NASA Goddard Space Flight Center, Greenbelt, Maryland; Universities Space Research Association, Columbia, Maryland

Chambers, Don P., College of Marine Science, University of South Florida, St. Petersburg, Florida

Chan, Duo, School of Ocean and Earth Science, University of Southampton, Southampton, United Kingdom

Cheng, Lijing, International Center for Climate and Environment Sciences, Institute of Atmospheric Physics, Chinese Academy of Sciences, Beijing, China

Dong, Shenfu, NOAA/OAR Atlantic Oceanographic and Meteorological Laboratory, Miami, Florida

Feely, Richard A., NOAA/OAR Pacific Marine Environmental Laboratory, Seattle, Washington

Franz, Bryan A., NASA Goddard Space Flight Center, Greenbelt, Maryland

Gao, Meng, NASA Goddard Space Flight Center, Greenbelt, Maryland; Science Systems and Applications, Inc., Lanham, Maryland

Garg, Jay, ADNET Systems, Inc., Hampton, Virginia

Giglio, Donata, Department of Atmospheric and Oceanic Sciences, University of Colorado Boulder, Boulder, Colorado

Graham, Garrett, North Carolina Institute for Climate Studies, North Carolina State University, Asheville, North Carolina

Hamlington, Benjamin D., Center for Coastal Physical Oceanography, Old Dominion University, Norfolk, Virginia

Hobbs, Will, Australian Antarctic Program Partnership, Institute for Marine and Antarctic Studies, University of Tasmania, Hobart, Tasmania; Australian Research Council Centre of Excellence for Climate Extremes, University of Tasmania, Hobart, Tasmania

Hu, Zeng-Zhen, NOAA/NWS National Centers for Environmental Prediction Climate Prediction Center, College Park, Maryland

Huang, Boyin, NOAA/NESDIS National Centers for Environmental Information, Asheville, North Carolina

Jersild, Annika, Earth System Science Interdisciplinary Center/Cooperative Institute for Satellite Earth System Studies, University of Maryland, College Park, Maryland

Jevrejeva, Svetlana, National Oceanography Centre, Liverpool, United Kingdom

Johns, William E., Rosenstiel School of Marine and Atmospheric Science, University of Miami, Miami, Florida

Johnson, Gregory C., School of Oceanography, University of Washington, Seattle, Washington ; NOAA/OAR Pacific Marine Environmental Laboratory, Seattle, Washington (retired)

Killick, Rachel. E., Met Office Hadley Center, Exeter, United Kingdom

Kuusela, Mikael, Department of Statistics and Data Science, Carnegie Mellon University, Pittsburg, Pennsylvania

Lamont, Tarron, Department of Forestry, Fisheries and the Environment, Cape Town, South Africa

Landerer, F. W., Jet Propulsion Laboratory, California Institute of Technology, Pasadena, California

Landschützer, Peter, Flanders Marine Institute, InnovOcean Campus, Ostend, Belgium

Le Hénaff, Matthieu, NOAA/OAR Atlantic Oceanographic and Meteorological Laboratory, Miami, Florida

Leuliette, Eric, NOAA/NWS NCWCP Laboratory for Satellite Altimetry, College Park, Maryland

Locarnini, Ricardo, NOAA/NESDIS National Centers for Environmental Information, Silver Spring, Maryland

Lumpkin, Rick, NOAA/OAR Atlantic Oceanographic and Meteorological Laboratory, Miami, Florida

Lyman, John M., Cooperative Institute for Marine and Atmospheric Research, University of Hawai'i, Honolulu, Hawai'i; NOAA/OAR Pacific Marine Environmental Laboratory, Seattle, Washington

Merrifield, Mark A., Integrative Oceanography Division, Scripps Institution of Oceanography, La Jolla, California

Mishonov, Alexey, Earth System Science Interdisciplinary Center/Cooperative Institute for Satellite Earth System Studies, University of Maryland, College Park, Maryland; NOAA/NESDIS National Centers for Environmental Information, Silver Spring, Maryland

Mitchum, Gary T., College of Marine Science, University of South Florida, St. Petersburg, Florida

Moat, Ben I., National Oceanography Centre, Southampton, United Kingdom

Nerem, R. Steven, Colorado Center for Astrodynamics Research, Cooperative Institute for Research in Environmental Sciences, University of Colorado Boulder, Boulder, Colorado

Oe, Mitsuho, Japan Meteorological Agency, Tokyo, Japan

Perez, Renellys C., NOAA/OAR Atlantic Oceanographic and Meteorological Laboratory, Miami, Florida

Reagan, James, NOAA/NESDIS National Centers for Environmental Information, Silver Spring, Maryland

Schlegal, Robert W., Laboratoire d'Océanographie de Villefranche, Sorbonne Université, Villefranche-sur-mer, France

Schmid, Claudia, NOAA/OAR Atlantic Oceanographic and Meteorological Laboratory, Miami, Florida

Smeed, David A., National Oceanography Centre, Southampton, United Kingdom

Smith, Ryan H., NOAA/OAR Atlantic Oceanographic and Meteorological Laboratory, Miami, Florida

Speich, Sabrina, Laboratoire de Météorologie Dynamique, Institut Pierre-Simon Laplace, ENS-PSL, Paris, France

Stackhouse, Jr., Paul W., NASA Langley Research Center, Hampton, Virginia

Sukianto, Thea, Department of Statistics and Data Science, Carnegie Mellon University, Pittsburg, Pennsylvania

Sweet, William, NOAA/NOS Center for Operational Oceanographic Products and Services, Silver Spring, Maryland

Thompson, Philip R., Cooperative Institute for Marine and Atmospheric Research, University of Hawai'i, Honolulu, Hawai'i

Triñanes, Joaquin A., Laboratory of Systems, Technological Research Institute, Universidad de Santiago de Compostela, Campus Universitario Sur, Santiago de Compostela, Spain; Cooperative Institute for Marine and Atmospheric Studies, Rosenstiel School of Marine and Atmospheric Science, University of Miami, Miami, Florida; NOAA/OAR Atlantic Oceanographic and Meteorological Laboratory, Miami, Florida

Tuchen, Franz Philip, Cooperative Institute for Marine and Atmospheric Studies, University of Miami, Miami, Florida; NOAA/OAR Atlantic Oceanographic and Meteorological Laboratory, Miami, Florida

Volkov, Denis L., Cooperative Institute for Marine and Atmospheric Studies, University of Miami, Miami, Florida; NOAA/OAR Atlantic Oceanographic and Meteorological Laboratory, Miami, Florida

Wanninkhof, Rik, NOAA/OAR Atlantic Oceanographic and Meteorological Laboratory, Miami, Florida

Weller, Robert A., Department of Physical Oceanography, Woods Hole Oceanographic Institution, Woods Hole, Massachusetts

Westberry, Toby K., Oregon State University, Corvallis, Oregon

Widlansky, Matthew J., Cooperative Institute for Marine and Atmospheric Research, University of Hawai'i, Honolulu, Hawai'i

Editor and Author Affiliations (continued)

Willis, Joshua K., Jet Propulsion Laboratory, California Institute of Technology, Pasadena, California

Yin, Xungang, NOAA/NESDIS National Centers for Environmental Information, Asheville, North Carolina

Yu, Lisan, Department of Physical Oceanography, Woods Hole Oceanographic Institution, Woods Hole, Massachusetts

Zhang, Huai-Min, NOAA/NESDIS National Centers for Environmental Information, Asheville, North Carolina

Editorial and Production Team

Allen, Jessicca, Graphics Support, Cooperative Institute for Satellite Earth System Studies, North Carolina State University, Asheville, North Carolina

Camper, Amy V., Graphics Support, Innovative Consulting and Management Services, LLC, NOAA/NESDIS National Centers for Environmental Information, Asheville, North Carolina

Carroll, Lauren, Content Team Lead, Communications and Outreach, NOAA/NESDIS National Centers for Environmental Information, Asheville, North Carolina

Haley, Bridgette O., Graphics Support, NOAA/NESDIS National Centers for Environmental Information, Asheville, North Carolina

Love-Brotak, S. Elizabeth, Lead Graphics Production, NOAA/NESDIS National Centers for Environmental Information, Asheville, North Carolina

Ohlmann, Laura, Technical Editor, Innovative Consulting and Management Services, LLC, NOAA/NESDIS National Centers for Environmental Information, Asheville, North Carolina

Noguchi, Lukas, Technical Editor, Innovative Consulting and Management Services, LLC, NOAA/NESDIS National Centers for Environmental Information, Asheville, North Carolina

Riddle, Deborah B., Graphics Support, NOAA/NESDIS National Centers for Environmental Information, Asheville, North Carolina

Veasey, Sara W., Visual Communications Team Lead, Communications and Outreach, NOAA/NESDIS National Centers for Environmental Information, Asheville, North Carolina

3. Table of Contents

3. GLOBAL OCEANS

G. C. Johnson and R. Lumpkin, Eds.

a. Overview

—G. C. Johnson and R. Lumpkin

El Niño ebbed in early 2024, reaching neutral status in May and crossing the threshold into La Niña conditions in December. The global average annual sea surface temperature was 0.06°C above the previous record set in 2023. Marine heatwaves in 2024 were, as in 2023, more widespread, long-lived, and severe than in previous years. From 2023 to 2024, ocean heat content from 0 dbar to 2000 dbar increased at a rate equivalent to ~1.5 W m^{-2} of heat applied over the ocean surface, and global sea level increased by 4.6 (±1.4) mm, both reaching record-high levels in 2024. Maps of air–sea flux data estimate that the oceans absorbed carbon at a rate of ~2.7 Pg C yr^{-1} in 2024, which was below the 2014–23 average of ~3.7 Pg C yr^{-1}.

In the Pacific Ocean, given the shift from a strong El Niño to weak La Niña conditions, surface currents across the equatorial Pacific in 2024 were strongly anomalously westward, and sea surface temperatures, sea surface salinities, 0 m–2000 m ocean heat content, and sea level all decreased sharply in the eastern equatorial Pacific from 2023 to 2024. Fluxes of carbon dioxide from ocean to atmosphere were anomalously lower than average during 2024 off Peru and out to about 140°W, likely owing to the El Niño in the first few months of the year. As in 2023, chlorophyll-*a* anomalies in 2024 were low in a wedge in the central and eastern equatorial Pacific, but high just outside that wedge. The Pacific Decadal Oscillation has been in a negative phase since 2020, with sea surface temperature, ocean heat content, and sea surface height values in the center of the North Pacific basin all higher than average, along with relatively lower values around the edges in 2024. A persistent 2020–24 poleward shift in the Kuroshio extension also continued to be evident east of Japan in both ocean heat content and zonal surface current anomalies.

In the Indian Ocean, sea surface temperature, ocean heat content, and sea level were all above average in 2024 across much of the basin, except for a large patch of below-average ocean heat content along 20°S–30°S. Surface currents near the equator were anomalously eastward. Surface salinities were primarily strongly anomalously fresh north of about 12°S in 2024, consistent with anomalously high freshwater input (precipitation minus evaporation) from the atmosphere to the ocean in the region. Chlorophyll-*a* anomalies were quite negative offshore of Somalia and Oman, as well as northeast of Madagascar, but generally positive in the rest of the basin. There was also a prominent ridge of high sea level and ocean heat content extending eastward from Africa just north of Madagascar, which was associated with anomalous westward surface currents on its northern flank.

In the Atlantic, sea surface temperature, ocean heat content, and sea level were all well above average across much of the basin in 2024, with some below-average values of ocean heat content in a patch extending from east of Cape Cod to about 55°N, 25°W. A band of anomalously eastward surface current and above-average ocean heat content directly north of a band of anomalously westward surface current along the Gulf Stream extension west of 70°W is consistent with an anomalous northward shift of the axis of this current in 2024. Sea surface salinity was anomalously high in much of the basin but anomalously low around the Intertropical Convergence Zone and in the Labrador Sea. Updates of time series of the Atlantic meridional overturning circulation at two latitudes revealed little evidence of a trend over the past few decades.

Arctic and Southern Ocean conditions for 2024 are discussed in detail in Chapter 5 and Chapter 6, respectively.

b. Sea surface temperatures

— X. Yin, R. W. Schlegel, B. Huang, D. Chan, G. Graham, Z.-Z. Hu, and H.-M. Zhang

1. INTRODUCTION

The state of sea surface temperatures (SSTs) in the global ocean is described and analyzed using four gridded SST datasets: the Daily OISST (DOISSTv2.1; Huang et al. 2021), ERSSTv5 (Huang et al. 2017), the Hadley Centre Sea Surface Temperature Dataset version 4 (HadSST.4.0.1.0; Kennedy et al. 2019), and Dynamically Consistent ENsemble of Temperature (DCENTv1.0; Chan et al. 2024). DOISSTv2.1 is blended from in situ observations and satellite measurements, covering the period from 1981 to present. It is a high-resolution SST product providing daily mean SSTs, analyzed on 0.25-degree latitude–longitude grids. The latter three products are in situ observation-based SST products, containing monthly mean SST data covering the period from preindustrial times (1854 for ERSSTv5, 1850 for HadSST.4.0.1.0 and DCENTv1.0) to present. The spatial resolution is 2-degree latitude-longitude for ERSSTv5 and 5-degree latitude-longitude for HadSST.4.0.1.0 and DCENTv1.0. SST anomalies (SSTAs) are calculated relative to a 1991–2020 baseline climatology.

A marine heatwave (MHW) is defined as five or more consecutive days of SST above the 90th-percentile daily climatology (Hobday et al. 2016). MHWs are categorized as moderate when the greatest temperature anomaly during the event is less than double the difference between the 90th percentile and the seasonal climatology. When this value is more than double, triple, or quadruple the difference, the MHW is categorized as strong, severe, or extreme, respectively (Hobday et al. 2018). The direct inverse is used to detect and categorize marine cold spells (MCSs; i.e., days below the 10th percentile). MHWs and MCSs are assessed here using the DOISSTv2.1. The baseline period used to detect events in this report is 1991–2020, matching the current advice from the World Meteorological Organization (WMO) for defining climate normals. This year's report is the first to shift to the new baseline for MHWs and MCSs. All previous reports used the 1982–2011 baseline. This means that the values for MHWs will appear lower in this report than in previous years, even though, in absolute terms, the ocean continues to warm.

2. SEA SURFACE TEMPERATURES IN 2024

Record-breaking ocean temperatures in 2023 (Huang et al. 2024; Hu et al. 2024; Jiang et al. 2025) persisted into 2024. Based on DOISSTv2.1, daily global mean SSTs were at record-high levels from the beginning of 2024 until late June. Although the all-time daily record set in 2023 was not surpassed, global mean daily SSTs in 2024 were extraordinary as they significantly ($p < 0.05$) deviated from the normal SSTs throughout the year. In DOISSTv2.1, 2024 was the only year in which all daily global mean SSTs fell outside—and, in fact, above—the two standard deviations (2-SD) of the 1991–2020 SST climate normals (Yin et al. 2024), indicating that the global ocean was abnormally warm in 2024. Here, the standard deviation for each calendar day is computed based on the global mean SSTs in the same day of years during the current climate normal period of 1991–2020.

In terms of annual average global mean SST, the global ocean in 2024 was the warmest in the 171-year record of ERSSTv5. This is the second year in a row that the global ocean set a record for the warmest year. The annual average global mean SSTA in 2024 was +0.47±0.01°C, exceeding that in 2023, now the second warmest year, +0.41±0.01°C on record, by a large margin. In ERSSTv5, the warmest 10 years for the global ocean were all from the last decade, with SSTAs ranging from +0.14±0.01°C to +0.47±0.01°C. Here, the uncertainties, reported as 95% confidence intervals and expressed as ± values, were estimated by the Student's t-test using a 500-member ERSSTv5 ensemble with randomly drawn parameter values within reasonable ranges during ERSSTv5 reconstructions (Huang et al. 2015, 2020).

In 2024, annual average SSTAs were well above (>+0.2°C) the 1991–2020 climatology in most of the global ocean (Fig. 3.1a). The majority of the Indian Ocean, Atlantic Ocean, and midlatitude central-western Pacific Ocean in both hemispheres had SSTAs above +0.5°C. The 2024 ocean warming was particularly pronounced in the midlatitude North Pacific, where SSTAs mostly exceeded +2°C in a zone stretching from Japan eastward across the dateline, and in the North Atlantic, where a horseshoe-shaped SST pattern with SSTAs above +1°C emerged across the

entire basin. Meanwhile, regions including the Okhotsk Sea, Bering Sea, Greenland Sea, southeastern Pacific, and the central-eastern Pacific between 40°S and 20°S were seen with SSTAs below (<0.2°C) the climatology. The two polar oceans—the Arctic Ocean and the Southern Ocean—were comparable to their climatologies, primarily due to extensive seasonal ice coverage.

The annual average SST difference between 2023 and 2024 (2024 minus 2023) reveals that 2023 to 2024 warming was dominant in the Southern Hemisphere (Fig. 3.1b). Across the Indo-Pacific Ocean and the tropical South Atlantic Ocean, the SST difference was mostly positive and exceeded 0.5°C over the eastern Indian Ocean. In the midlatitude Southern Hemisphere, approximately south of 30°S, three warming centers and three cooling centers were almost evenly distributed in an alternating pattern. The warm center over the southeastern Pacific and the Southern Ocean along 120°W was the most pronounced warming region globally, with SSTs increasing by more than 1°C in a large area. The strong cooling along the central-eastern equatorial Pacific and the southeast tropical Pacific reflects the El Niño–Southern Oscillation phase transition from the 2023/24 El Niño event (Tan et al. 2024) to the late 2024 La Niña conditions.

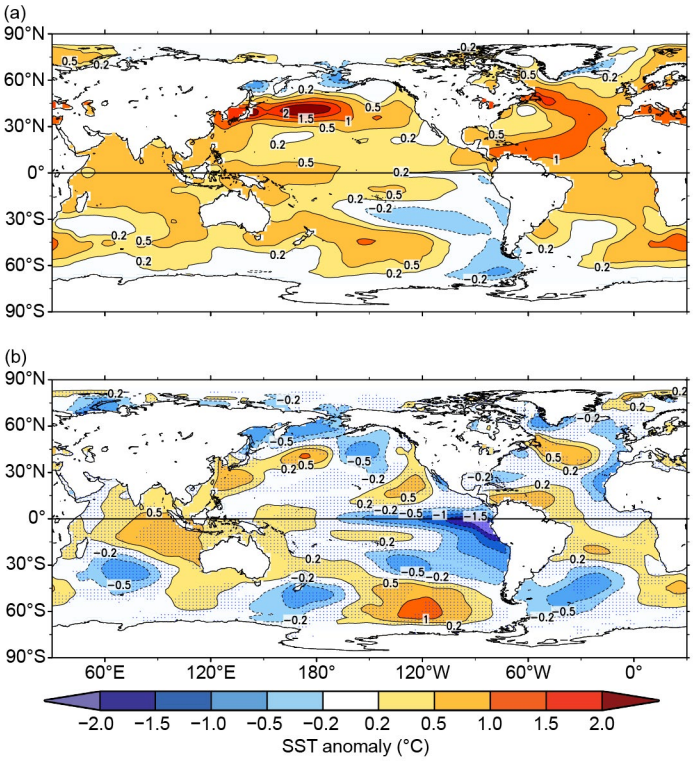

Fig. 3.1. Annual average (a) sea surface temperature anomalies (SSTAs; °C) in 2024 relative to 1991–2020 climatology and (b) differences of annual mean SSTAs from the previous year (2024 minus 2023; °C). The stippled areas in panel (b) indicate that the 2024-minus-2023 SSTA difference is significant at 95% confidence. (Source: ERSSTv5.)

Seasonal average SSTAs (Fig. 3.2) provide further insights into the temporal evolution of SSTs in 2024. Consistent with the annual result (Fig. 3.1a), positive SSTAs were dominant globally in all seasons. From boreal winter (December 2023–February 2024, Fig. 3.2a) throughout boreal autumn (September–November 2024, Fig. 3.2d), SST patterns exhibited steady and progressive changes over time in two regions: In the central-eastern equatorial Pacific, a typical El Niño SST pattern was evident during the winter season (Fig. 3.2a; Tan et al. 2024), as indicated by SSTAs above +0.5°C. However, the El Niño SST pattern began to diminish in the spring (Fig. 3.2b) and eventually transitioned to a weak La Niña SST pattern during the summer and autumn seasons (Figs. 3.2c,d). In the midlatitude central-western Pacific, the area with SSTAs over +1°C was first seen approximately west of 160°W between 30°N and 45°N in the winter (Fig. 3.2a). In the following three seasons (Figs. 3.2b–d), the area gradually expanded, particularly northward, with central SSTA contours increasing from 1.5°C to 2°C.

The tropical Atlantic Ocean was warmer than normal by more than 1°C across most of the western portion in the winter (Fig. 3.2a), and this warm area expanded to the west coasts in the spring (Fig. 3.2b). This pattern disappeared over the next two seasons (Figs. 3.2c,d); instead, a horseshoe-shaped SST pattern that was visible on the annual map (Fig. 3.1a) appeared and peaked during the summer (Fig. 3.2c).

Except for an area south of Madagascar during the first three seasons, the Indian Ocean was warmer than normal in all seasons. During the winter (Fig. 3.2a), a large band area with SSTAs exceeding +1°C extended from the Arabian Sea to Madagascar and then turned toward the southwest of Australia. However, similar to the El Niño pattern, this pattern vanished in the subsequent seasons.

In the Arctic, coastal SSTAs were negative during the winter and spring (Figs. 3.2a,b) in all seas except the Barents Sea in the winter and became positive during the summer and autumn (Figs. 3.2c d), except in the Chukchi Sea in the summer.

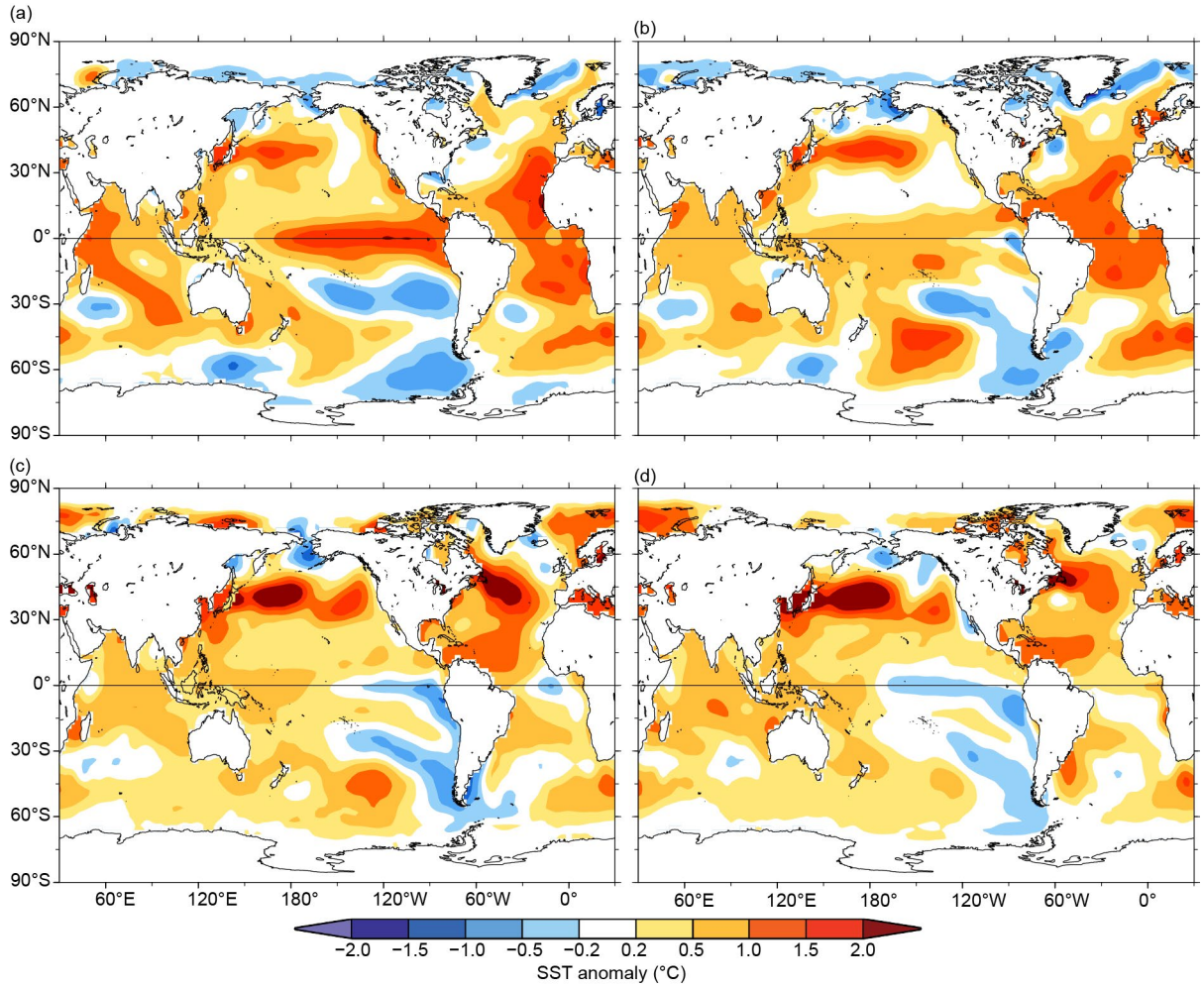

Fig. 3.2. Seasonal average sea surface temperature anomalies (SSTAs; °C; 1991–2020 base period) for (a) Dec 2023–Feb 2024, (b) Mar–May 2024, (c) Jun–Aug 2024, and (d) Sep–Nov 2024. (Source: ERSSTv5.)

3. MARINE HEATWAVES AND COLD SPELLS

In 2024, 91% of the global ocean experienced at least one marine heatwave (Fig. 3.3b) and 26% experienced at least one marine cold spell (Fig. 3.3d). The most common MHW category (Hobday et al. 2018) in 2024 was Category 2 (Strong, 46%), with the coverage of Category 3 (Severe) events reaching 8%. Category 1 (Moderate) MCSs have remained the most common (16%) cool events in all years since 1987. The ocean experienced a global average of 100 MHW days (nine MCS days) in 2024. This is far greater than the 2016 MHW record of 58 days (MCS record of 55 days in 1982; Figs. 3.3a,c). This equates to a daily average MHW coverage of 27% (2% MCS; Figs. 3.3a,c).

The year 2024 started off where 2023 ended: hot, with most of the Atlantic Ocean, the majority of all oceans within ±20° of the equator, and large patches of the Southern Ocean south of Africa and Australia in a MHW state (see Fig. 3.2 for seasonal SST anomalies). The MHW north of the equator in the Atlantic was a continuation of the basin-scale event that started in January 2023 and has continued nearly unabated for two years through to the end of 2024. It seems only a matter of time before this event gains a unique name for itself as "The Blob" did in the northeast Pacific.

Similar in size to this North Atlantic event was another event, loosely connected just to the south of the equator. Another holdover from 2023, the basin-scale event picked up steam going into March, but finally dissipated in June, just as a MHW larger than Western Europe began to develop in the North Atlantic. While this event persisted nearly to the end of the year, it broke up twice, potentially signifying different key drivers of the anomalous heat. From August to late

November, the Barents and Kara Seas experienced what has become a perennially recurring Category 4 MHW. The Gulf of Aden, and much of the surrounding waters, experienced a noteworthy MHW in February, while the Mediterranean Sea had exceptionally intense regional MHWs from July to September.

Notable MCSs within ±60° of the equator have nearly vanished since the late 1990s, with 2024 being no exception. Some high-category events took place throughout the year, though almost all were either an expression of seasonal changes in the ice edge of the polar regions or particularly pronounced anti-cyclonic eddies within the western boundary currents. That being said, the Russian coastline of the Barents Sea exhibited intense cooling from May to June, with the Kara Sea experiencing a widespread Category 4 MCS from June to July.

4. SEA SURFACE TEMPERATURE TRENDS

Time series of annual mean SSTAs from three analyses spatially averaged on global and basin scales (Fig. 3.4) differ from region to region but generally agree for a given region among the analyses and generally increase over the lengths of the records. Linear trends in ERSSTv5 for the regions shown in Fig. 3.4 were computed for the two periods of 1950–2024 and 2000–24 (Table 3.1). For comparison, trends of global mean SSTA are also

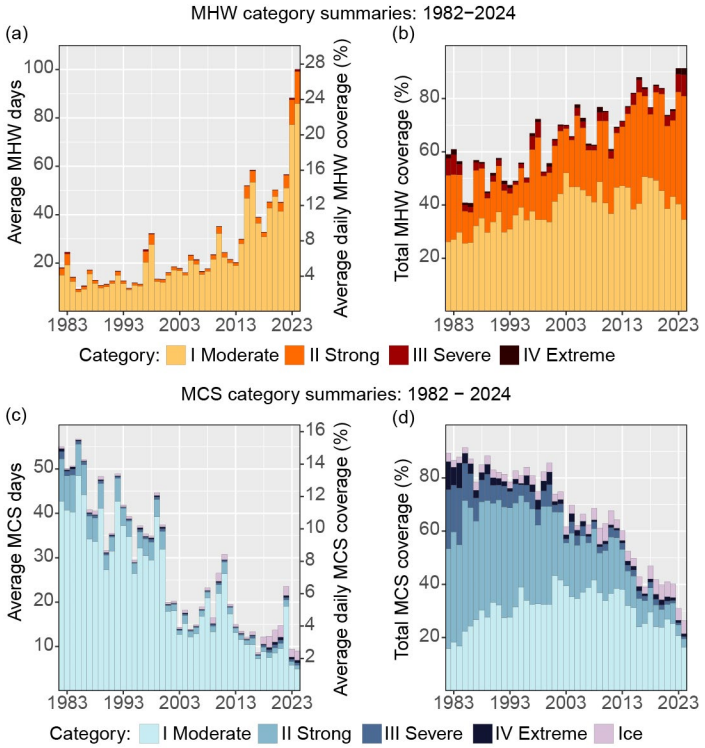

Fig. 3.3. Annual global (a),(b) marine heatwave (MHW) and (c),(d) marine cold spell (MCS) occurrences based on the 1991–2020 base period. (a) Average count of MHW days experienced over the surface of the ocean each year (left y-axis), also expressed as the percent of the surface of the ocean experiencing a MHW on any given day (right y-axis) of that year; (b) total percent of the surface area of the ocean that experienced a MHW at some point during the year; (c) same as (a) but for MCS; and (d) same as (b) but for MCS. Values shown are for the highest category of MHW/MCS experienced at any point. (Source: Daily OISST [DOISSTv2.1.])

Table 3.1. Linear trends (°C decade^{-1}) of global and regional mean annual sea surface temperature anomalies (SSTAs) from ERSSTv5, the Hadley Centre Sea Surface Temperature Dataset version 4 (HadSST4.0.1.0), the Dynamically Consistent ENsemble of Temperature (DCENTv1.0), and the Daily OISST (DOISSTv2.1). The uncertainties at a 95% confidence level, expressed as ± values, are estimated by accounting for the effective sampling number quantified by lag–1 autocorrelation on the degrees of freedom of annual mean SSTAs.

Product	Region	1950–2024	2000–24
DCENTv1.0	Global	0.13±0.01	0.19±0.06
HadSST.4.0.1.0	Global	0.12±0.02	0.21±0.07
DOISSTv2.1	Global	N/A	0.22±0.06
ERSSTv5	Global	0.11±0.01	0.18±0.06
ERSSTv5	Tropical Pacific (30°S–30°N)	0.10±0.03	0.15±0.14
ERSSTv5	North Pacific (30°N–60°N)	0.11±0.04	0.44±0.12
ERSSTv5	Tropical Indian (30°S–30°N)	0.14±0.02	0.19±0.08
ERSSTv5	North Atlantic (30°N–60°N)	0.12±0.03	0.25±0.10
ERSSTv5	Tropical Atlantic (30°S–30°N)	0.12±0.02	0.22±0.10
ERSSTv5	Southern Ocean (30°S–60°S)	0.10±0.01	0.15±0.05

assessed from DOISSTv2.1 (2000–24 only), HadSST.4.0.1.0, and DCENTv1.0. For each region, the trend of 2000–24 is greater than that of 1950–2024, indicating an accelerated ocean warming in the last few decades, particularly since the 1980s in most regions, as is apparent in Fig. 3.4.

For the global ocean, trends in ERSSTv5 during 1950–2024 and 2000–24 are 0.11±0.01°C decade^{-1} and 0.18±0.06°C decade^{-1}, respectively. At regional scales, between 1950–2024 and

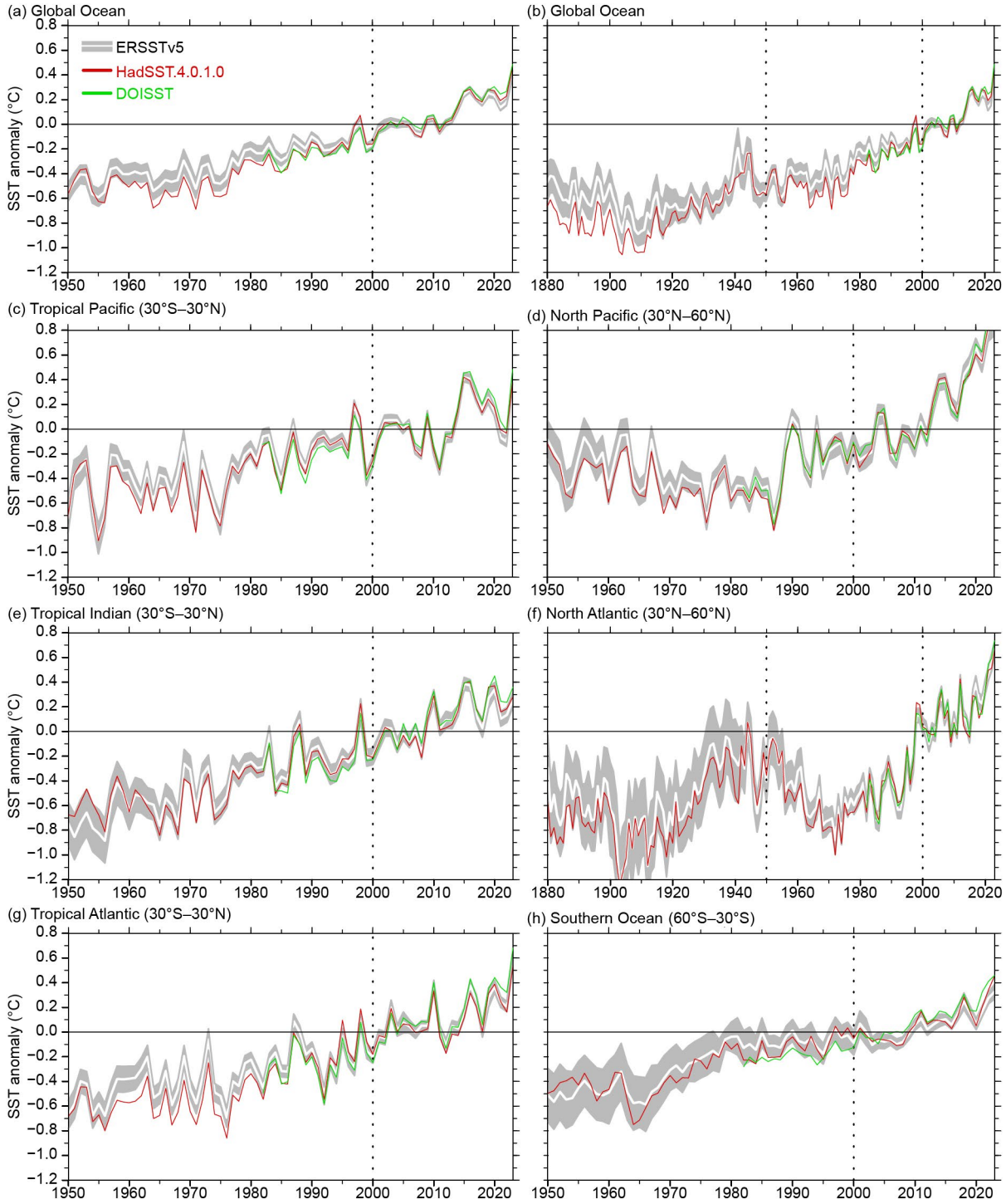

Fig. 3.4. Regional mean annual average sea surface temperature anomalies (SSTAs; °C) of ERSSTv5 (solid white), Hadley Centre Sea Surface Temperature dataset (HadSST.4.0.1.0; solid red), and Daily OISST (DOISSTv2.1; solid green) for the period 1950–2024 except for (b) and (f). (a) global ocean; (b) global ocean for 1880–2024; (c) tropical Pacific; (d) North Pacific; (e) tropical Indian; (f) North Atlantic for 1880–2024; (g) tropical Atlantic; and (h) Southern Ocean. Shadings provide the two-standard-deviation envelopes derived from a 500-member ensemble analysis based on ERSSTv5 and centered on the SSTAs of ERSSTv5. The starting years of the two periods for trend assessment, 1950 and 2000, are indicated by vertical dotted black lines.

2000–24, the warming rate difference is the highest for the North Pacific, from 0.11±0.04°C decade^{-1} to 0.44±0.12°C decade^{-1}, followed by the North Atlantic, from 0.12±0.03°C decade^{-1} to 0.25±0.10°C decade^{-1}. During the longer term since 1950, trends among different regions are comparable, ranging from 0.10°C decade^{-1} to 0.14°C decade^{-1} with the highest trends in the tropical Indian Ocean. During the shorter term since 2000, trends among different regions are widely spread, ranging from 0.15°C decade^{-1} to 0.44°C decade^{-1} with the highest trends observed in the North Pacific, suggesting an acceleration of the warming (Hu et al. 2024). Global trends calculated from different SST products, ranging from 0.11°C decade^{-1} to 0.13°C decade^{-1} over 1950–2024 and from 0.18°C decade^{-1} to 0.22°C decade^{-1} over 2000–24, are statistically indistinguishable with uncertainties considered (Table 3.1).

Departures of both DOISSTv2.1 and HadSST.4.0.1.0 from ERSSTv5 (Fig. 3.4) generally fall within the 2-SD envelope (gray shading), which was derived from a 500-member ensemble analysis of ERSSTv5 and centered on the SSTA of ERSSTv5 (Huang et al. 2020). An exception is the global mean SSTAs before the 1910s, when uncertainties in ERSSTv5 are large, and the HadSST.4.0.1.0 falls outside the 2-SD range of ERSSTv5. This is because in situ observations were scarce at the time, and different data reconstruction algorithms based on limited observations led to higher uncertainties in SST reconstructions. The SSTAs in the North Atlantic exhibit interdecadal variations in the long term since 1880 (Fig. 3.3f). This may be primarily associated with the Atlantic Multidecadal Variability (Schlesinger and Ramankutty 1994).

c. Ocean temperature and heat content anomalies

—G. C. Johnson, J. M. Lyman, L. Cheng, D. Giglio, R. E. Killick, M. Kuusela, R. Locarnini, A. Mishonov, M. Oe, J. Reagan, and T. Sukianto

The oceans are central to the transport of heat in Earth's ocean–atmosphere system (e.g., Donohoe et al. 2024). They have also absorbed ~89% of the excess heat energy entering Earth at the top of the atmosphere from 1971 to 2020 (e.g., von Schuckmann et al. 2023). Since this warming is greatest at the surface, it has increased the strength and duration of marine heatwaves (MHWs; e.g., Oliver et al. 2021) and the stratification of the upper ocean (e.g., Li et al. 2020), impacting biogeochemical cycles, ocean circulation, and ecosystems. This warming is linked to increased energy that fuels tropical cyclones (e.g., Walsh et al. 2016), sea level rise (section 3f), the melting of sea ice, ice shelves, marine terminating glaciers and ice sheets (von Schuckmann et al. 2023), and coral bleaching (e.g., Hughes et al. 2017). Here, we discuss ocean temperature and heat content anomalies for 2024 relative to 2023 as well as to a 1993–2022 climatology. We focus primarily on the upper 2 km, where temperature profiles collected by the Argo array, which first reached sparse near-global coverage around 2005, have greatly improved ocean sampling and the ability to map subsurface ocean temperature fields.

Weekly maps of ocean heat content anomaly (OHCA) relative to a 1993–2022 baseline mean (this particular 30-year time period is used because 1993 is the first full year that satellite sea surface height measurements used in this section were collected) as well as temperature for 58 pressure layers from 0 dbar to 2000 dbar were generated using Random Forest regression following Lyman and Johnson (2023) with V2.2 improvements as described at https://www.pmel.noaa.gov/rfrom/. In situ ocean temperature profiles, including Argo data downloaded from an Argo Global Data Assembly Centre in January 2025 (http://doi.org/10.17882/42182#98916), were used for training data for these maps, and prediction variables included satellite sea surface height and temperature, location, and time. In situ global estimates of OHCA for three depth layers (0 m–700 m, 700 m–2000 m, and 2000 m–6000 m) from six different research groups are also discussed. These same Argo data are used along with shipboard Conductivity-Temperature-Depth (CTD) data downloaded from the World Ocean Database (Mishonov et al. 2024; https://www.ncei.noaa.gov/access/world-ocean-database-select/dbsearch.html) in January 2025 to update a 2000-dbar–6000-dbar multidecadal estimate of deep and abyssal ocean temperature trends (Johnson and Purkey 2024).

El Niño conditions ebbed in early 2024, reached the neutral threshold in May 2024, and crossed the threshold to La Niña conditions in December 2024. Hence, the 2024-minus-2023 difference of 0-m–2000-m OHCA (Fig. 3.5b) shows a decrease across the entire equatorial Pacific—albeit stronger in the east than the west—with ocean heat content anomalies for 2024 (Fig. 3.5a) that are negative across the equatorial Pacific. Ridges of high values in 2024-minus-2023 differences are found close to the coast of the Americas at higher latitudes and farther west at lower latitudes, with troughs of low values just to the west of the high value ridges, and are likely owed to the Rossby Wave signatures of the recent El Niño and preceding La Niñas propagating in succession from the eastern boundary westward. As in 2022 and 2023, the centers of the North and South Pacific continued to be anomalously warm in 2024, with colder conditions around the edges (Fig. 3.5a), consistent with a continued negative Pacific Decadal Oscillation index in the Northern Hemisphere (section 3b). However, the centers of these basins did cool slightly from 2023 to 2024 (Fig. 3.5b), consistent with a weakening of the negative Pacific Decadal Oscillation index. As in 2022 and 2023, cold anomalies just south of the Kuroshio Extension and warm anomalies within that current in 2024 are associated with a long-lasting northward shift of that current (see Fig. 3.19a). Pacific marginal seas mostly cooled from 2023 to 2024, leaving them warm but closer to climatological means in 2024 than in 2023.

In the Indian Ocean, the 2024-minus-2023 difference of OHCA (Fig. 3.5b) mostly increased, with a decrease from west of Australia that ends just east of Madagascar. The 2024 OHCA anomalies (Fig. 3.5a) were mostly positive, with regions of somewhat negative values found from west of Australia to just east of Madagascar.

The 2024-minus-2023 difference of OHCA (Fig. 3.5b) in the Atlantic Ocean was weakly positive in most of the tropics and the northern North Atlantic, with cooling in the western subtropical North Atlantic, the Caribbean Sea, and the higher-latitude South Atlantic. Cooling on the north

side of the Gulf Stream extension east of about 70°W continued from 2023 to 2024 (it was also present from 2022 to 2023), suggesting a continued southward shift in the axis of that current in the region (Figs. 3.19a,b). Much of the Atlantic Ocean exhibited OHCA well above the 1993–2022 average (Fig. 3.5a), as it has in recent years. In addition to the cool region on the northern edge of the Gulf Stream extension east of about 70°W already noted, the cooler-than-average conditions were found southeast of Greenland, where they have persisted for several years.

As expected, the large-scale statistically significant regional patterns in the 1993–2024 local linear trends of 0-m–2000-m OHCA (Fig. 3.5c) are similar to those from 1993–2023 (Johnson et al. 2024) and earlier *State of the Climate* reports for 0 m–700 m.

Near-global average seasonal temperature anomalies in the upper 2000 dbar of the ocean since 1993 (Fig. 3.6) show signatures of El Niño and La Niña events (Fig. 3.6a) and a surface-intensified warming trend over the 32-year time period (Fig. 3.6b). Boreal winter 2023/24 shows a typical El Niño signature, with a near-surface warm anomaly and a relatively cool (compared to surrounding years) subsurface anomaly centered at about 200 dbar. Other El Niño winters prominent in this record are 1997/98, 2010/11, and 2015/16. La Niña winters, which show the opposite pattern, include 1998–2001, 2007/08, and 2020–23. While near-surface warm anomalies in 2024 slowly reduced over the year as El Niño

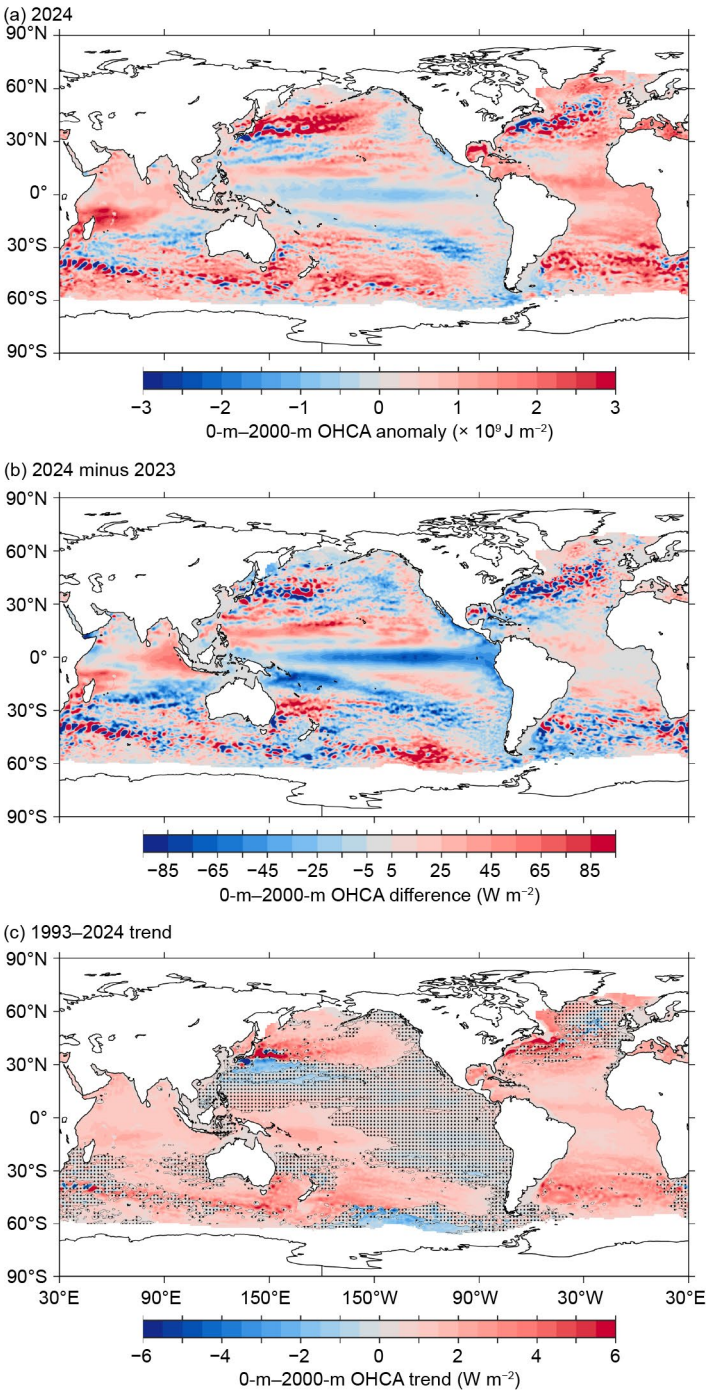

Fig. 3.5. (a) Random Forest Regression Ocean Maps (RFROM) v2 estimate of 0-m–2000-m ocean heat content anomaly (OHCA; × 10^9 J m^{-2}) for 2024 analyzed following Lyman and Johnson (2023) with v2.2 improvements as in https://www.pmel.noaa.gov/rfrom/. Values are displayed relative to a 1993–2022 baseline. (b) 2024-minus-2023 of 0-m–2000-m OHCA expressed as a local surface heat flux equivalent (W m^{-2}). For (a) and (b) comparisons, note that 95 W m^{-2} applied over one year results in a 3 × 10^9 J m^{-2} change of OHCA. (c) Linear trend for 1993–2024 0-m–2000-m annual OHCA (W m^{-2}). Areas with statistically insignificant trends at 5%–95% confidence (taking into account the decorrelation time scale of the residuals when estimating effective degrees of freedom) are stippled.

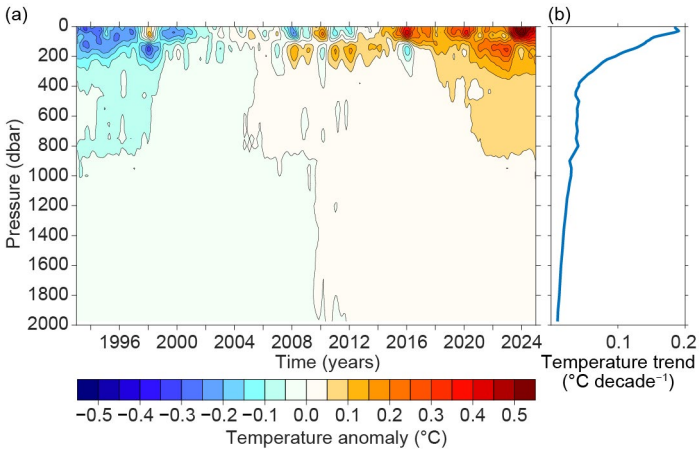

Fig. 3.6. (a) Near-global (66.5°S–81.5°N, but excluding seasonally ice-covered regions within that latitude range) average monthly ocean temperature anomalies (°C; from Random Forest Regression Ocean Maps [RFROM] v2.2, Lyman and Johnson [2023]) relative to 1993–2022 average monthly values, smoothed with a five-month Hanning filter and contoured at 0.05°C intervals (see color bar) vs. pressure and time. (b) Linear trend of temperature anomalies over the period 2004–24 in (a) plotted vs. pressure in °C $decade^{-1}$ (blue line) with 5%–95% confidence intervals (light blue shading).

faded and eventually transitioned to weak La Niña conditions, the near-surface ocean remained record warm during the first half of the year and was second warmest behind 2023 in the second half of the year. Near 200 dbar, conditions were cooler in 2024 than during the previous few years when La Niña dominated but were still warmer than the 30-year (1993–2022) average. The 1993–2024 length warming trend (Fig. 3.6b) is strongest near the surface (0.19°C decade^{-1} at 30 dbar), diminishing steadily with increasing pressure to reach 0.04°C decade^{-1} by 400 dbar, remaining relatively constant until 800 dbar, and then steadily diminishing again with increasing pressure to about 0.01°C decade^{-1} at around 2000 dbar.

Globally integrated annually averaged OHCA estimates from 0 m–700 m and 700 m–2000 m from six research groups are presented (Fig. 3.7). As noted in previous reports, year-round, near-global sampling in both of those layers commenced around 2005 from Argo, making estimates relatively certain after that date. Deep expendable bathythermographs sampling to 700 m were deployed extensively over much of the globe (with the notable exception of the high southern latitudes) starting in the early 1990s (Lyman and Johnson 2014), hence the upper layer results may be fairly robust back to 1993. Results for the 700-m–2000-m layer, which is quite sparsely sampled prior to about 2005, should be interpreted with caution in earlier years.

The various estimates of annual globally integrated 0-m–700-m OHCA (Fig. 3.7a) consistently show large increases since 1993, with all six analyses reporting 2024 as a record high. The 700-m–2000-m OHCA annual analyses (Fig. 3.7b) show a smaller, but still distinct long-term warming trend, and again all six analyses report 2024 as a record high in that deeper layer. The water column from 0 m to 700 m gained 13±7 ZJ and from 700 m to 2000 m gained 3.9±1.5 ZJ (means and standard deviations given) from 2023 to 2024. Causes of differences among estimates are discussed in Johnson et al. (2015, 2024).

The estimated linear rates of heat gain for each of the five global integral estimates of 0-m–700-m OHCA that extended from 1993 through 2024 (Fig. 3.7a) range from 0.39±0.06 W m^{-2} to 0.46±0.07 W m^{-2}. These estimates are applied over the surface area of Earth (Table 3.2) rather than the surface area of the ocean, to relate directly to the top-of-the-atmosphere energy imbalance (e.g., Loeb et al. 2021; section 2f1). For average ocean

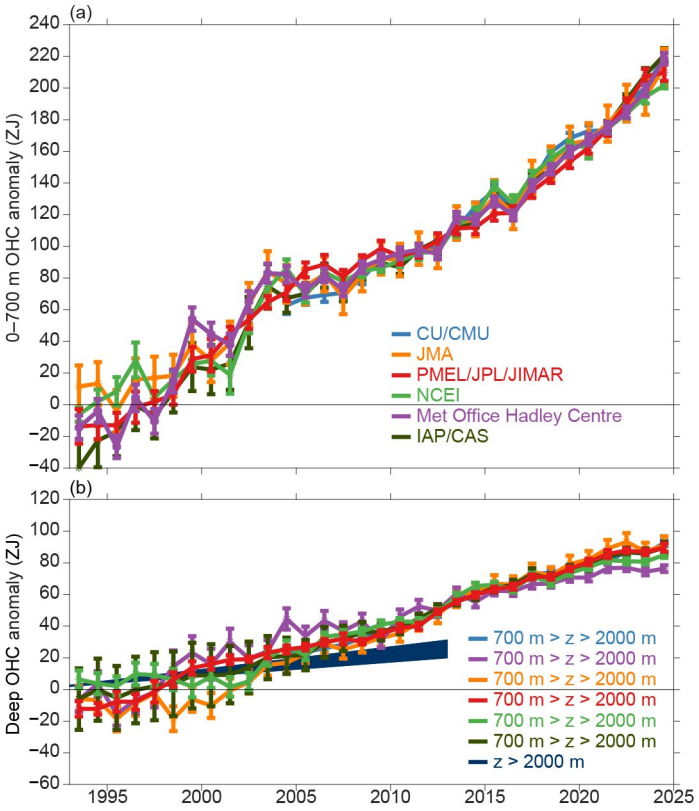

Fig. 3.7. (a) Annual average global integrals of in situ estimates of upper (0-m–700-m) ocean heat content anomaly (OHCA; ZJ; 1 ZJ = 10^{21} J) for the period 1993–2024 with standard errors of the mean. The Meteorological Research Institute (MRI)/Japan Meteorological Agency (JMA) estimate is an update of Ishii et al. (2017). The Pacific Marine Environmental Laboratory (PMEL)/Jet Propulsion Laboratory (JPL)/Cooperative Institute for Marine and Atmospheric Research (CIMAR) estimate is from Random Forest Regression Ocean Maps (RFROM) v2.2 after Lyman and Johnson (2023). The Met Office Hadley Centre estimate is computed from gridded monthly temperature anomalies following Palmer et al. (2007) and Good et al. (2013). Both the PMEL and Met Office estimates use Cheng et al. (2014) eXpendable BathyThermograph (XBT) corrections and Gouretski and Cheng (2020) mechanical bathythermograph corrections (MBT) corrections. The NCEI estimate follows Levitus et al. (2012). The Institute of Atmospheric Physics (IAP)/Chinese Academy of Sciences (CAS) estimate was reported in Cheng et al. (2025). The University of Colorado (CU)/Carnegie Mellon University (CMU) estimate is detailed in Giglio et al. (2025). See Johnson et al. (2015, 2024) for details on uncertainties, methods, and datasets. For comparison, all estimates have been individually offset (vertically on the plot), first to their individual 2005–22 means (the best sampled time period) and then to their collective 1993 mean. (b) Annual average global integrals of in situ estimates of intermediate (700-m–2000-m) OHCA for 1993–2024 (ZJ) with standard errors of the mean and a long-term trend with one-standard-error uncertainty shown from January 1988 to October 2014 for deep and abyssal (2000 dbar–6000 dbar) OHCA following Johnson and Purkey (2024) but updated as detailed in the text.

air–sea heat fluxes, estimates should be multiplied by 1.41. Linear trends from the 700-m–2000-m layer over the same time period range from 0.17±0.03 W m^{-2} to 0.24±0.04 W m^{-2}. Trends from all five groups in both layers agree within 5%–95% uncertainties. Using shipboard and Deep Argo CTD data collected from 1968 through 2024 to update the estimate of Johnson and Purkey (2024) for 2000 dbar–6000 dbar, the linear trend is 0.070±0.016 W m^{-2} from January 1988 to October 2014 (these dates are global volume average times of first and last sampling used in the local trend calculations), consistent with previously reported decadal deep and abyssal warming trends (e.g., Purkey and Johnson 2010), although with smaller uncertainties owing to the use of more data than in previous estimates. Summing the three layers (despite their different time periods as given above), the full-depth ocean heat gain rate applied to Earth's entire surface ranges from 0.66 W m^{-2} to 0.74 W m^{-2}.

Table 3.2. Trends of ocean heat content increase (in W m^{-2} applied over the 5.1 × 10^{14} m^2 surface area of Earth) from six different research groups over three depth ranges (see Fig. 3.7 for details). For the upper (0-m–700-m) and intermediate (700-m–2000-m) depth ranges, estimates cover 1993–2023, with 5%–95% uncertainties based on the residuals taking their temporal correlation into account when estimating degrees of freedom (Von Storch and Zwiers 1999). The 2000-m–6000-m depth range estimate, an update of Johnson and Purkey (2024), uses data from 1970 to 2024, having a global average start and end date of Jan 1988 to Oct 2014, again with 5%–95% uncertainty.

Research Group	0 m–700 m Global Ocean Heat Content Trends (W m^{-2})	700 m–2000 m Global Ocean Heat Content Trends (W m^{-2})	2000 m–6000 m Global Ocean Heat Content Trends (W m^{-2})
MRI/JMA	0.39±0.06	0.24±0.03	—
PMEL/JPL/JIMAR	0.42±0.09	0.21±0.02	—
NCEI	0.40±0.04	0.19±0.04	—
Met Office Hadley Centre	0.42±0.07	0.18±0.03	—
IAP/CAS	0.46±0.07	0.21±0.02	—
Johnson and Purkey	—	—	0.07±0.02

d. Salinity

—G. C. Johnson, J. Reagan, J. M. Lyman, R. Locarnini, and C. Schmid

1. INTRODUCTION

As noted in previous reports, ocean density is determined by salinity, temperature, and pressure of seawater. The vertical density structure sets the ocean stratification and impacts its interaction with the atmosphere. Horizontal density gradients are directly related to vertical ocean current shear through the thermal wind relation. In high latitudes, salinity variation plays an important role in setting ocean density. Various factors, including advection, precipitation and evaporation, river run-off, ice melt, and ice freezing (Ren et al. 2011; Yu 2011) contribute to salinity variations that impact crucial ocean–atmosphere exchanges of heat and dissolved gases, influencing phenomena like marine heatwaves and deep or bottom water formation, as well as nutrient and oxygen exchange between the surface mixed layer and denser waters below. Ocean salinity is a predictor for tropical cyclone intensity (Balaguru et al. 2012), seasonal precipitation forecasting (Li et al. 2016), and air–sea carbon dioxide (CO_2) flux (Landschützer et al. 2013).

The sea surface salinity (SSS) analysis relies on Argo data downloaded in January 2025, with annual anomaly maps relative to a seasonal climatology generated following Johnson and Lyman (2012) as well as monthly maps of bulk (as opposed to skin) SSS data from the Blended Analysis of Surface Salinity (BASS; Xie et al. 2014). BASS blends in situ SSS data with data from the *Aquarius* (Le Vine et al. 2014; mission ended in June 2015), Soil Moisture and Ocean Salinity (SMOS; Font et al. 2013), and the Soil Moisture Active Passive (SMAP; Fore et al. 2016) satellite missions. Despite the larger uncertainties of satellite data relative to Argo data, their higher spatial and temporal sampling allow higher spatial and temporal resolution maps than are possible using in situ data alone at present. To investigate interannual changes of subsurface salinity, all available salinity profile data are quality controlled following Mishonov et al. (2024) and then used to derive 1° monthly mean gridded salinity anomalies relative to a long-term monthly mean for the years 1955–2022 from World Ocean Atlas 2023 (WOA 2023; J. Reagan et al. 2024) at standard depths from the surface to 2000 m. Note that all salinity values used in this section are reported as observed, on the dimensionless Practical Salinity Scale-78 (PSS-78; Fofonoff and Lewis 1979).

In recent years, the largest source of salinity profiles is the profiling floats of the Argo program (Riser et al. 2016). These data are a mix of real-time (preliminary) and delayed-mode (scientific quality controlled) observations. Hence, the estimates presented here may be subject to instrument biases such as a positive salinity drift identified in a subset of Argo Conductivity-Temperature-Depth and will change after all data are subjected to scientific quality control.

2. SEA SURFACE SALINITY

—G. C. Johnson and J. M. Lyman

As noted in previous reports (e.g., Johnson et al. 2020), since salinity has no direct feedback to the atmosphere, unlike sea surface temperature (SST) anomalies, which are often damped by heat exchange with the atmosphere, large-scale SSS anomalies can be quite persistent. Generally, regions dominated by evaporation, such as the subtropics, exhibit higher salinity values, while areas where precipitation prevails, like the Intertropical Convergence Zone (ITCZ) and high latitudes, have fresher water (e.g., Wüst 1936; Schmitt 1995).

In the tropical Pacific, the ITCZ became fresher from 2023 to 2024 (Fig. 3.8b). The northern edge of the South Pacific Convergence Zone freshened and the southern side got saltier, suggesting a northward shift of that zone. The western equatorial Pacific also became saltier, suggesting a westward contraction of the fresh pool there with the transition from El Niño to La Niña over the year. There was also a large freshening in the climatologically fresh area west of Central America. As in 2022 and 2023, in the North Pacific, the center of the basin was mostly anomalously salty in 2024, and the periphery was generally anomalously fresh (Fig. 3.8a). Much of the South Pacific was anomalously salty in 2024.

In the Atlantic, SSS increased from 2023 to 2024 in the region of the ITCZ and the eastern equatorial area as well as in the Caribbean Sea and the Gulf of America/Gulf of Mexico (Fig. 3.8b). The center of the subtropics in both hemispheres was generally anomalously salty in 2024

(Fig. 3.8a), as it had been in 2022 and 2023 and other recent years. The ITCZ remained anomalously fresh in 2024, although somewhat less so than in 2023.

The equatorial Indian Ocean freshened south of the equator from 2023 to 2024, as did the western Arabian Gulf, whereas in the eastern Arabian basin and south of about 10°S (especially just west of Australia) the basin mostly became saltier (Fig. 3.8b). These changes resulted in an anomalously fresh region across much of the Indian Ocean north of about 10°S in 2024 (Fig. 3.8a), with weakly anomalously salty conditions south of about 10°S in that basin.

Sea surface salinity trends from 2005 to 2024 are mostly statistically insignificant, but, as in 2023 (Fig. 3.8c), there is statistically significant freshening in the eastern third of the Pacific ITCZ, the Gulf of Alaska, northeastern portions of the North Atlantic Ocean, the Greenland–Iceland–Norwegian Seas, the western Bay of Bengal, and the Gulf of Guinea. These are all climatologically fresh areas where precipitation is strong. There are also statistically significant freshening trends in the eastern Gulf of Arabia and northeast of Hawai'i, which are not climatologically fresh. Salty trends are evident in portions of the subtropics in all the ocean basins, which are climatologically salty and subject to strong evaporation, as well as the western Pacific sector of the Southern Ocean and west of Chile, which are neither. This overall "salty gets saltier and fresh gets fresher" trend, which has been evident to varying degrees and discussed in *State of the Climate* reports since 2006, is expected on a warming Earth: As the atmosphere warms, it can hold more moisture, enabling an increased hydrological cycle over the ocean (Held and Soden 2006; Durack and Wijffels 2010; Durack et al. 2012, Skliris et al. 2014).

In 2024, the seasonal BASS SSS anomalies (Fig. 3.9) show the progression of many of the features observed in the annual anomaly map using Argo data alone (Fig. 3.8a) but with higher spatial and temporal resolution, albeit likely with less accuracy. The Pacific ITCZ had the strongest fresh anomalies in the first two seasons of 2024, whereas the western equatorial Pacific became saltier in the last two seasons. In the Atlantic, the fresh anomalies in the Gulf of Guinea and the ITCZ weakened as the year progressed but, in contrast, the anomalies in the Amazon/Orinoco River plume region

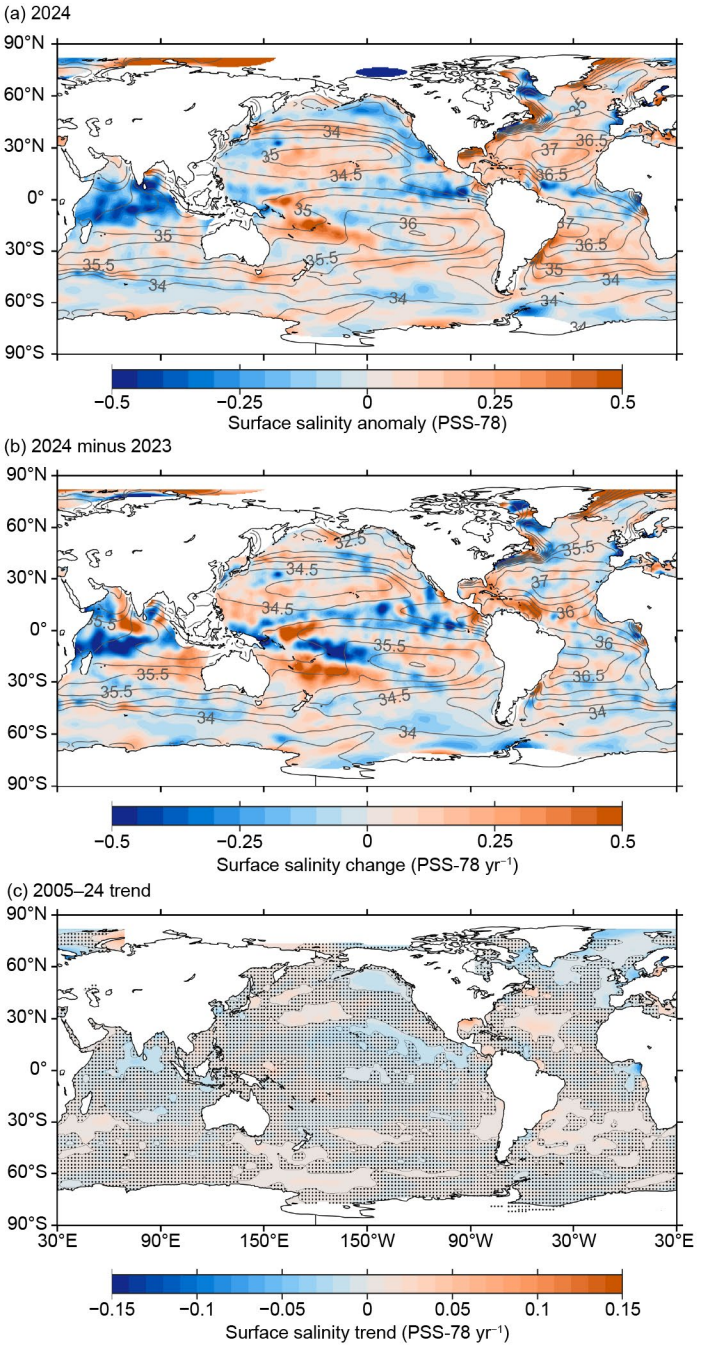

Fig. 3.8. (a) Map of the 2024 annual surface salinity anomaly (colors, Practical Salinity Scale-78 [PSS-78]) with respect to monthly climatological 1955–2022 salinity fields from World Ocean Atlas 2023 (WOA 2023; yearly average; gray contours at 0.5 intervals, PSS-78). (b) Difference of 2024 and 2023 surface salinity maps (colors, PSS-78 yr^{-1}). White ocean areas are too data-poor (retaining <80% of a large-scale signal) to map. (c) Map of local linear trends estimated from annual surface salinity anomalies for the period 2005–24 (colors, PSS-78 yr^{-1}). Areas with statistically insignificant trends at 5%–95% confidence (taking into account the decorrelation time scale of the residuals when estimating effective degrees of freedom) are stippled. All maps are made using Argo data.

started out salty and became fresher. In the Indian Ocean, the fresh basin-wide anomaly along the equator and in the Bay of Bengal in December 2023–February 2024 persisted in March–May 2024 and then weakened somewhat in the equatorial region while remaining strong in the northern Bay of Bengal even into September–November 2024.

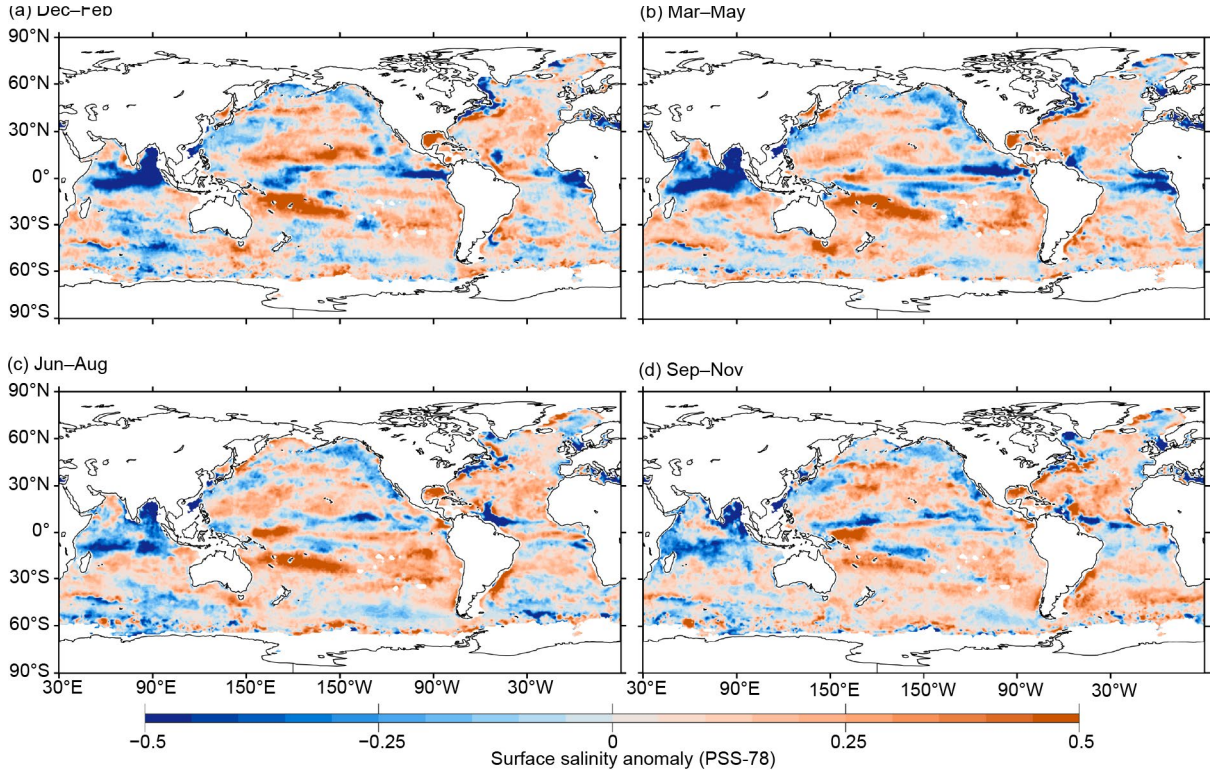

Fig. 3.9. Seasonal maps of sea surface salinity anomalies (colors) from monthly blended maps of satellite and in situ salinity data (Blended Analysis of Surface Salinity [BASS]; Xie et al. 2014) relative to monthly climatological 1955–2022 salinity fields from World Ocean Atlas 2023 (WOA 2023) for (a) Dec 2023–Feb 2024, (b) Mar–May 2024, (c) Jun–Aug 2024, and (d) Sep–Nov 2024.

3. SUBSURFACE SALINITY

—J. Reagan, R. Locarnini, and C. Schmid

Salinity changes at the surface of the ocean can be propagated to depth primarily through two pathways: subduction and convection. Subduction occurs in areas where isopycnals outcrop (intersect the surface) and are followed by downward movement of water along sloped isopycnal (constant density) surfaces. Convection is the movement of water from the surface to deeper depths through vertical mixing and penetrates deepest at high latitudes during winter. The propagation of salinity anomalies into the ocean's interior can impact ocean dynamics through changes in seawater density and is therefore an important variable to monitor.

The pattern of basin-average Atlantic salinity anomalies (Fig. 3.10a) in 2024 is similar to that of 2020 (J. R. Reagan et al. 2024), with salty anomalies (>0.06) near the surface weakening to ~0.01 between 500-m and 600-m depth. Positive salinity anomalies are dominant from 0-m–800-m depth from mid-2017 through 2024. Basin-average changes from 2023 to 2024 (Fig. 3.10b) reveal large salinification near the surface (max of 0.03 at 30 m), with a sharp drop to near 0 at 150-m depth, and slightly positive salinity anomalies (~0.003) from 200 m to 400 m with slight freshening (~−0.001) below 600 m. The causes of the salinity changes from 2023 to 2024 are clearer in the change in zonally averaged salinity between 2023 and 2024 (Fig. 3.10c). Large changes (>0.15) in the upper 30 m near 10°N with changes of >0.06 surrounding this area from 0 m–75 m and 5°N–25°N are primarily responsible for the near-surface salinification. Additional salinification occurred in the South Atlantic subtropical underwater subduction zone near ~20°S (0 m–250 m) and in the North Atlantic from 50 m to 250 m poleward of 50°N (Fig. 3.10c).

Basin average Pacific salinity anomalies (Fig. 3.10d) for 2024 continued a pattern that started in mid-2022 (J. Reagan et al. 2024). Since 2022, there has been movement toward salinification in

the upper 100 m and freshening from 125 m to 600 m in the Pacific. This pattern is clearer in the Pacific basin average difference between 2023 and 2024 (Fig. 3.10c). Salinification of ~0.018 in the upper 30 m transitioned to freshening from 125 m to 600 m with a max freshening of ~−0.01 at 200 m. The 0-m–100-m salinification between 2023 and 2024 can be attributed to large (>0.06) positive zonally averaged salinity changes at the 25°S and 25°N subduction zones (Fig. 3.10f), with the 25°S subduction zone changes as large as 0.12 in the upper 50 m. The deeper changes are primarily due to weak freshening (>−0.03) in much of the South Pacific at depths greater than 150 m, with stronger freshening (<−0.03) between 10°S–20°S and 150 m–350 m. There was also a pocket of strong freshening (<−0.09) centered at 100 m and 5°N.

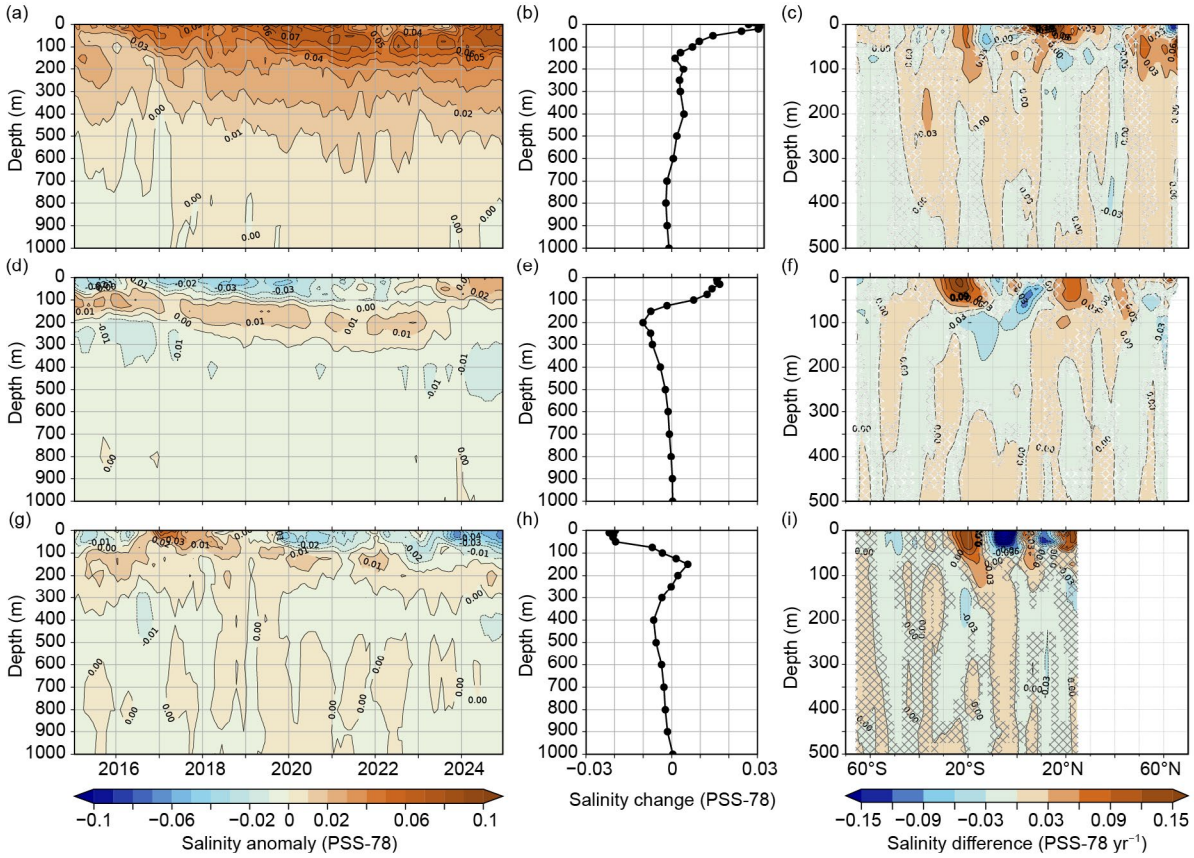

Fig. 3.10. Average monthly salinity anomalies (Practical Salinity Scale-78 [PSS-78]) vs. depth for the (a) Atlantic, (d) Pacific, and (g) Indian basins. Change in salinity from 2023 to 2024 vs. depth for the (b) Atlantic, (e) Pacific, and (h) Indian basins. Change in the zonal-average salinity from 2023 to 2024 vs. latitude and depth in the (c) Atlantic, (f) Pacific, and (i) Indian Ocean basins with areas of statistically insignificant change, defined as <±1 std. dev. and calculated from all year-to-year changes between 2005 and 2024, are stippled in gray. Data are smoothed using a three-month running mean. Anomalies are relative to the long-term (1955–2022) World Ocean Atlas (WOA) 2023 monthly salinity climatology (J. R. Reagan et al. 2024).

The basin average Indian Ocean salinity anomalies in 2024 continued the same pattern of salinity anomalies that has been evident since 2020 (brief disruption in late 2021/early 2022) with freshening near the surface, salinification below, and weak ± anomalies below 400 m (Fig. 3.10g). While the pattern in 2024 is similar to that of the previous five years, there were some notable changes between 2023 and 2024 (Fig. 3.10h). Strong freshening (~−0.02) in the upper 50 m transitioned abruptly to weak salinification (~0.005) at 150 m and then quickly changed back to weak freshening (max ~−0.008 at 400 m) from 300 m to 900 m. The negative change in salinity between 2023 and 2024 near the surface is due to large freshening (<−0.06) from 0 m to 100 m between 0° and 10°S, with values <−0.24 near the surface at 5°S. Similar to both the Atlantic and Pacific, there was salinification in the subduction zone at 20°S (from 0 m to 250 m, maximum of ~0.12 at 50 m) and additional salinification in the upper 100 m at 8°N and 22°N, but these positive changes do not negate the aforementioned near-surface freshening.

The 2005–24 zonally averaged salinity trends from 0 m to 1000 m resemble what has been documented in prior *State of the Climate* reports (e.g., J. Reagan et al. 2022, 2023, 2024; Fig. 3.11), and they continue to follow the "wet gets wetter and dry gets drier" paradigm introduced in the previous subsection. Atlantic zonally averaged significant salinity changes from 2023 to 2024 (Fig. 3.10c) mostly act to reinforce, or at least not counter, the zonally averaged significant salinity trends, with the exception being the 2023 to 2024 salinification in the North Atlantic from 50 m to 500 m between 50°N and 65°N where there has been a dominant freshening trend from 2005 to 2024 (Fig. 3.11a). The zonally averaged significant salinity changes from 2023 to 2024 in the Pacific (Fig. 3.10f) were mostly located in regions of insignificant zonally averaged salinity trends (Fig. 3.11b), but salinity decreased between 2023 and 2024 in the region centered at 15°S and 200 m where significant positive salinity trends were observed. The largest counter to the 2005–24 significant salinity trends occurred in the Indian Ocean, where there was an increase in zonally averaged salinity during 2023–24 from 0° to 10°N and from 0 m to 50 m (Fig. 3.10i); this opposed the significant freshening trend that has been evident over the past 20-year time period (Fig. 3.11c).

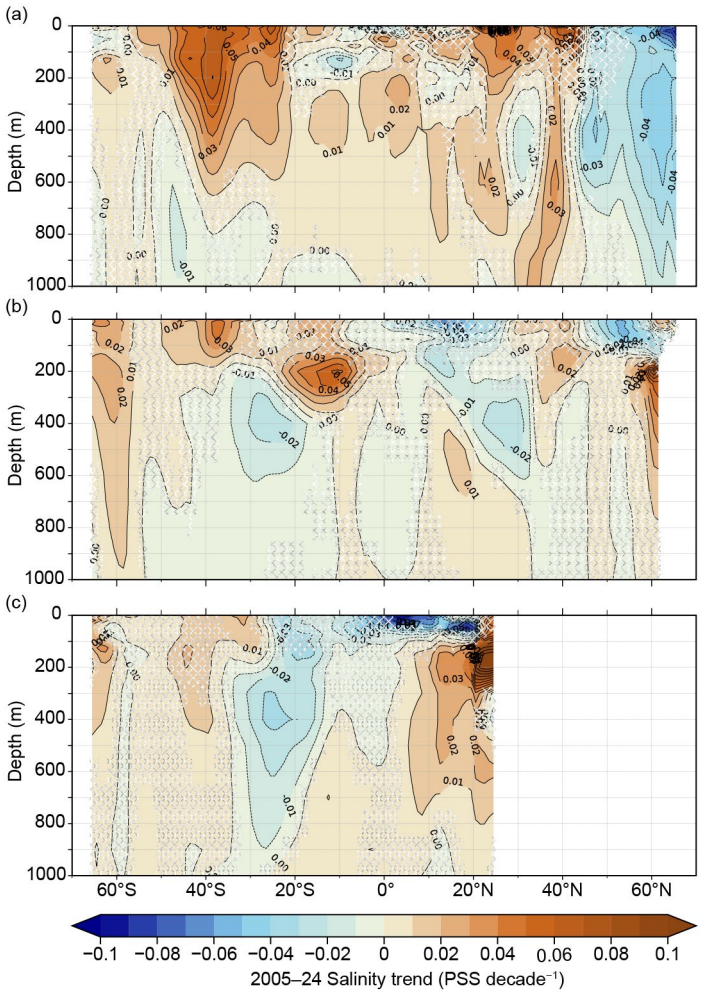

Fig. 3.11. Linear trend of zonally averaged salinity (Practical Salinity Scale-78 [PSS-78] decade^{-1}) for the period 2005–24 vs. latitude and depth for the (a) Atlantic, (b) Pacific, and (c) Indian Ocean computed using least squares regression. Areas stippled in gray are not significant at the 95% confidence interval.

e. Global ocean heat, freshwater, and momentum fluxes

—L. Yu, P. W. Stackhouse, J. Garg, and R. A. Weller

The ocean and the atmosphere interact through the exchange of heat, freshwater, and momentum across their interface. These air–sea fluxes are key to maintaining the global climate system's equilibrium in response to incoming solar radiation. The ocean absorbs the majority of shortwave radiation reaching Earth's surface and redistributes this energy to the atmosphere through longwave radiation, evaporation (latent heat flux), and conduction (sensible heat flux). Any remaining heat is stored in the ocean and transported by ocean processes that are predominantly driven by wind stress. Evaporation not only mediates heat but also moisture transfer, the latter of which, together with precipitation, determines the surface freshwater flux across the open ocean. Changes in these air–sea fluxes act as pivotal drivers for changes in ocean circulation, thereby affecting the global distribution of heat and salt from the tropics to the poles.

Here, we present the surface heat flux, freshwater flux, and wind stress in 2024 and their changes from 2023. The net surface heat flux (Q_{net}) comprises four components: shortwave (SW), longwave (LW), latent heat (LH), and sensible heat (SH). We calculate the net surface freshwater flux into the ocean, excluding inputs from rivers and glaciers, as the difference between precipitation (P) and evaporation (E), referred to as the $P–E$ flux. Data from multiple research groups are synthesized to produce global maps of Q_{net}, $P–E$, and wind stress (Figs. 3.12–3.14) and provide a long-term view over time (Fig. 3.15). Annual anomalies are relative to a 2001–15 climatology for all analyses in this section, since 2001 is the starting year for the Q_{net} estimates used here.

SW and LW in 2023 and 2024 were sourced from the Fast Longwave And Shortwave Radiative Fluxes (FLASHFlux) version 4A product (Stackhouse et al. 2006), which have been radiometrically scaled to the SW and LW products from the Clouds and the Earth's Radiant Energy System (CERES) EBAF Edition 4.2 (Loeb et al. 2018; Kato et al. 2018). P was derived from the GPCP version 2.3 products (Adler et al. 2018). Estimates for LH, SH, E, and wind stress were produced by the second generation of the OAFlux2 (Yu and Well 2007; Yu 2019), computed from satellite retrievals and the bulk parameterization COARE version 3.6 (Fairall et al. 2003). The Q_{net} time series begins in 2001, aligning with the availability of CERES EBAF 4.2 products, while the $P–E$ and wind stress time series extend back 37 years, starting in 1988.

1. SURFACE HEAT FLUXES

The 2024 Q_{net} anomaly pattern (Fig. 3.12a) shows predominantly positive anomalies (indicating downward heat input and ocean surface warming) across tropical oceans between 30°S and 30°N. In contrast, negative Q_{net} anomalies (indicating upward heat release and surface cooling) were observed at higher latitudes, poleward of ±30° latitude. This suggests that tropical oceans were the primary heat gain regions in 2024, with substantial positive Q_{net} anomalies (~10 W m^{-2}) over the tropical Indian Ocean, equatorial Pacific and Atlantic, and the western tropical Atlantic. Meanwhile, heat loss at higher latitudes is most pronounced in the central Pacific between 30°N and 50°N, where sea surface temperature (SST) anomalies of ~1°C (Fig. 3.1) persisted throughout the year, reflecting the prolonged negative phase of the Pacific Decadal Oscillation (PDO).

The 2024-minus-2023 Q_{net} difference pattern generally differs from the 2024 anomaly pattern, with the most noticeable deviations in equatorial regions. Compared to 2023, Q_{net} anomalies in 2024 were positive in the equatorial cold tongues, strongest in the Pacific (~25 W m^{-2}) and slightly weaker in the Atlantic (~10 W m^{-2}). This difference pattern is primarily driven by surface turbulent heat flux (LH+SH; Fig.3.12d) pattern, with a smaller contribution from net downward surface radiation (SW+LW; Fig. 3.12c). In the equatorial Pacific, the Q_{net} increase corresponds to 2024 SST anomalies. The transition from El Niño in 2023 to neutral conditions in early 2024 and later to La Niña conditions strengthened the cold tongue, leading to a cooler sea surface that suppressed LH+SH. As a result, less heat was lost from the sea surface, contributing to positive Q_{net} anomalies. For the SW+LW difference pattern, organized positive anomalies (~5 W m^{-2} to 10 W m^{-2}) are evident along the Intertropical Convergence Zone (ITCZ) and South Pacific Convergence Zone (SPCZ) in the Pacific, while negative anomalies of similar magnitude dominate the tropical Indian Ocean. Elsewhere, the SW+LW difference anomalies remain generally weak.

The midlatitude North Pacific in 2024 was characterized by large negative Q_{net} anomalies (~20 W m^{-2}) that extended along the Kuroshio Extension and its recirculation gyre between

20°N and 40°N, surrounded by positive Q_{net} anomalies to its east. This pattern reflects the prolonged influence of the negative PDO phase, with SST anomalies of +1°C (see Fig. 3.1) persisting throughout 2024. Meanwhile, the midlatitude North Atlantic between 30°N and 50°N experienced the opposite trend, with positive anomalies near the Gulf Stream extension surrounded by weak negative Q_{net} anomalies to the east. These patterns of Q_{net} anomalies were primarily driven by surface turbulent heat fluxes in response to contrasting changes in surface winds across these two basins (Fig. 3.14b). Stronger winds over the broad North Pacific enhanced turbulent heat loss, resulting in negative Q_{net} anomalies, whereas weaker winds over the North Atlantic reduced turbulent heat loss, increasing ocean heat gain (negative anomalies).

The South Pacific in 2024 tended to gain more heat (positive Q_{net} difference anomalies), particularly between 40°S and 15°S, perhaps related to the northward shift of the SPCZ visible in salinity changes (see Fig. 3.8b). Net downward radiation (SW+LW) increased slightly (~5 W m^{-2}), while turbulent heat loss (LH+SH) decreased substantially (>10 W m^{-2}). In contrast, the South Indian Ocean tended to lose more heat (negative Q_{net} difference anomalies) due to reduced downward radiative fluxes and increased turbulent heat loss. Changes in the South Atlantic were generally mild.

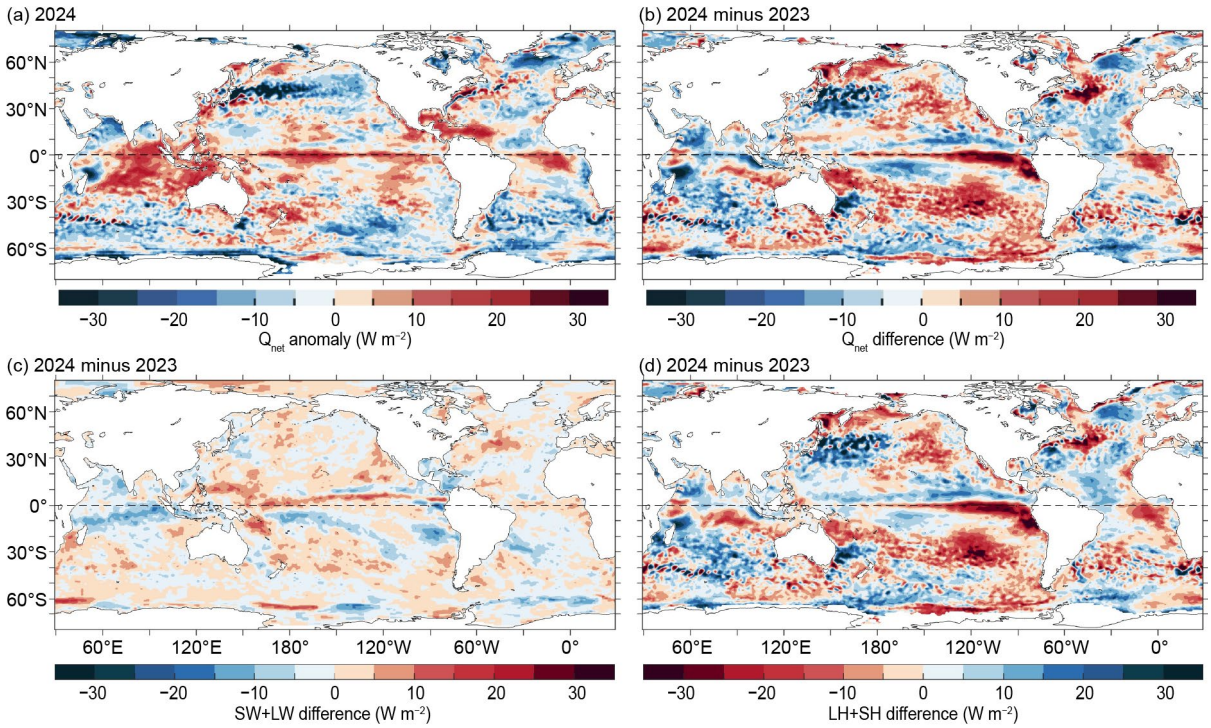

Fig. 3.12. (a) Surface heat flux (Q_{net}) anomalies (W m^{-2}) for 2024 relative to the 2001–15 climatology. Positive values denote ocean heat gain. (b) 2024-minus-2023 difference for (b) 2024-minus-2023 difference for (b) Q_{net}, (c) net surface radiation shortwave (SW) + longwave (LW), and (d) turbulent heat fluxes latent heat (LH) + sensible heat (SH), respectively. Positive tendencies denote more ocean heat gain in 2024 than in 2023. LH+SH are from the Woods Hole Oceanographic Institution (WHOI) OAFlux2, and SW+LW from Fast Longwave And SHortwave Radiative Fluxes (FLASHFlux). Net radiative fluxes are defined as the difference between the incoming and outgoing radiation (positive indicates radiative flux into the ocean).

2. SURFACE FRESHWATER FLUXES

The 2024 *P*–*E* anomalies (Fig. 3.13a) indicate a slight freshwater gain (positive anomalies) in the tropical oceans, while the extratropical oceans experienced freshwater loss (negative anomalies), particularly in the South Indian and Pacific Oceans between 60°S and 30°S, and in the North Pacific between 10°N and 50°N. Freshwater loss was most pronounced in the midlatitude central Pacific (>20 cm per year), associated with the prolonged negative PDO phase. Conversely, freshwater gain was most substantial in the western tropical Pacific and the tropical Indian Ocean, coinciding with the widespread warming in these regions (see Fig. 3.1).

The pattern of the 2024-minus-2023 differences in *P*–*E* (Fig. 3.13b) is distinct, primarily reflecting tropical changes associated with interannual ENSO variability. Pacific ITCZ rainfall decreased by more than 60 cm in 2024 compared to 2023, concurrent with the ENSO phase transition, while rainfall in the tropical Indian Ocean increased by over 40 cm. Rainfall also increased in the central Pacific, east of the SPCZ. These prominent *P*–*E* features were primarily driven by changes in precipitation (Fig. 3.13d).

The 2024-minus-2023 differences in evaporation (Fig. 3.13c) show a moderate increase (~10 cm yr^{-1}) along the Pacific ITCZ, contrasted by a substantial decrease (~25 cm yr^{-1}) in the eastern equatorial Pacific cold tongue. Evaporation also increased in the midlatitude North Pacific where large SST anomalies persisted throughout 2024, associated with the negative PDO phase. Elsewhere, changes in *P*–*E* were relatively minor.

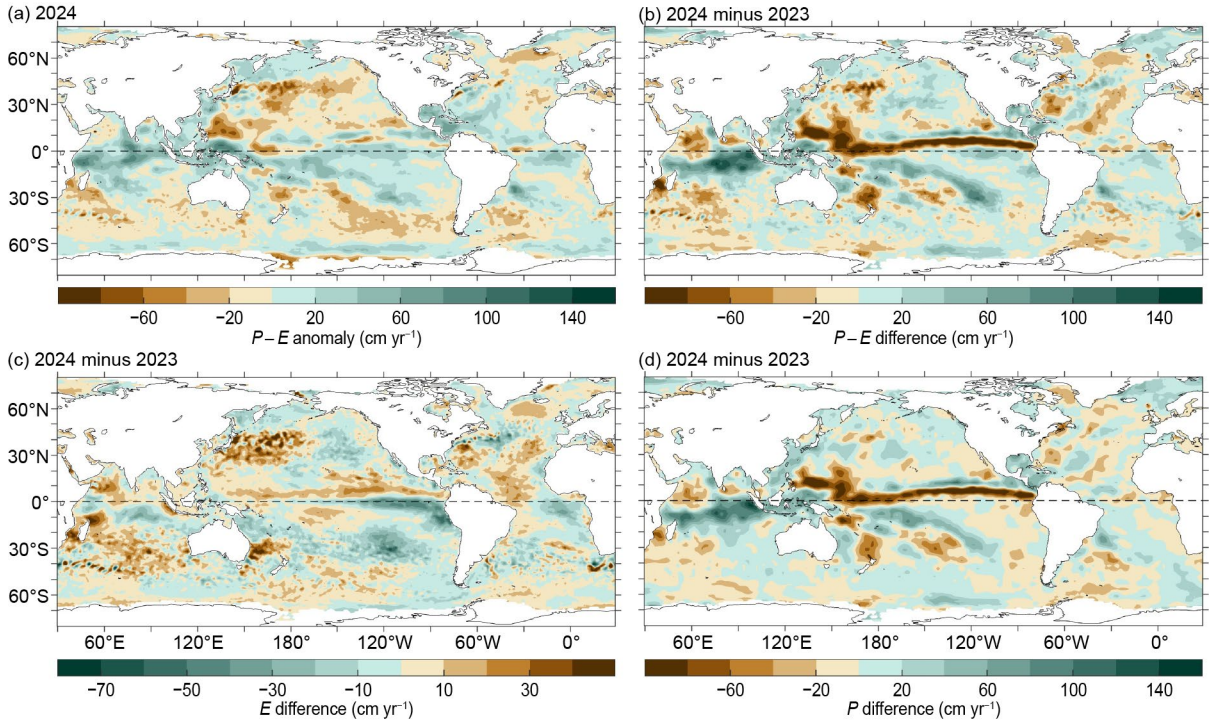

Fig. 3.13. (a) Surface freshwater precipitation (*P*)–evaporation (*E*) flux anomalies (cm yr^{-1}) for 2024 relative to the 2001–15 climatology. Positive values denote ocean freshwater gain. 2024-minus-2023 differences for (b) *P*–*E*, (c) *E*, and (d) *P*. Positive values denote ocean freshwater gain. *P* is from the GPCP version 2.3 product, and *E* is from the Woods Hole Oceanographic Institution (WHOI) OAFlux2.

3. WIND STRESS

In 2024, the tropical basins were predominantly characterized by weak negative wind stress anomalies, with considerable magnitude in the tropical North Atlantic, eastern Pacific basin, and eastern tropical Indian Ocean (Fig. 3.14a). This pattern suggests that northeast trade winds slightly strengthened in the tropical North Pacific but weakened in the tropical Atlantic. In mid- to high latitudes, wind anomalies were more pronounced. Over the Antarctic Circumpolar Current (ACC) region (40°S–60°S), Southern Hemisphere westerlies weakened substantially, with anomalies falling below −0.04 N m^{-2}. Meanwhile, midlatitude westerlies in the North Atlantic also weakened by more than 0.04 N m^{-2}, whereas those in the central North Pacific slightly strengthened (~0.02 N m^{-2}). The 2024-minus-2023 differences (Fig. 3.14b) show a distinct anomaly pattern: slightly stronger trade winds in the tropical North Pacific and a general weakening of westerlies across the Southern Ocean and the North Atlantic.

Wind patterns exhibit substantial spatial variability, leading to divergence and convergence in Ekman transport. These variations generate vertical velocity, known as Ekman pumping, which is characterized by downwelling (negative) and upwelling (positive) velocities, represented by W_{EK} at the base of the Ekman layer. The computation of W_{EK} follows the equation: $W_{EK} = 1/\rho\nabla\times(\tau/f)$, where ρ is the water density and f the Coriolis parameter.

The 2024 W_{EK} anomalies showed distinct positive anomalies in a narrow off-equatorial band of the eastern Pacific and pronounced negative anomalies in a similar narrow off-equatorial band in the Indian Ocean, both exceeding 16 cm day^{-1} (Fig. 3.14c). These patterns suggest a weakening of the regional climatological conditions.

The 2024-minus-2023 W_{EK} difference map (Fig. 3.14d) deviates from the 2024 mean anomaly pattern, reflecting wind pattern changes associated with the transition from El Niño in 2023 to ENSO neutral in early 2024 and then weak La Niña conditions by late 2024. Downwelling (negative) anomalies enhanced in the near-equatorial Pacific and Atlantic, while upwelling (positive) anomalies strengthened in the near-equatorial Indian Ocean. Outside of the equatorial zones, W_{EK} anomalies with substantial magnitudes were observed at higher latitudes, particularly in the Indo-Pacific sector of the ACC regions and the subpolar North Atlantic.

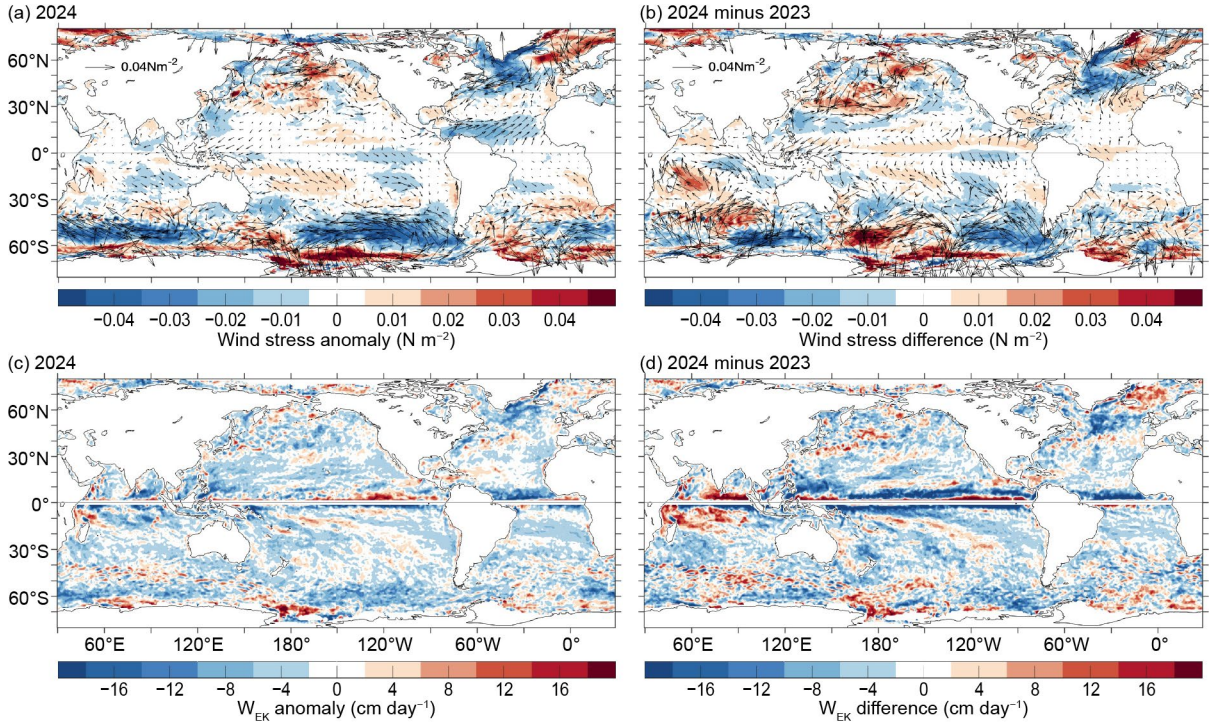

Fig. 3.14. (a) Wind stress magnitude (shaded) and vector anomalies (N m^{-2}) for 2024 relative to a 2001–15 climatology. (b) 2024-minus-2023 differences in wind stress. (c) Ekman vertical velocity (W_{EK}; cm day^{-1}) anomalies for 2024 relative to a 2001–15 climatology. Positive values denote upwelling and negative values denote downwelling. (d) 2024-minus-2023 differences of W_{EK}. Wind stress and W_{EK} fields are from the Woods Hole Oceanographic Institution (WHOI) OAFlux2.

4. LONG-TERM PERSPECTIVE

A long-term perspective on ocean surface forcing changes in 2024 is presented using a three-decade annual-mean time series of Q_{net}, $P-E$, and wind stress averaged over global ice-free oceans (Figs. 3.15a–c). Q_{net} anomalies are referenced to the 2001–15 mean, where positive anomalies indicate increased net downward heat flux into the ocean, contributing to ocean surface warming. The $P-E$ and wind stress time series span 37 years, starting in 1988, and are also referenced to the 2001–15 mean for consistency. Positive anomalies in $P-E$ denote increased freshwater flux into the ocean, leading to sea surface freshening. Similarly, positive anomalies in wind stress denote increased wind stress magnitude. Error bars in the time series represent one standard deviation of year-to-year variability.

Annual means of Q_{net}, $P-E$, and wind stress serve as indicators of the heat, freshwater, and momentum balance at the ocean surface. Q_{net} remained relatively stable from 2001 to 2010 but showed an upward trend thereafter. Between 2011 and 2016, Q_{net} increased by approximately 3±0.9 W m^{-2}, rising from ~–1±1 W m^{-2} during the 2011 La Niña to a peak of ~+2±1 W m^{-2} during the strong 2015/16 El Niño. This increase in Q_{net} coincided with a 0.35°C increase in global-mean SST (see Fig. 3.3). Subsequently, Q_{net} decreased during the 2017/18 La Niña and continued its decline

throughout the 2020–23 triple-dip La Niña. In 2024, Q_{net} was slightly higher by 0.4±0.9 W m^{-2}.

The *P*–*E* time series shows distinct decadal variability. A notable downward trend occurred in the 1990s, followed by a relatively stable period in the 2000s, and substantial interannual fluctuations in the 2010s. After peaking in 2015/16, *P*–*E* decreased by approximately 4±2 cm yr^{-1}, reaching a low point in 2021 before gradually recovering. In 2024, *P*–*E* increased by 0.8±2 cm yr^{-1} compared to 2023, approaching the climatological mean.

The wind stress time series has remained relatively stable over the past two decades following a notable regime shift around 1999. From 2000 onward, the trend has been steady, with minor interannual fluctuations. A slight reduction occurred in 2009 followed by a small increase in 2021. In 2024, the wind stress level was similar to 2023, remaining slightly weaker than the climatological mean.

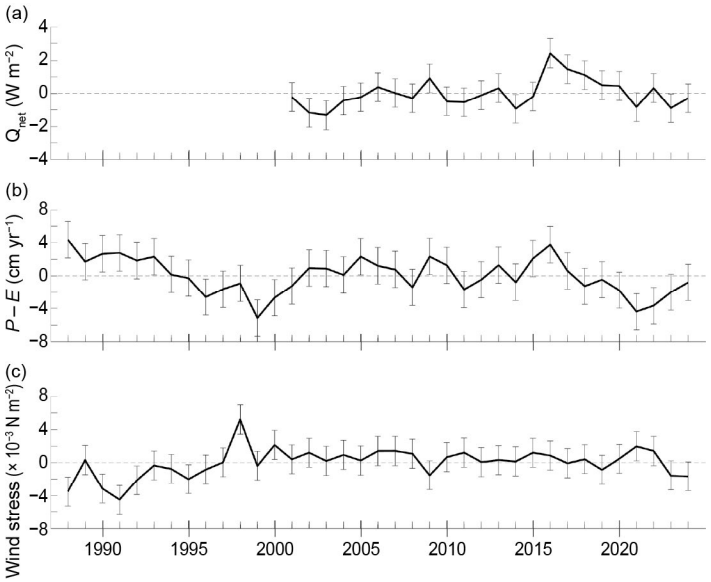

Fig. 3.15. Annual mean time series of global ocean surface (a) net surface heat flux (Q_{net}; W m^{-2}) from a combination of Clouds and the Earth's Radiant Energy System (CERES) EBAF4.2 short wave (SW) + long wave (LW) and the Woods Hole Oceanographic Institution (WHOI) OAFlux2 latent heat (LH) + sensitive heat (SH). The 2024 Q_{net} is based on FLASHFlux SW+LW as adjusted to EBAF and OAFlux2 LH+SH. (b) Net freshwater flux anomaly (*P*–*E*; cm yr^{-1}) from a combination of GPCP *P* and OAFlux2 *E*. (c) Wind stress magnitude anomalies (N m^{-2}) from WHOI OAFlux2. Error bars denote one standard deviation of annual-mean variability.

f. Sea level variability and change

—P. R. Thompson, M. J. Widlansky, B. Beckley, A. Bellas-Manley, D. P. Chambers, B. D. Hamlington, S. Jevrejeva, F. W. Landerer, E. Leuliette, M. A. Merrifield, G. T. Mitchum, R. S. Nerem, and W. Sweet

Annual average global mean sea level (GMSL) from satellite altimetry (1993–present; Beckley et al. 2024) reached a new high in 2024, rising to 105.8 mm above the 1993 mean (Fig. 3.16a). This marks the 13th consecutive year (and 29th out of the last 31) that GMSL increased relative to the previous year, reflecting unprecedented subsurface ocean temperatures during 2024 (section 3c; Cheng et al. 2025) and the combined effects of ongoing trend and acceleration in GMSL. The average linear trend over the entire altimetry era is 3.3±0.4 mm yr^{-1} (Fig. 3.16a) when corrected for glacial isostatic adjustment (GIA; −0.25±0.1 mm yr^{-1}; Tamisea and Mitrovica 2011; Caron and Ivins 2020), while acceleration in GMSL, at 0.078±0.025 mm yr^{-2}, has doubled the decadal rate of GMSL rise during the altimetry era (Hamlington et al. 2024). A quadratic fit with corrections for the eruption of Mount Pinatubo (Fasullo et al. 2016) yields a climate-driven linear trend of 3.1±0.4 mm yr^{-1} and acceleration of 0.092±0.025 mm yr^{-2} (updated from Nerem et al. 2018).

The thermosteric (i.e., ocean warming) contribution to GMSL change was 1.5±0.3 mm yr^{-1} during 2005–24 (Fig. 3.16a), which primarily reflects warming of the upper 2000 m of the ocean as measured by Argo profiling floats and analyzed by Scripps Institution of Oceanography (SIO; Roemmich and Gilson 2009). The deep ocean below 2000 m contributes less than 10% of the thermosteric trend based on measurements made by deep Argo floats and ship-based observations (Johnson and Purkey 2024). Mass concentration anomalies from GRACE and GRACE Follow-On (GRACE-FO) missions produced by the NASA Jet Propulsion Laboratory (JPL; Wiese et al. 2022) show the average mass contribution to GMSL rise during the 2005–24 period was 2.1±0.4 mm yr^{-1} when corrected for GIA –1.0±0.3 mm yr^{-1}; Caron and Ivins 2020; Fig. 3.16a). The trend in the sum of thermosteric and mass contributions, 3.5±0.5 mm yr^{-1}, agrees with the GMSL trend of 3.8±0.4 mm yr^{-1} measured by altimetry since 2005 (Leuliette and Willis 2011; Chambers et al. 2017).

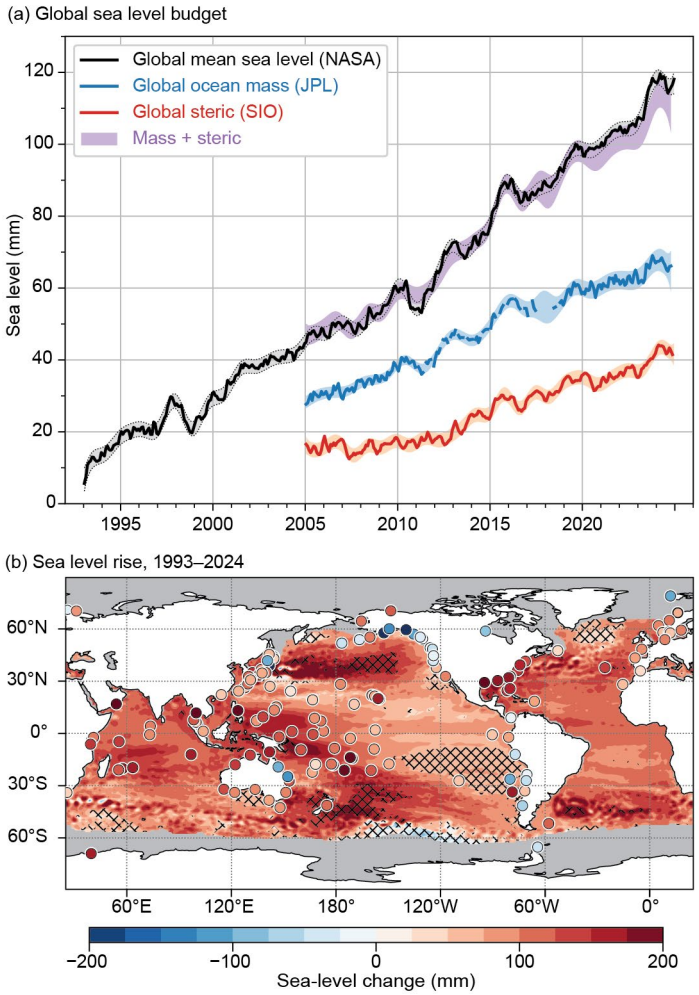

Fig. 3.16. (a) Global mean sea level (GMSL) observed by satellite altimeters (1993–2024) produced with support from the NASA Sea Level Change and Ocean Surface Topography Science Teams (black). Monthly global ocean mass (2005–24) from GRACE and GRACE-Follow-On (GRACE-FO) calculated from mass concentrations produced by NASA Jet Propulsion Laboratory (JPL; blue). GRACE and GRACE-FO data within 300 km of land were excluded. Monthly global mean thermosteric sea level (2005–24) from Scripps Institute of Oceanography (SIO) for depths above 2000 m and long-term trends from Johnson and Purkey (2024; JP24) for depths below 2000 m (red). Shading around the GMSL, mass, and thermosteric series represents a 95% confidence range for annual and longer variations, including glacial isostatic adjustment (GIA) uncertainty for the GMSL and mass time series. The confidence ranges for mass and thermosteric are used to produce a 95% confidence range for the sum of the contributions to GMSL (purple). (b) Total local sea level change during 1993–2024 as measured by satellite altimetry (contours) and tide gauges (circles). Hatching indicates local changes that differ from the change in GMSL by more than one standard deviation. The trend map was generated using gridded delayed-mode and near-real-time altimetry data produced by the Copernicus Climate Change Service and obtained from the Copernicus Marine Service. Tide-gauge observations were obtained from the University of Hawai'i Sea Level Center Fast Delivery database.

Spatial structure in sea level trends (Fig. 3.16b) has become increasingly uniform as the altimetry record has lengthened and the impact of transient fluctuations on regional sea level trends has lessened. Presently, only a small fraction of the global ocean has experienced sea level trends that differ from the GMSL trend by more than one standard deviation (hatched areas, Fig. 3.16b). However, sea level changes relative to land (i.e., the quantity measured by tide gauges; circles, Fig. 3.16b), which is most relevant for societal impacts, can differ substantially from satellite-derived changes in tectonically active regions (e.g., Japan) and areas strongly affected by vertical land movement such as glacial isostatic adjustment (e.g., Alaska; Fig. 3.16b).

Monthly GMSL anomalies peaked during March 2024 as the strong El Niño conditions that persisted through the 2023/24 boreal winter were ending (see section 4b for details), which impacted GMSL via global patterns of oceanic heat content and precipitation (Nerem et al. 1999; Hamlington et al. 2020). The return to El Niño–Southern Oscillation (ENSO)-neutral conditions by mid-year, followed by development of La Niña-like conditions late in the year, caused GMSL anomalies to fall during the second half of 2024. Despite decreasing seasonal anomalies, annually averaged GMSL increased by 4.6±1.4 mm from 2023 to 2024. This annual change is approximately half of the change from 2022 to 2023 but is still an above-average annual increase for the altimetry record. The sum of annual increases in the global mean steric contribution, 4.16±0.66 mm, and global mean mass contribution, 1.78±0.90 mm, slightly exceeds the observed annual increase in GMSL reported above, although the sum of the contributions is within the standard error of the expected total.

Local sea level anomalies averaged during 2024 were well above the 1993–2022 baseline (a 30-year period that starts with the first full year that satellite sea level maps are available) over most regions of the global ocean (Fig. 3.17a), except for near-normal conditions across much of the equatorial Pacific and parts of the tropical South Pacific. In these latter two regions, there were annual decreases in sea level from 2023 to 2024 (Fig. 3.17b). Year-over-year decreases of 5 cm to 10 cm in these regions, which also extended along the coasts of Central and South America, resulted from the change in ENSO conditions described above (see section 4b for details).

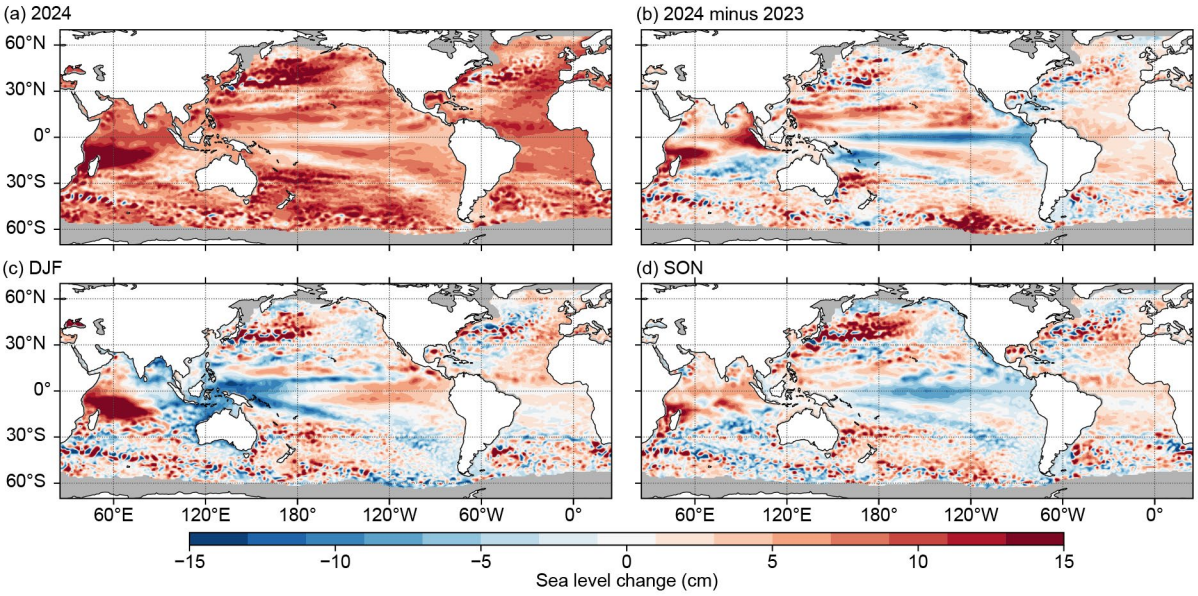

Fig. 3.17. (a) Annual average sea level anomaly during 2024 relative to average sea level at each location during 1993–2022. (b) Average 2024-minus-2023 sea level anomaly. (c) Average sea level anomaly during Dec–Feb (DJF) 2024 relative to the 1993–2022 DJF average. (d) Same as (c), but for Sep–Nov (SON). Units are given in cm. Global mean sea level was subtracted from panels (c),(d) to emphasize regional, non-secular change. These maps were generated using gridded delayed-mode and near-real-time altimetry data produced by the Copernicus Climate Change Service and obtained from the Copernicus Marine Service.

In contrast, sea levels increased year-over-year in most of the tropical North Pacific, a feature commonly observed following the termination of El Niño that is associated with high sea levels around Hawai‘i (e.g., Long et al. 2020). In the tropical South Pacific, year-over-year changes were predominantly positive east of the dateline, while the southwestern Pacific experienced decreasing sea levels, a pattern that has been linked to post-El Niño conditions and, in some cases, associated with exposed island reefs during especially low tides (e.g., Widlansky et al. 2014).

Large annual anomalies and positive year-over-year changes in the Indian Ocean reflect changes in the state of the Indian Ocean dipole (IOD). The IOD began 2024 in an extreme positive phase, which is associated with above-normal sea levels in the western Indian Ocean (Kumar et al. 2020), before transitioning to neutral by boreal summer. Sea levels in the Atlantic Ocean were mostly higher in 2024 compared to the previous year (Fig. 3.17b), consistent with long-term trends. One exception was the northwestern Caribbean and the U.S. East Coast, where year-over-year changes were negative. Despite this localized interannual decline, sea level anomalies in 2024 remained well above normal relative to the 1993–2022 baseline (Fig. 3.17a). Characteristics of oceanic eddies remained evident in the mid- and higher latitudes, both in year-over-year changes (Fig. 3.17b) and in the seasonal anomalies (Figs. 3.17c,d).

Seasonal sea level anomalies after removing the long-term trend (Figs. 3.17c,d) indicate the transition from an El Niño-associated sea level pattern (high in the east, low in the west) in early 2024 (December 2023–February 2024) to a more La Niña-like configuration (lower sea levels in most of the equatorial Pacific) by late 2024 (September–November). In the northwestern Pacific as well as around the Maritime Continent and into the Indonesian Throughflow region, sea level anomalies increased during 2024, ending the year with near-climatological values. In the tropical Indian Ocean, 2024 began with sea levels (December 2023–February 2024) that were well above normal—exceeding 15 cm in the southwestern basin—while below-normal sea levels were observed in the eastern region. After removing the long-term trend, negative anomalies extended poleward to include the Bay of Bengal and the western coast of Australia. By September–November 2024, these anomalies moderated, with sea levels in the Bay of Bengal and near Australia becoming positive. However, well-above-normal sea levels persisted in the western Indian Ocean, particularly near Africa and Madagascar, consistent with positive ocean heat content anomalies in the region (see Fig. 3.5a).

Ongoing trends, year-to-year variability, and seasonal changes in sea level impact coastal communities by increasing the magnitude and frequency of positive sea level extremes that contribute to flooding and erosion (e.g., Wahl et al. 2014; Kendon et al. 2024; Li et al. 2022). Minor impacts tend to emerge when local water levels exceed the 99th percentile of the observed daily maxima (Sweet et al. 2014). Using 1993–2022 as the epoch for calculating percentiles (consistent with the altimetry baseline), daily sea level maxima that exceed the 99th percentile—hereafter referred to as extreme sea level events—occurred more frequently in recent years compared to previous decades (Sweet et al. 2024). Tide-gauge records with at least 80% completeness during 1993–2024 and 80% completeness during both 2023 and 2024 were analyzed. Across the 110 records that met these criteria, the median number of extreme sea level events per year and location increased from one during the 1993–97 pentad to five during the 2020–24 pentad. The 90th percentile of events per year and location increased from 6 during 1993–97 to 17 during 2020–24.

Thirty-four of the 110 locations experienced more than 10 extreme sea level events during 2024 (Fig. 3.18a). These locations were distributed around the global ocean and were concentrated in areas where sea level trends and/or annual sea level anomalies were largest (Figs. 3.17a, 3.18b). The greatest number of extreme events occurred in Hawai‘i, where two locations experienced more than 30 events due to the combination of interannual increases in sea level (Figs. 3.17a,b) and local mesoscale variability. The elevated numbers of events along the North Atlantic western boundary current system reflect a continuation of extremely high sea levels from the previous year (Fig. 3.18c), which reflects ongoing ocean warming of the region (Fig. 3.5c;

Volkov et al. 2023) and trends in the amplitude of the seasonal cycle (Barroso et al. 2024; Yang and Chen 2025). Elevated numbers of extreme sea level events elsewhere in the Indian Ocean, western Pacific at midlatitudes, and eastern North Atlantic (Fig. 3.18 a) are generally consistent with the positive sea level anomalies in these regions (Fig. 3.17).

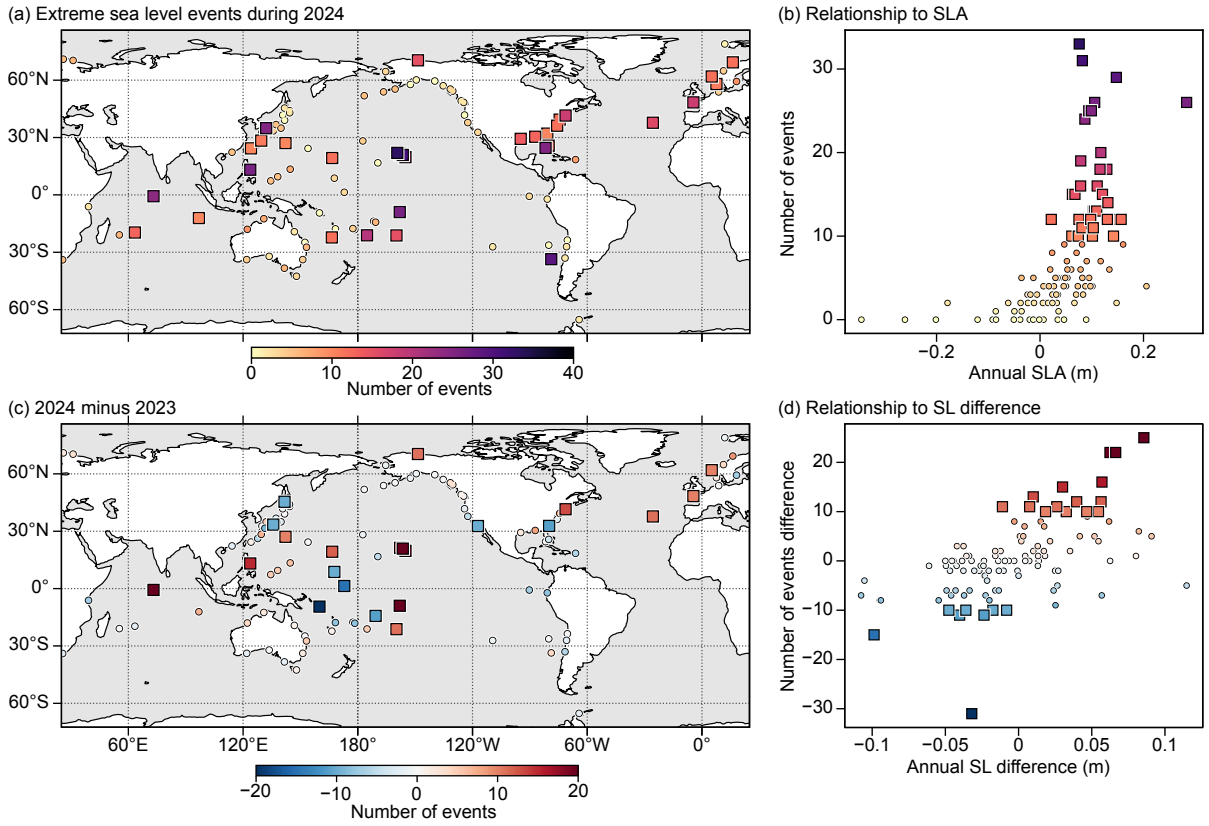

Fig. 3.18. (a) Number of extreme sea level events from tide gauges during 2024. (b) Counts in (a) as a function of annual sea level anomaly during 2024. Square markers in (a) and (b) highlight locations with more than 10 extreme events. (c) Change in number of extreme sea level events from 2023 to 2024. (d) Counts in (c) as a function of the change in annual sea level from 2023 to 2024. Square markers in (c) and (d) highlight locations where the magnitudes of changes in counts of extreme events were greater than 10. Counts of extreme sea level events were calculated from hourly tide gauge observations obtained from the University of Hawai'i Sea Level Center Fast Delivery database.

g. Surface currents

—R. Lumpkin, M. Le Hénaff, F. P. Tuchen, and R. C. Perez

This section describes variations of ocean surface currents, transports, and associated features, such as rings. Here, geostrophic and total surface currents are obtained from in situ and satellite observations. See Lumpkin et al. (2012) for details of these calculations. Zonal geostrophic current anomalies are calculated with respect to a 1993–2023 climatology (with 1993 being the first full year that satellite sea level data are available) and are discussed below for individual ocean basins.

In terms of ocean surface current retrieval methodologies, 2024 saw the continued development of Artificial Intelligence-based approaches that could be leveraged for future reports. The approaches developed by Fablet et al. (2024), Martin et al. (2024), and Kugusheva et al. (2024) all combine low-resolution altimetry sea surface height observations with higher-resolution sea surface temperature (SST), and, in the case of Kugusheva et al. (2024), chlorophyll-*a* satellite measurements. These approaches are all based on deep learning and neural networks, and they provide surface current estimates that are more accurate (Kugusheva et al. 2024), with higher resolution (Martin et al. 2024), and with a better estimation of the ageostrophic component of the current (Fablet et al. 2024). These approaches are promising for the retrieval of surface current estimates of high quality, and therefore have the potential for increased value in their applications.

In 2024, near-surface in situ measurements (12-m depth or shallower) were available from 10 mooring sites in the tropical Atlantic, 3 sites along the equator in the tropical Pacific, and 3 sites in the Indian Ocean, as part of the Global Tropical Moored Buoy Array (GTMBA, e.g., McPhaden et al. 2023). As part of the Tropical Atmosphere Ocean (TAO) recapitalization efforts, it is expected that the number of tropical Pacific moorings with near-surface current information will increase substantially in 2025/26.

1. PACIFIC OCEAN

In 2024, zonal geostrophic currents in the equatorial Pacific (Fig. 3.19a) exhibited annual mean westward (negative) current anomalies exceeding –10 cm s^{-1} between 2°S and 3°N across the basin, with the strongest anomalies of –23 cm s^{-1} along the equator at 160°E–165°E. Because these westward anomalies are a reversal of the El Niño-associated eastward anomalies of 2023 (Lumpkin et al. 2024), the 2024-minus-2023 difference map (Fig. 3.19b) reached westward values of –30 cm s^{-1}, covering nearly the entire equatorial waveguide in the Pacific basin.

Zonal current anomalies in December 2023–February 2024 (Fig. 3.20a) indicated an intensification and southward shift of the North Equatorial Countercurrent (NECC), with eastward anomalies of 16 cm s^{-1} at 6°N (south of the climatological core of the NECC) and westward anomalies of –10 cm s^{-1} at 9°N. Anomalies near the equator were close to zero during this season. In contrast, dramatic westward anomalies exceeding –10 cm s^{-1}, with an equatorial peak of –25 cm s^{-1}, dominated the central Pacific in March–May 2024 (Fig. 3.20b) concurrent with the relaxation from strong

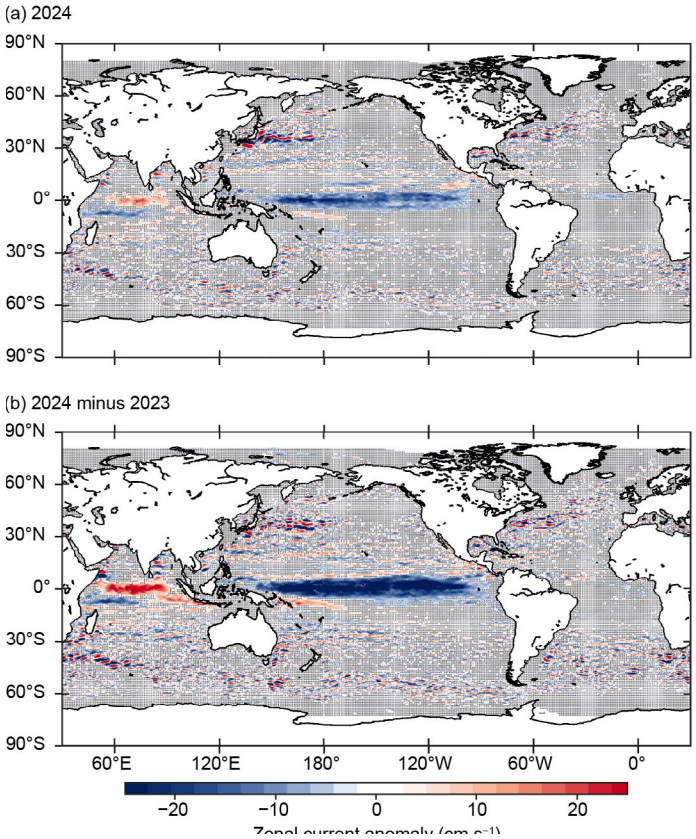

Fig. 3.19. Annually averaged geostrophic zonal current anomalies (cm s^{-1}) with respect to the seasonal climatology for (a) 2024 and (b) 2024 minus 2023. Values are only shown where they are significantly different from zero.

El Niño SST conditions in December 2023–February 2024 to El Niño–Southern Oscillation (ENSO)-neutral conditions in April–June (see section 4b). These anomalies weakened significantly in June–August (Fig. 3.20c) and September–November (Fig. 3.20d) but were still present through the end of the year.

In 2020–24, the annual-average latitude of the Kuroshio Extension in the region 141°E–153°E, 32°N–38°N was shifted north of its long-term (1993–2024) location of 35.4°N to a maximum of 36.8°N in 2021 and to 36.1°N in 2024. This can be seen as alternating eastward/westward current anomalies in Fig. 3.19a that persisted through the year (Fig. 3.20) and also in a band of increased ocean heat content anomaly (Fig. 3.5a). This 2020–24 northward shift of the Kuroshio Extension corresponded with a multi-year increase in averaged eddy kinetic energy. This pattern is associated with a meander of the Kuroshio Current off the southern coast of Japan (Qiu et al. 2020) seen in the 2024 altimetry data that has persisted since 2017 (Qiu and Chen 2021) and was noted in last year's *State of the Climate in 2023* report.

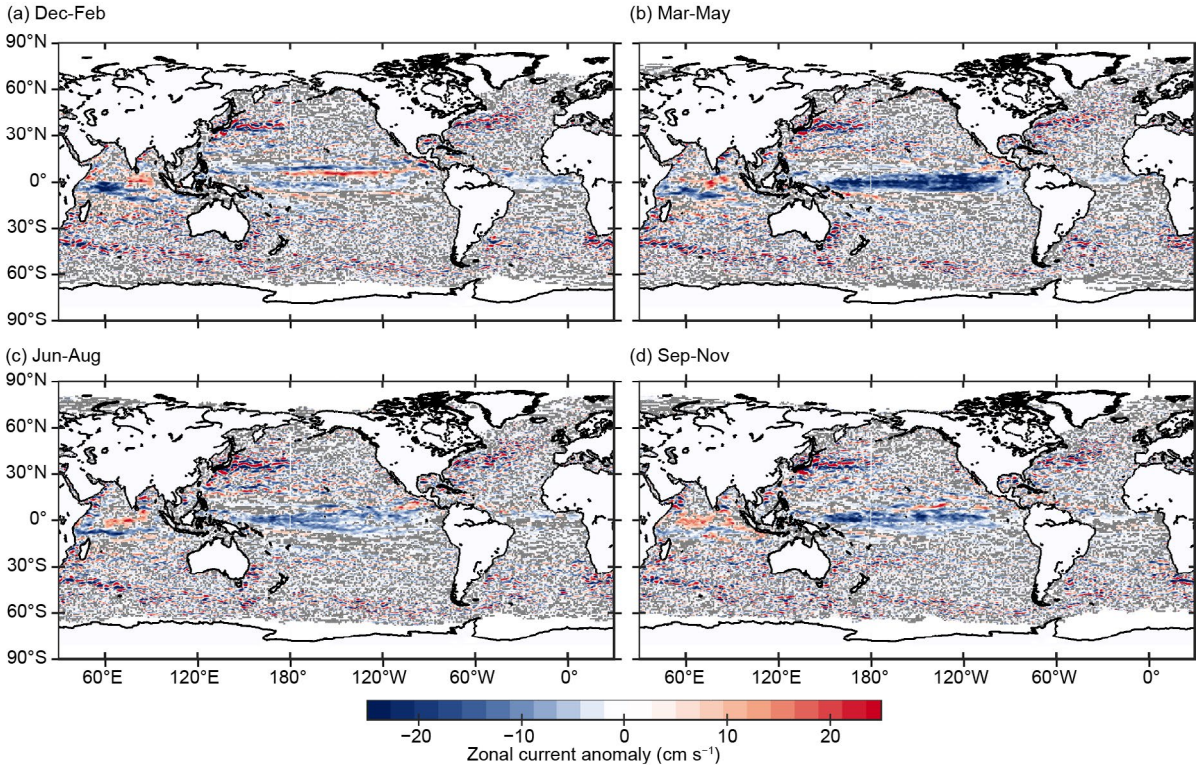

Fig. 3.20. Seasonally averaged zonal geostrophic anomalies (cm s^{-1}) with respect to seasonal climatology for (a) Dec 2023–Feb 2024, (b) Mar–May 2024, (c) Jun–Aug 2024, and (d) Sep–Nov 2024. Values are only shown where they are significantly different from zero.

In a recent study by Tuchen et al. (2024), a long-term increase of the near-surface total (geostrophic plus wind-driven) zonal currents in the tropical Pacific as well as poleward transport was shown based on a synthesis product of surface drifter data, reanalysis winds, and satellite altimetry (Fig. 3.21). Between 1993 and 2022, the westward surface currents near the equator increased by ~20%, while the eastward NECC increased in strength by ~30%. At the same time, the divergent poleward flow north and south of the equator in the central Pacific increased by ~60% and 20%, respectively. These multi-decadal trends are attributed to increased easterlies and cross-equatorial winds, likely due to natural modes of variability. As a consequence of accelerating zonal currents, tropical instability waves (TIWs) in the Pacific Ocean have significantly intensified over the same time period (Wang et al. 2024). This is due to increased meridional shear of zonal velocity in the central equatorial Pacific, causing intensified barotropic energy

conversion from the mean flow into higher-frequency fluctuations like TIWs. Continued monitoring of surface and subsurface currents through drifters, moorings, and repeat shipboard observations will be necessary to distinguish between internal and external variability.

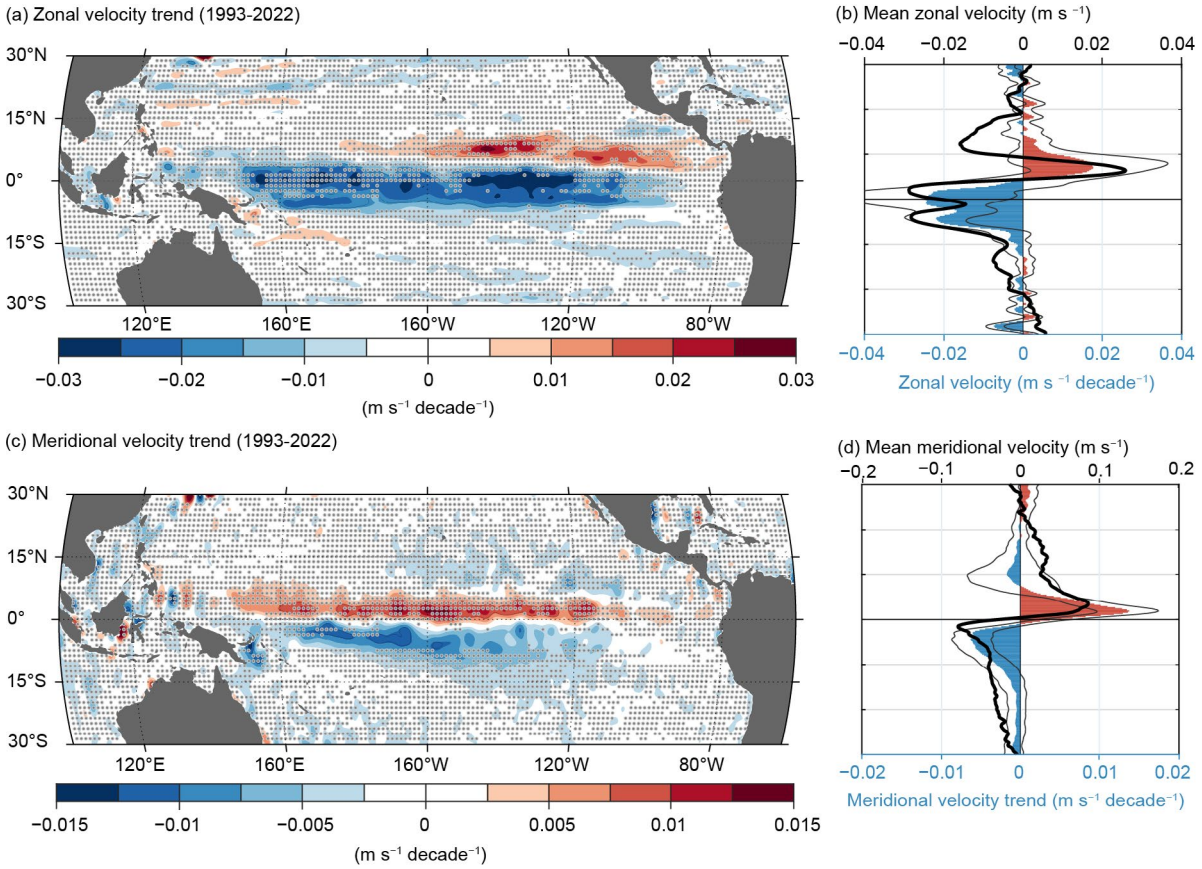

Fig. 3.21. (a) Surface zonal total velocity trend (m s^{-1} decade^{-1}) between 1993 and 2022 in the tropical Pacific. Regions where trends are not significantly different from zero at 97.5% confidence are stippled. (b) Zonally averaged (100°W–170°W) mean surface zonal velocity (black line) and surface zonal velocity trend (colored bars) as functions of latitude. Thin black lines indicate the 2.5%– 97.5% confidence intervals on the trend. (c) and (d) Same as (a) and (b) but for total meridional velocity.

2. INDIAN OCEAN

Annually-averaged geostrophic zonal current anomalies in the Indian Ocean (Fig. 3.19a) exhibited 10 cm s^{-1} to 14 cm s^{-1} eastward anomalies at 2°S–1°N and –5 cm s^{-1} to –8 cm s^{-1} westward anomalies between 6°S and 10°S. Because the equatorial currents were anomalously westward in 2023, the 2024-minus-2023 difference map (Fig. 3.19b) has strong eastward differences exceeding 20 cm s^{-1} on the equator. These eastward anomalies were not present in December 2023–February 2024 (Fig. 3.20a). They developed in March–May (Fig. 3.20b), strengthened in June–August (Fig. 3.20c), and persisted through September–November (Fig. 3.20d). Unlike in 2022/23, there was no evidence of a southward shift in the Somali Current extension.

3. ATLANTIC OCEAN

Annual mean geostrophic zonal current anomalies in the tropical Atlantic Ocean in 2024 did not exceed ±5 cm s^{-1} (Fig. 3.19a). Because a similar situation was observed in 2023, the 2024-minus-2023 difference map (Fig. 3.19b) is not remarkable. Westward –5 cm s^{-1} to –7 cm s^{-1} anomalies between 1°S and 3°N in the eastern half of the basin in December 2023–February 2024 (Fig. 3.20a) disappeared by March–May (Fig. 3.20b), and no significant anomalies reappeared in June–November (Figs. 3.20c,d). In 2024, the equatorial Atlantic experienced a series

of pronounced equatorial wave propagation events that had an impact on surface zonal velocities near the equator. According to operational reanalysis data from the European Centre for Medium-Range Weather Forecasts' Ocean ReAnalysis System 5 (ORAS5), surface zonal velocity anomalies reached values of +40 cm s^{-1} in March, causing a reversal of the surface currents that usually flow from east to west in this region and season. This situation led to a reduction in upper-ocean current shear between the surface current and the subsurface Equatorial Undercurrent. Likely, the late phase of the 2023/24 El Niño event caused westerly wind anomalies in the western equatorial Atlantic through an atmospheric teleconnection that excited equatorial waves in early 2024.

In the subtropical North Atlantic, a band of strong positive and negative anomalies of magnitude 15 cm s^{-1} to 20 cm s^{-1} east of Cape Hatteras (Fig. 3.19a) and west of 70°W indicated that the Stream extension in that region was shifted anomalously northward in 2024 compared to the long-term mean.

h. Meridional overturning circulation and heat transport in the Atlantic Ocean

—D. L. Volkov, J. K. Willis, W. Hobbs, D. A. Smeed, W. E. Johns, B. I. Moat, R. C. Perez, S. Dong, R. H. Smith, S. Speich, and T. Lamont

The observing network for the meridional overturning circulation (MOC) volume transport and the associated meridional heat transport (MHT) in the Atlantic Ocean consists of several trans-basin moored arrays and synthetic estimates based on the combination of satellite and in situ data (Fig. 3.22; Frajka-Williams et al. 2019). Here, moving from north to south, we present the updated Atlantic MOC/MHT time series for: 1) the synthetic estimates at 41°N based on satellite altimetry and Argo data (Willis and Hobbs 2025), 2) the moored RAPID–Meridional Overturning Circulation and Heat-flux Array–Western Boundary Time Series (henceforth RAPID) array at ~26.5°N (Moat et al. 2024), 3) the moored South Atlantic MOC Basin-wide Array (SAMBA) at ~34.5°S (Meinen et al. 2013, 2018), and 4) the synthetic estimates at ~34.5°S based on satellite altimetry, expendable bathythermograph, and Argo data (Dong et al. 2021). Only the synthetic estimates are updated through 2024. The estimates from the moored arrays are updated through 2022 for RAPID and through 2023 for SAMBA (MOC only). The updates for the Overturning in the Subpolar North Atlantic Program (OSNAP) trans-basin array and for the Meridional Overturning Variability Experiment (MOVE) array in western tropical North Atlantic at ~16°N are pending. Highlights here include a major revision of the Florida Current (FC) transport estimates that significantly amended the MOC/MHT at ~26.5°N (Volkov et al. 2024a) and the continued increase in the MOC/MHT at 41°N first documented in the previous year's report (Volkov et al. 2024b).

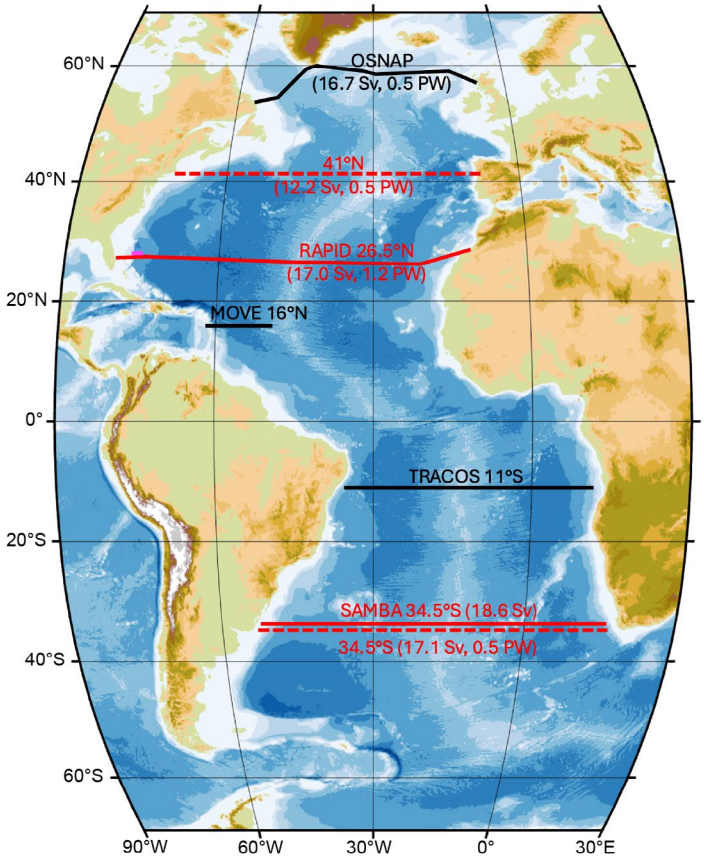

Fig. 3.22. The Atlantic meridional overturning circulation (MOC) observing network: moored arrays (solid red and black lines) and sections across which the MOC and meridional heat transport (MHT) are estimated by synthesizing in situ measurements (Argo, eXpendable BathyThermograph [XBT]) with satellite altimetry data (dashed red lines). The red lines show the sections that have updates covered in this report, while the black lines show the sections for which updates are pending. The record mean MOC and MHT values are shown in parentheses.

The synthetic MOC/MHT time series at 41°N were reproduced from Willis (2010) and Hobbs and Willis (2012) and extended to December 2024 (Fig. 3.23a; Willis and Hobbs 2025). Each individual estimate represents a three-month average with an uncertainty of ±2.3 Sverdrup (Sv) for the MOC and ±0.23 petaWatt (PW) for the MHT. The record-length time-mean MOC and MHT are 12.2 Sv and 0.46 PW, respectively. The MOC transport at 41°N was 16.2 Sv in 2024, 15.1 Sv in 2023, 12.8 Sv in 2022, and 11.2 Sv in 2021, with only the 2023 and 2024 means being statistically different from the time-mean given the uncertainty (Fig. 3.23a). The MHT was 0.74 PW in 2024 and 0.66 PW in 2023, both of which are significantly greater than the time-mean and the MHT of 0.54 PW in 2022. As quality control of Argo and altimeter data are ongoing, improvements in the estimate over the past few years are common. The improvements implemented since the *State of the Climate in 2023* report (Volkov et al. 2024b) resulted in a small decrease in the MOC transport of 0.1 Sv to 0.6 Sv in the 2021 through 2023 values, relative to last year's report. While this change is smaller than the year-to-year uncertainty in the estimate at 41°N, it is worth noting that the recent high values of the MOC in 2023 and 2024 persisted and remained unusually high, relative to the mean and variability in the Atlantic MOC volume and heat transports of the previous 20 years.

The RAPID moored array at ~26.5°N is the oldest trans-basin MOC observing array, marking 20 years of operation in April 2024. At this latitude, most of the northward volume transport in the upper limb of the MOC and in the horizontal gyre circulation is carried by the FC. The FC volume transport has been estimated from motion-induced voltages measured on submarine cables nearly continuously since 1982 (Baringer and Larsen 2001; Meinen et al. 2010). Thus, the 40+ years record of the FC transport can serve as an index of the MOC's strength in the subtropical North Atlantic. A small negative trend in the FC transport of about −0.3 Sv decade^{-1} was reported earlier (e.g., Baringer et al. 2015; Volkov et al. 2021). A major revision of the cable record was performed last year, showing that the negative trend was largely spurious, and that the FC had remained remarkably stable with a mean transport of about 32 Sv (Volkov et al. 2024a). After applying a correction for the secular change in geomagnetic field to the cable record, the negative trend was reduced to −0.1±0.2 Sv decade^{-1}, which is statistically insignificant. Because the FC transport is an integral component of the MOC/MHT estimate at ~26.5°N, the revision of the former led to a revision of the latter; both were made publicly available in September 2024 (Volkov et al. 2024a; Moat et al. 2024).

The corrected FC transport increased the record mean MOC value from 16.8 Sv to 17 Sv. This increase is smaller than the ±0.9 Sv uncertainty of annual transport estimates (McCarthy et al. 2015). Most importantly, the correction reduced the negative trend that was present in the 2004–22 MOC record from –1.3±0.7 Sv decade^{-1} to −0.8±0.7 Sv decade^{-1}. The MOC time series at ~26.5°N exhibits a decadal-scale variability, with a decline in 2004–09, an increase in 2009–18, and a decline since then (Fig. 3.23b; e.g., Moat et al. 2020; Smeed et al. 2018). In 2021 and 2022, the MOC was 15.9 Sv and 15.2 Sv, respectively, which is significantly smaller than the time-mean. The latter value was the second-lowest MOC on record, behind 2009. The MOC and MHT at ~26.5°N are highly correlated (r=0.95), suggesting that most of the poleward heat transport is carried by the overturning circulation. The time-mean MHT is 1.21 PW with a monthly standard deviation of 0.25 PW. In 2022, the MHT was 1.11 PW, which is less than the 1.18 PW in 2021 and the time-mean of 1.21 PW. However, this MHT decrease is barely significant. In recent years, the ratio of MHT to MOC has become higher due to the increasing temperature in the Florida Straits (Johns et al. 2023). Therefore, the decrease of MHT in 2022 was not as profound as the corresponding decrease of MOC.

The MOC/MHT time series at 41°N and ~26.5°N are somewhat coherent, with a correlation of 0.5, which is statistically significant at a 95% confidence level. At both latitudes, the MOC/MHT was high during 2004–08 but dropped to a record-low value in 2009. However, the following increase of MOC/MHT in 2010–18 was stronger at ~26.5°N than at 41°N (Fig. 3.23). This led to heat convergence and associated sea level rise in the subtropical gyre of the North Atlantic, which also translated to accelerated sea level rise and significantly increased flood risk along the southeast U.S. coast, including the Gulf of America/Gulf of Mexico (Domingues et al. 2018; Volkov et al. 2019, 2023). MOC/MHT divergence between ~26.5°N and 41°N in 2021/22 was due to the opposing MOC/MHT tendencies at the two latitudes (Fig. 3.23). As soon as the RAPID dataset is updated, it will be possible to see whether this divergence continued through 2023/24 and how it impacted the regional heat content and sea level. The dependence of coastal sea level on MOC-related gyre-scale processes

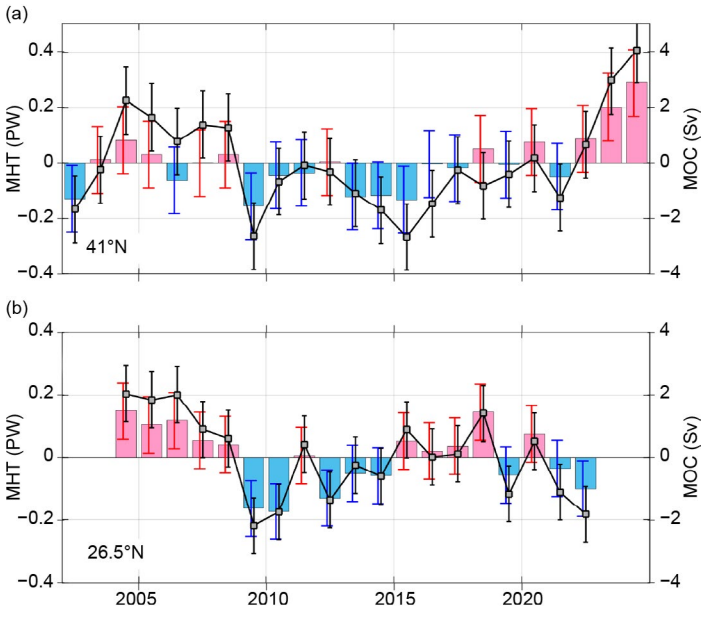

Fig. 3.23. Annual mean anomalies of meridional overturning circulation (MOC; Sverdrup [Sv]) transport (black curve) and meridional heat transport (MHT; petaWatt [PW]; pink and blue bars) relative to the respective record-length time-mean values at (a) 41°N and (b) ~26.5°N. Error bars show uncertainties for annual mean values.

is one among many examples of why the continued monitoring of MOC/MHT at ~26.5°N and 41°N is important. Because regional ocean heat content and sea level are proportional to the time-integral of MHT divergence, the observed time series of MOC/MHT provides one to three years of advance predictability for sea level.

Preliminary estimates of the MOC transport at ~34.5°S have been updated from March 2009 to December 2022 using data from SAMBA's two most inshore moorings (Fig. 3.24a). The mean MOC volume transport from the SAMBA array is 18.6 Sv with a decreasing trend of −0.56±0.32 Sv yr^{-1}. While statistically significant, the trend is largely controlled by the high annual mean values at the start of the record (25.7 Sv in 2009 and 18.9 Sv in 2010) and the low annual mean values at the end of the record from 2020 to 2022 (between 9.8 Sv and 18.4 Sv). These outlier years appear to be driven primarily by density differences, rather than by pressure differences or wind forcing, and are not evident in the synthetic time series. The mean synthetic MOC and MHT estimates at ~34.5°S are 17.1 Sv and 0.48 PW, respectively. In 2023/24, the synthetic MOC and MHT are not significantly different from record mean values considering the uncertainties (Fig. 3.24b). No long-term trend was found for the synthetic MOC, but the synthetic MHT experienced an increasing trend of 0.02±0.01 PW $decade^{-1}$ due to strong warming in the upper ocean. While SAMBA and the synthetic estimates agree well on seasonal timescales, the differences in the amplitude of their annual mean fluctuations are profound, with the SAMBA MOC being an order of magnitude more variable (Fig. 3.24). While the ground truth is unknown, it is necessary to determine the reasons for these differences, which probably arise from different instrumentation, sampling characteristics, and methodologies used.

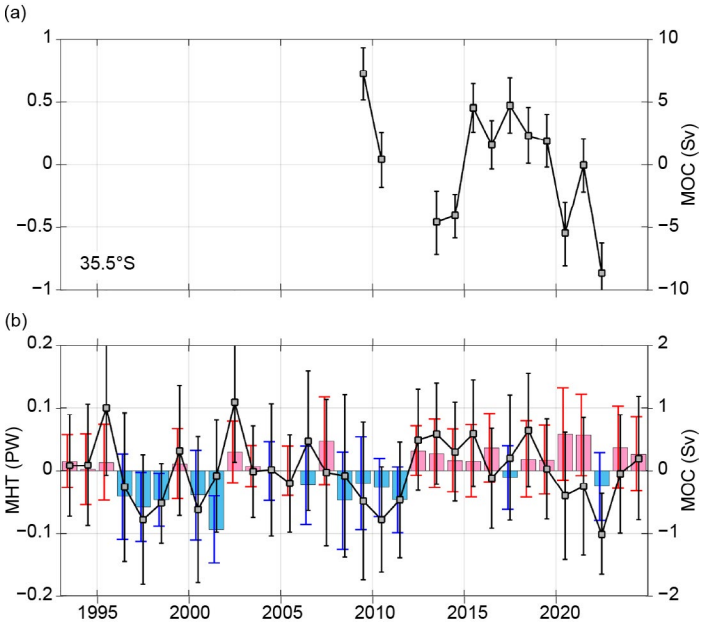

Fig. 3.24. Annual mean anomalies of meridional overturning circulation (MOC) transport (Sverdrup [Sv]; black curves) and meridional heat transport (MHT; PW; pink and blue bars) relative to the respective record-length time-mean values for (a) the South Atlantic MOC Basin-wide Array (SAMBA) and (b) synthetic estimates at 34.5°S. No MHT updates are available for the SAMBA. Error bars show uncertainties of the annual mean values.

The observational MOC/MHT estimates serve as important indicators of climate variability. The updated estimates in the North Atlantic reveal MOC/MHT divergence between 26.5°N and 41°N in the most recent years, which is part of the interannual-to-interdecadal variability that dominates the yearly time series. In the South Atlantic, it is still necessary to reconcile the MOC transports obtained from the moored SAMBA array and from the synthetic estimates at 34.5°S. Overall, the existing MOC/MHT estimates are still short compared to the climate time scales. They are just starting to showcase the decadal-scale changes. Sustained observations are therefore necessary to fully resolve inter-decadal variability and to detect a possible MOC decline projected by climate models and proxy-based reconstructions.

i. Global ocean phytoplankton

—B. A. Franz, I. Cetinić, M. Gao, and T. K. Westberry

Marine phytoplankton play a crucial role in global ecosystems, contributing about 50% of Earth's total net primary production. They meet the energy demands of oceanic food webs and provide a key mechanism for carbon sequestration, transporting carbon to the deep ocean (Field et al. 1998; Siegel et al. 2023). Diversity, abundance, and distribution of phytoplankton are influenced by both biotic factors—such as grazing by zooplankton and viruses—and abiotic factors like the availability of nutrients and light. These, in turn, depend on physical conditions like ocean temperature, stratification, and circulation (e.g., Behrenfeld et al. 2006). Observations from spaceborne ocean color sensors offer a global view of phytoplankton dynamics, tracking spatial and temporal variations by measuring near-surface concentrations of chlorophyll-*a* (Chl*a*; mg m^{-3}) and phytoplankton carbon (C_{phy}; mg m^{-3}). While Chl*a* levels reflect both phytoplankton biomass and physiological state, C_{phy} quantifies phytoplankton carbon biomass. Although Chl*a* and C_{phy} often covary, differences in their distribution can reveal shifts in the physiological or compositional makeup of phytoplankton communities (Dierssen 2010; Geider et al. 1997; Cetinić et al. 2012; Siegel et al. 2013; Westberry et al. 2016).

In this report, we evaluate the global distribution of phytoplankton over the one-year period from October 2023 through September 2024 (the analysis year, which is necessarily different from other sections owing to time required to finalize instrument calibrations and gather data from ancillary sources) using remotely sensed Chl*a* and C_{phy} measurements from a continuous 27-year record (1997–2024) that combines observations of the Sea-Viewing Wide Field-of-View Sensor (SeaWiFS; 1997–2010), Moderate Resolution Imaging Spectroradiometer on *Aqua* (MODIS-A, 2002–present), and Visible Infrared Imaging Radiometer Suite on NOAA-20 (VIIRS-N20, 2017–present). The MODIS-A daytime sea surface temperature (SST; °C) is also assessed over a consistent time period to provide context on the physical state of the oceans. The ocean color data from VIIRS-N20, MODIS-A, and SeaWiFS correspond to NASA processing version R2022. The Chl*a* product was derived using the Ocean Color Index algorithm of Hu et al. (2012), but with updated algorithm coefficients (Hu et al. 2019; O'Reilly and Werdell 2019; Werdell et al. 2023). C_{phy} was derived from the particle backscattering coefficient (b_{bp}) at 443 nm (Generalized Inherent Optical Properties algorithm; Werdell et al. 2013; McKinna et al. 2016, 2024) and a linear relationship between b_{bp} and C_{phy} (Graff et al. 2015). In merging the time series of SeaWiFS and MODIS-A, differences between the sensors were assessed over the overlapping period from 2003 through 2008, and mean bias corrections (−0.0021 mg m^{-3} in Chl*a*, −6.7e-5 m^{-1} in b_{bp} , or −0.78 mg m^{-3} of C_{phy}) were derived and applied to the SeaWiFS time series. Similarly, the overlap period of 2018 to 2020 was used to assess the differences between MODIS-A and VIIRS-N20, and bias corrections (−0.0021 mg m^{-3} in Chl*a*, −3.1e-4 m^{-1} in b_{bp} , or −3.6 mg m^{-3} of C_{phy}) were applied to the VIIRS-N20 timeseries. The bias corrections between the VIIRS-N20 and MODIS-A b_{bp} time series are relatively large, due to residual sensor radiometric calibration errors and sensitivity of the b_{bp} retrievals to spectral sampling differences between the sensors (i.e., Werdell and McKinna 2019). Efforts are underway at NASA to reduce this retrieval bias, but additional caution is warranted here in the interpretation of C_{phy} anomalies from VIIRS-N20 relative to the climatological record that is dominated by MODIS-A. However, the VIIRS-N20 instrument is temporally stable (Twetd et al. 2022) and thus provides the primary reference to assess changes over the current analysis year.

Changes in the global distribution of phytoplankton were assessed by subtracting monthly climatological means for MODIS-A Chl*a* and C_{phy} (October 2002–September 2023) from the VIIRS-N20 bias-adjusted monthly mean values for the 2024 analysis year. These monthly anomalies were then averaged to produce the global Chl*a* and C_{phy} annual mean anomaly maps (Figs. 3.25a,b). Similar calculations were performed on MODIS-A SST data to produce an equivalent SST annual mean anomaly for the same time period and climatological reference period (Fig. 3.25c). The permanently stratified ocean (PSO), which is used for the analyses depicted in Figs. 3.26 and 3.27, is defined as the region spanning the tropical and subtropical oceans where annual average SST is greater than 15°C (black lines near 40°N and 40°S in Fig. 3.25).

There, surface mixed layers are typically low in nutrients and shallower than the nutricline (Behrenfeld et al. 2006).

For the 2024 analysis year, the distribution of SST anomalies (Fig. 3.25c) is consistent with initially strong but declining El Niño conditions, including a pronounced tongue of anomalously warm waters extending across the equatorial Pacific with anomalously cool waters north and south of the feature. A similar but inverse feature is evident in the Chl*a* anomalies, with concentrations depressed (<20%) within the warm tongue and strongly elevated (>40%) in the adjacent cooler waters (Fig. 3.25a). Negative SST anomalies within the PSO are typically associated with deeper surface mixed layers (Deser et al. 2010), which reduces phytoplankton light exposure rates leading to higher cellular Chl*a* and a decoupling between Chl*a* and C_{phy} variability (Behrenfeld et al. 2016). While C_{phy} and Chl*a* anomalies appear to covary in the equatorial Pacific and the Indian Ocean south of the equator, C_{phy} is depressed where Chl*a* is elevated in the North and South Atlantic, consistent with observations in 2023 (Franz et al. 2024a). Similar decoupling between Chl*a* and C_{phy} is also observed in the Arabian Sea (Chl*a* depressed with C_{phy} elevated) and in the Indian Ocean east of Madagascar (Chl*a* elevated with C_{phy} depressed). Patches of depressed Chl*a* are visible throughout the subpolar and polar regions outside of the PSO (Fig. 3.25a), and the C_{phy} anomalies are generally elevated (Fig. 3.25b). Observed heterogeneity in biomass indicators outside of the PSO are a result of the ephemeral nature of phytoplankton blooms in these waters as well as poor spatial and temporal sampling due to clouds and low-light conditions that limit interpretation of interannual variability in higher latitude regions.

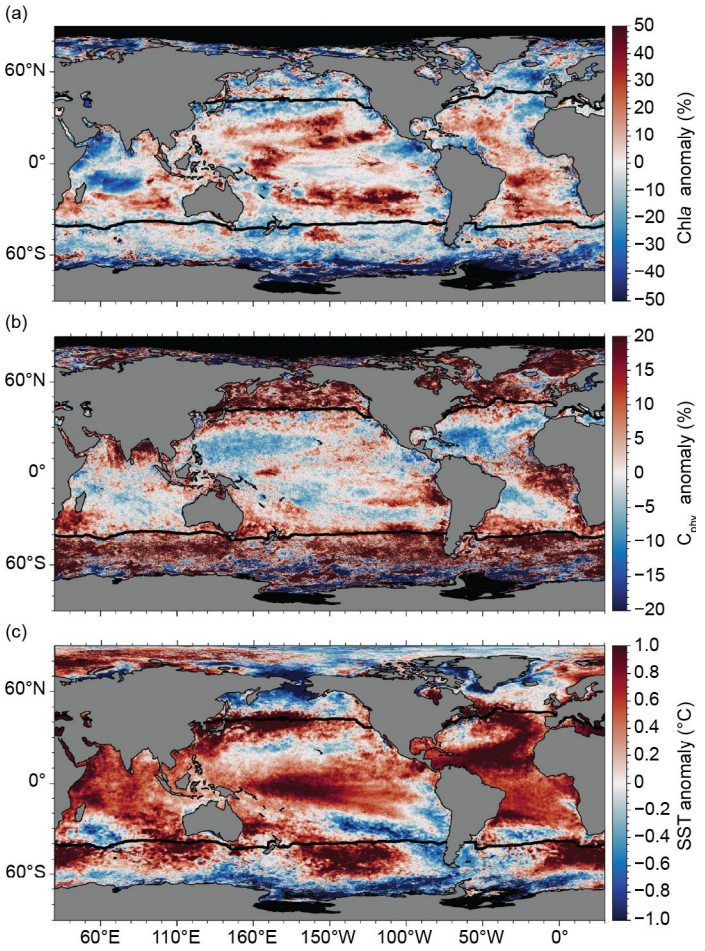

Fig. 3.25. Spatial distribution of average monthly (a) VIIRS on NOAA-20 (VIIRS-N20) chlorophyll-*a* (Chl*a*) anomalies (%), (b) VIIRS-N20 phytoplankton carbon (C_{phy}) anomalies (%), and (c) Moderate Resolution Imaging Spectroradiometer on *Aqua* (MODIS-A) sea surface temperature (SST) anomalies (°C) for Oct 2023–Sep 2024, where monthly differences were derived relative to the MODIS-A climatological record (Oct 2002–Sep 2023). Chl*a* and C_{phy} are stated as % difference from climatology, while SST is shown as an absolute difference. Also shown in each panel is the location of the mean 15°C SST isotherm (black lines) delineating the permanently stratified ocean. Differences in the SST anomalies here versus in Fig. 3.1 are owing to differences in analysis years, climatological periods, smoothing, and data sources.

Annual variability of Chl*a* and C_{phy} within the PSO typically exhibits two distinct peaks (Figs. 3.26a,b), reflecting the springtime increases of biomass in the Northern (Figs. 3.26c,d) and Southern Hemispheres (SH; Figs. 3.26g,h). The timing of peaks in C_{phy} lags two to three months behind those of Chl*a*, reflecting a reduction in phytoplankton chlorophyll-to-carbon ratios as the seasonal bloom progresses (e.g., Westberry et al. 2016) and the tight coupling between phytoplankton biomass and its losses (e.g., grazing). The timing of seasonal peaks and troughs observed in the 2024 analysis year are consistent with the monthly climatologies. The SH PSO anomalies for C_{phy} (Fig. 3.26h) were modestly low in the first half of the analysis year (October–March). A similar but stronger pattern was observed in 2023 (Franz et al. 2024a) and was traced to error in the measurements due to continuing influence of stratospheric aerosols from the 2022 Hunga eruptions (Franz et al. 2024b). Low Chl*a* and C_{phy} in the equatorial region

over the first half of the year is consistent with an expected response to the prevailing El Niño conditions over that time period, which leads to reduced upwelling and vertical transport of nutrients and thus reduced phytoplankton abundance and productivity (Behrenfeld et al. 2001; Chavez et al. 2011).

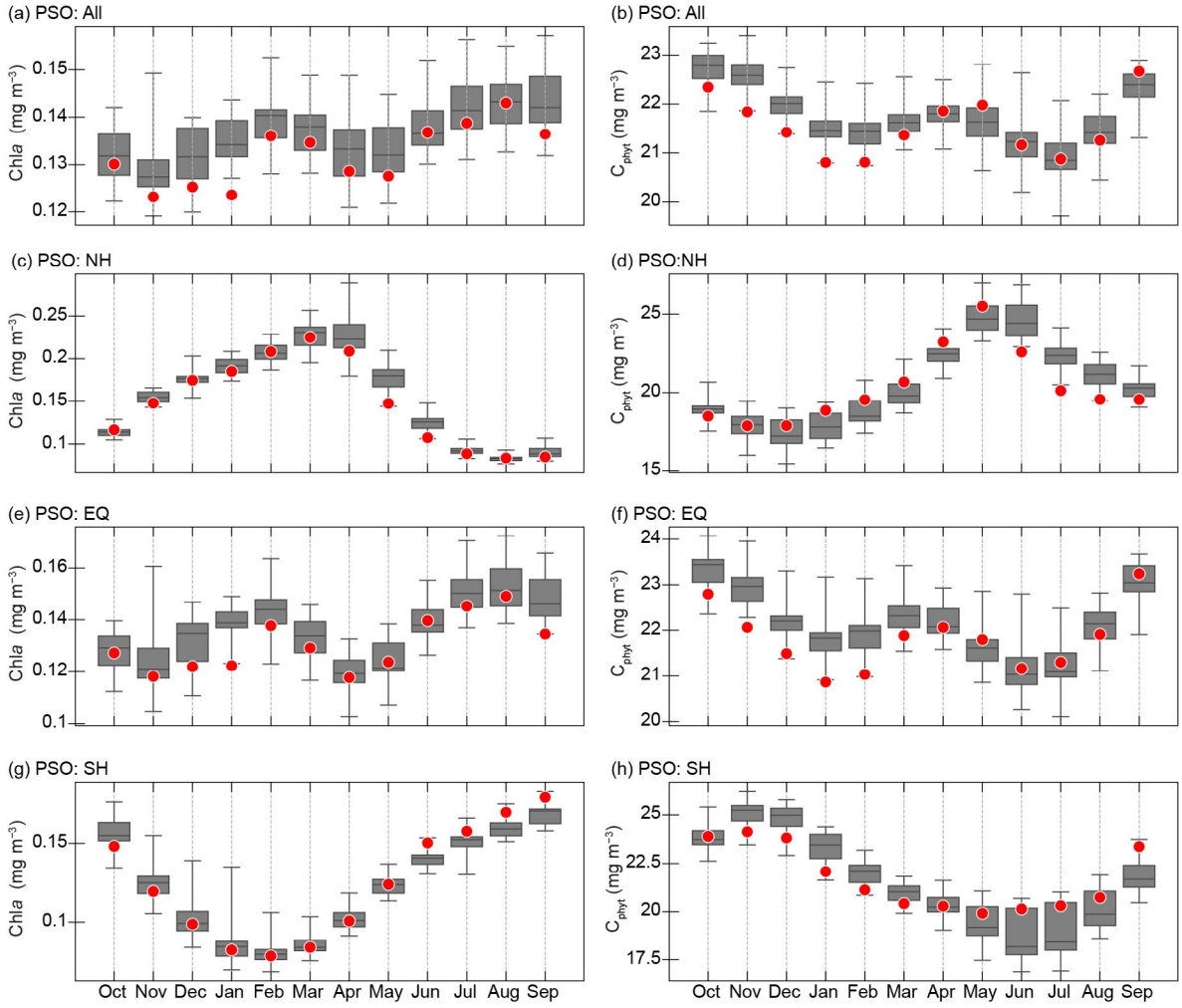

Fig. 3.26. Distribution of Oct 2023–Sep 2024 monthly means (red circles) for (a) VIIRS on NOAA-20 (VIIRS-N20) chlorophyll-*a* (Chl*a*) and (b) VIIRS-N20 phytoplankton carbon (C_{phy}) for the permanently stratified ocean (PSO) region (see Fig. 3.25), superimposed on the climatological values as derived from the combined time series of the Sea-Viewing Wide Field-of-View Sensor (SeaWiFS), Moderate Resolution Imaging Spectroradiometer on *Aqua* (MODIS-A), and Visible Infrared Imaging Radiometer Suite on NOAA-20 (VIIRS-N20) over the period of Oct 1998–Sep 2023. Gray boxes show the interquartile range of the climatology, with a black line for the median value and whiskers extending to minimum and maximum values. Subsequent panels show latitudinally segregated subsets of the PSO for the (c),(d) Northern Hemisphere above tropics (NH), (e),(f) tropical ±23.5° latitudes (EQ), and (g),(h) Southern Hemisphere below tropics (SH). Units for (a), (c), (e), and (g) are Chl*a* (mg m^{-3}) and (b), (d), (f), and (h) are C_{phy} (mg m^{-3}).

Over the 27-year time series of spatially averaged monthly mean Chl*a* within the PSO, concentrations vary by 5.7% (0.008 mg m^{-3}, standard deviation) around a long-term average of 0.136 mg m^{-3} (Fig. 3.27a). C_{phy} over the same 27-year period varies by 3.2% (0.69 mg m^{-3}) around an average of 21.8 mg m^{-3} (Fig. 3.27c). Chl*a* monthly anomalies within the PSO (Fig. 3.27b) vary by 4.5% (0.006 mg m^{-3}) over the multi-mission time series, with the largest deviations generally associated with El Niño-Southern Oscillation (ENSO) events (r = −0.39), as demonstrated by the correspondence of Chl*a* anomaly variations with the Multivariate ENSO Index (MEI; Wolter and Timlin 1998; presented in the inverse to illustrate the covariation). C_{phy} anomalies (Fig. 3.27d), which vary by 2.0% (0.43 mg m^{-3}), are less correlated with the MEI (r = −0.28) due to the inherent lag between environmental change, phytoplankton growth, and biomass accumulation. The mean anomalies in 2024 for Chl*a* and C_{phy} within the PSO indicate modestly depressed concentrations in the early part of the analysis year—consistent with El Niño conditions that limited

phytoplankton production—with concentrations returning to a nominal state following relaxation of El Niño forcings.

Through continuous ocean color monitoring, we can track changes in the global distribution of phytoplankton, which are crucial for driving biogeochemical processes, influencing the oceans' role in the global carbon cycle, and exerting control over marine ecosystems, food webs, and fisheries. Small fluctuations in Chl*a* and C_{phy} help with differentiating between climate-driven changes in phytoplankton biomass and shifts in their physiology and community dynamics. The recently launched Plankton, Aerosol, Cloud, ocean Ecosystem (PACE) mission, which is equipped with the first global hyperspectral instrument for ocean color measurement, is expected to improve the identification of phytoplankton absorption features (Werdell et al. 2019). This instrument will also help separate these features from non-algal optical signals (e.g., Pahlevan et al. 2021; Siegel et al. 2005), enabling more accurate assessments of phytoplankton species and community composition changes (e.g., Cetinić et al. 2024). These advancements will result in enhanced capacity to understand the impacts of climate forces on global phytoplankton communities.

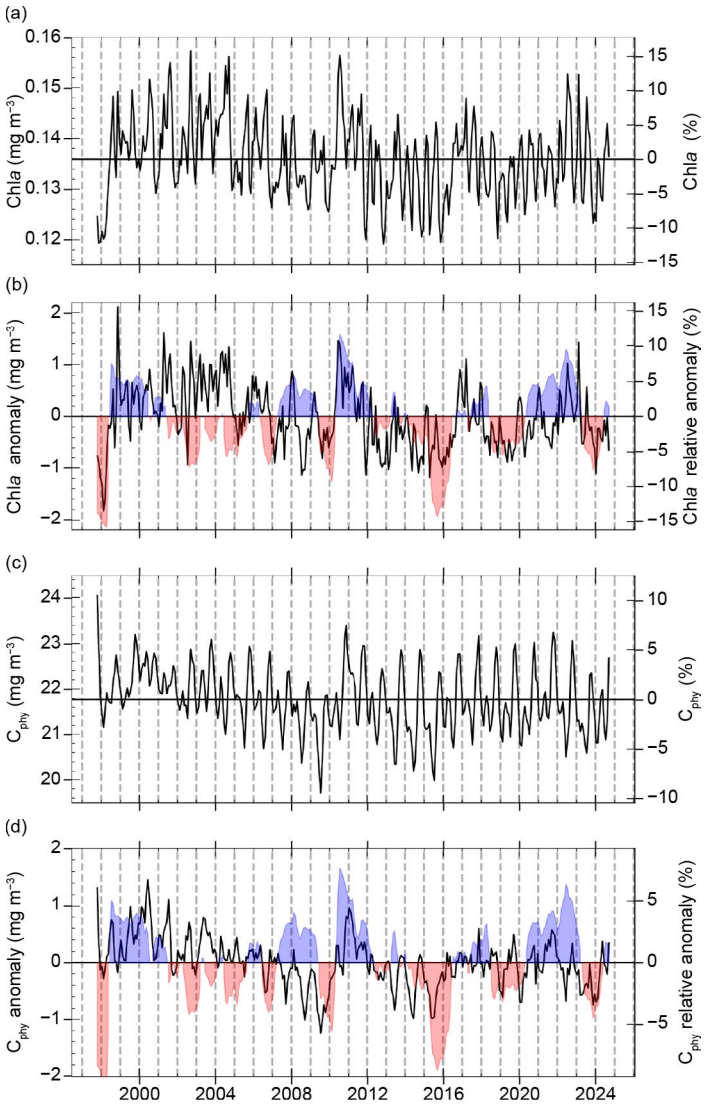

Fig. 3.27. Twenty-seven-year, multi-mission record of chlorophyll-*a* (Chl*a*; mg m^{-3}) and phytoplankton carbon (C_{phy}; mg m^{-3}) averaged over the permanently stratified ocean (PSO; Oct 1997–Sep 2024). (a) Monthly Chl*a*, with the horizontal line indicating the multi-mission mean Chl*a* concentration for the entire PSO region. (b) Monthly Chl*a* anomalies after subtraction of the multi-mission climatological mean (Fig. 3.26a). (c) Monthly C_{phy}, with the horizontal line indicating the multi-mission mean C_{phy} concentration for the entire PSO region. (d) Monthly C_{phy} anomalies after subtraction of the multi-mission climatological mean (Fig. 3.26b). Shaded blue and red colors show the Multivariate El Niño–Southern Oscillation Index, inverted and scaled to match the range of the Chl*a* and C_{phy} anomalies, where blue indicates La Niña and red indicate El Niño conditions.

j. Global ocean carbon cycle

—A. Jersild, R. Wanninkhof, J. A. Triñanes, P. Landschützer, R. A. Feely, and B. R. Carter

1. INTRODUCTION

The oceans play a major role in the global carbon cycle by taking up a substantial fraction of the excess carbon dioxide that humans release into the atmosphere. As a consequence of humankind's collective carbon dioxide (CO_2) release into the atmosphere, referred to as anthropogenic CO_2 (C_{ant}) emissions, the atmospheric CO_2 concentration has risen from pre-industrial levels of about 278 ppm (parts per million) to 422.5 ppm in 2024 (see section 2g1 for details). Marine C_{ant} is the primary cause of anthropogenic ocean acidification. Over the last decade, the global ocean has continued to take up C_{ant}, and therefore is a major mediator of global climate change. Of the 10.8±0.9 Pg C yr^{-1} C_{ant} released during the period 2014–23, 2.9±0.4 Pg C yr^{-1} (27%) accumulated in the ocean, 3.2±0.9 Pg C yr^{-1} (30%) accumulated on land, and 5.2±0.02 Pg C yr^{-1} (48%) remained in the atmosphere, with an imbalance of −0.4 Pg C yr^{-1} (−4%; see Table 7 in Friedlingstein et al. 2025). This decadal C_{ant} uptake estimate by the ocean is a consensus view from a combination of measured ocean decadal CO_2 inventory changes, global ocean biogeochemical models, and global air–sea CO_2 flux estimates based on surface ocean fugacity of CO_2 (fCO_{2w})[1] measurements.

The ocean interior is more challenging to observe than the surface ocean, leading to reduced temporal and spatial coverage relative to surface ocean fCO_2. Machine-learning gap filling techniques are employed to provide increased resolution of interior C_{ant} estimates. An example includes Carter et al. (2024), which overall agrees with estimates given by Friedlingstein et al. (2025), but suggests lower seasonal and interannual variability in the interior. Results demonstrate that the changes in the total carbon ocean inventory ($C_{inventory}$) can be primarily attributable to air–sea CO_2 flux and riverine inorganic carbon inputs. These estimates, however, are derived from expected patterns based on measurements that predate 2024.

2. AIR–SEA CARBON DIOXIDE FLUXES

Ocean uptake of CO_2 is estimated from the net air–sea CO_2 flux derived from a bulk flux formula determined from the product of the difference of air and surface seawater fCO_2 (ΔfCO_2) and gas transfer coefficients. Gas transfer is parameterized with wind, described in Wanninkhof (2014). This calculation provides a net flux estimate. Here, 0.65 Pg C yr^{-1} is applied as the river adjustment (Regnier et al. 2022) as recommended in the Global Carbon Budget 2024. The data sources for fCO_{2w} are annual updates of observations from the Surface Ocean CO_2 Atlas (SOCAT) composed of moorings, autonomous surface vehicles, and ship-based observations (Bakker et al. 2016), with SOCAT v2024 containing 38.6 million data points from 1957 through 2023 (Bakker et al. 2024). The increased observations and improved mapping techniques, including machine learning methods summarized in Rödenbeck et al. (2015), provide annual global fCO_{2w} fields on a 1° latitude × 1° longitude grid at monthly time scales. For this report, we use the self-organizing maps feed-forward neural network (SOM-FNN) approach of Landschützer et al. (2013, 2014), using SOCATv2024 for training. The monthly 2024 fCO_{2w} maps use as predictor variables: sea surface temperature (SST; Rayner et al. 2003); chlorophyll-*a* (Globcolour; Maritorena et al. 2010); mixed-layer depth (de Boyer Montégut et al. 2004 merged with Schmidtko et al. 2013), and salinity (Good et al. 2013). For atmospheric CO_2, the zonally resolved NOAA marine boundary layer atmospheric CO_2 product is used (Lan et al. 2023). The gas transfer coefficients are determined using ERA5 winds (Hersbach et al. 2018). The air–sea CO_2 flux maps for 2024 do not include fCO_{2w} observations for 2024 that have a year's latency but rather are created by extrapolation using the predictor variables. The uptake of the fCO_2-based models such as the Flanders Marine Institute (VLIZ) SOM-FNN used here is larger than the model-based estimates, with differences in uptake of ≈0.3 Pg C in 2023. This difference has decreased in recent years and is within the uncertainty of the approaches.

The VLIZ SOM-FNN results (Fig. 3.28) show a steady ocean CO_2 sink (S_{ocean}) from 1982 to 1998, followed by a period of decreasing uptake from 1998 to 2002. There is a strong increase in the ocean sink from 2002 onward that continues through 2016, after which the global uptake

[1] The fugacity is the partial pressure of CO_2 (pCO_2) corrected for non-ideality. They are numerically similar for surface waters with $fCO_2 \approx 0.994\ pCO_2$.

decreases substantially until 2024. The C_{ant} flux of 2.7 Pg C yr^{-1} for 2024 (green line in Fig. 3.28) shows a ≈1 Pg C decrease in uptake below the 2014–23 average of 3.7±0.31 Pg C yr^{-1}. The amplitude of seasonal variability is ≈2.3 Pg C with a minimum uptake in June–September.

Sea surface temperature anomalies can manifest themselves in differing ways on fCO_{2w}. Positive SST anomalies will decrease solubility and thereby increase fCO_{2w}. However, in regions with high fCO_{2w} due to upwelling, warmer SSTs will lower fCO_{2w} as a result of decreased upwelling of cold, CO_2-rich water.

The annual average flux map for 2024 (Fig. 3.29a) shows the characteristic pattern of high effluxes (ocean-to-air CO_2 fluxes) in tropical, coastal upwelling, and open ocean upwelling regions. Coastal upwelling regions include those in the Arabian Sea and off the west coasts of North and South America, along with West Africa. The western Bering Sea was a strong CO_2 source in 2024, a clear juxtaposition to the strong sink in the surrounding regions. This regional source is hypothesized to result from a local outcropping of shallow isopycnals with high CO_2 values; however, this has not been independently verified. Cumulatively, the regions of effluxes are substantial CO_2 sources to the atmosphere (≈1 Pg C). The primary CO_2 uptake regions are in the subtropical and subpolar regions. The largest sinks are poleward of the sub-tropical fronts. In the Southern Ocean, the area near the polar front (~60°S) was a weak to moderate sink in 2024, with a source closer to the Antarctic coast along the lower latitudes Southern Ocean. This source was not apparent in the previous iteration (see Fig, 3.28a in last year's report) but rather than a physical phenomenon, is attributed to new observations in the region and changes in the source of predictor variables used in the approach.

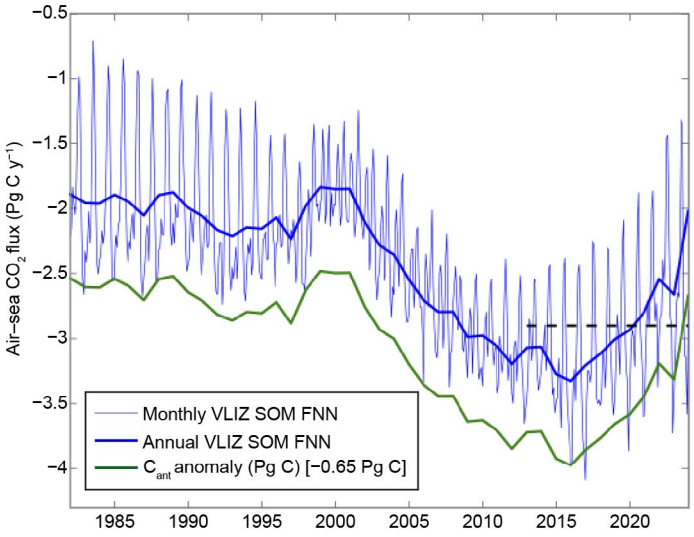

Fig. 3.28. Global annual (thick blue line) and monthly (thin blue line) net air–sea carbon dioxide (CO_2) fluxes (Pg C yr^{-1}) for the period 1982–2024 using the Flanders Marine Institute (VLIZ) self-organizing maps feed-forward neural network (SOM-FFN) output. The annual anthropogenic CO_2 (C_{ant}) air–sea flux (solid green line) includes the riverine adjustment of –0.65 Pg C. Black dashed line is the 2014–23 mean C_{ant} flux based on models and data-based products (Friedlingstein et al. 2025). Negative values indicate CO_2 uptake by the ocean.

In the Northern Hemisphere, the entire North Atlantic is a large sink, while in the North Pacific the sink region is punctuated by a substantial source of CO_2 in the western subpolar North Pacific and the central Bering Sea. The Northern Hemisphere sinks are in part due to the position of the western boundary currents, whose cooling waters when transported poleward cause an increase in solubility and contribute to CO_2 uptake at high latitudes. The Gulf Stream/North Atlantic Drift in the Atlantic extends farther north than the Kuroshio in the Pacific, extending the region of a strong sink in the North Atlantic poleward.

The ocean carbon uptake anomalies (Fig. 3.29c) in 2024 relative to the 1990–2020 average, adjusted for the 20-year trend, show the effect of the El Niño condition in the second half of 2023 lasting through spring 2024, with reduced upwelling and lower effluxes of CO_2 in the eastern equatorial Pacific (EEP). The Southern Ocean shows overall reduced uptake (~60°S–45°S) when compared to the 20-year trend, although the larger region is still overall an ocean sink. This reduction in uptake, which is nearly 50% smaller than previous estimates, is likely due to a combination of temporal variation, methodological improvements, and data sparsity in the region (Hauck et al. 2023).

The spatial differences in CO_2 fluxes between 2024 and 2023 (Fig. 3.29b) show predominant orange shaded regions depicting more efflux, or less influx, leading to a substantially smaller CO_2 uptake by the ocean in 2024 (Fig. 3.28). The eastern and central equatorial Pacific shows regions of more outgassing right along the equator in 2024 compared to 2023 and more uptake,

or less outgassing, immediately to the north. The increased efflux along the equator reflects the residual impacts of the El Niño that lingered into early 2024, leading to a reduced uptake in the EEP. The regions of increased effluxes or decreased influxes in the Northern Hemisphere correspond with the positive SST anomalies in the boreal summer, which often correspond with regions with marine heatwaves. The strong source in the western subpolar North Pacific and Bering Sea (Fig 3.29a) shows up as a positive anomaly compared to the long-term average, similar to the anomaly observed in 2023.

3. OCEAN INTERIOR INVENTORY ESTIMATES

The ocean inventory of dissolved inorganic carbon (DIC) varies over time due to surface CO_2 fluxes, interior ocean cycling of organic matter, riverine inputs, and sedimentary exchanges. While this variability can be monitored directly using ship-based measurements, the ocean interior is more challenging to observe than the surface ocean. There is, therefore, less spatial and temporal coverage of these measurements than surface ocean fCO_2 observations. For this reason, interior ocean DIC observations are primarily used in decadal retrospective analyses that quantify the accumulation of C_{ant} throughout the ocean.

As with surface ocean fCO_2 observations, machine learning gap-filling techniques are now being used to map the available measurements onto data products that have better spatial and temporal resolution (Keppler et al. 2023). Here (Fig. 3.30) we use the Empirical Seawater Property Estimation Routines (ESPERs: Carter et al. 2021) to project DIC onto the temperature and salinity climatology of Roemmich and Gilson (2009), which is supplemented for deep and high-latitude regions using the static climatology from Lauvset et al. (2016). Recent methods for estimating the time-varying C_{ant} in the ocean interior (Carter et al. 2024) allow the $C_{inventory}$ estimates and their year-to-year increases (attributable primarily to S_{ocean}) to be separated into natural variations (ΔC_{nat}) and anthropogenic accumulation (ΔC_{ant}).

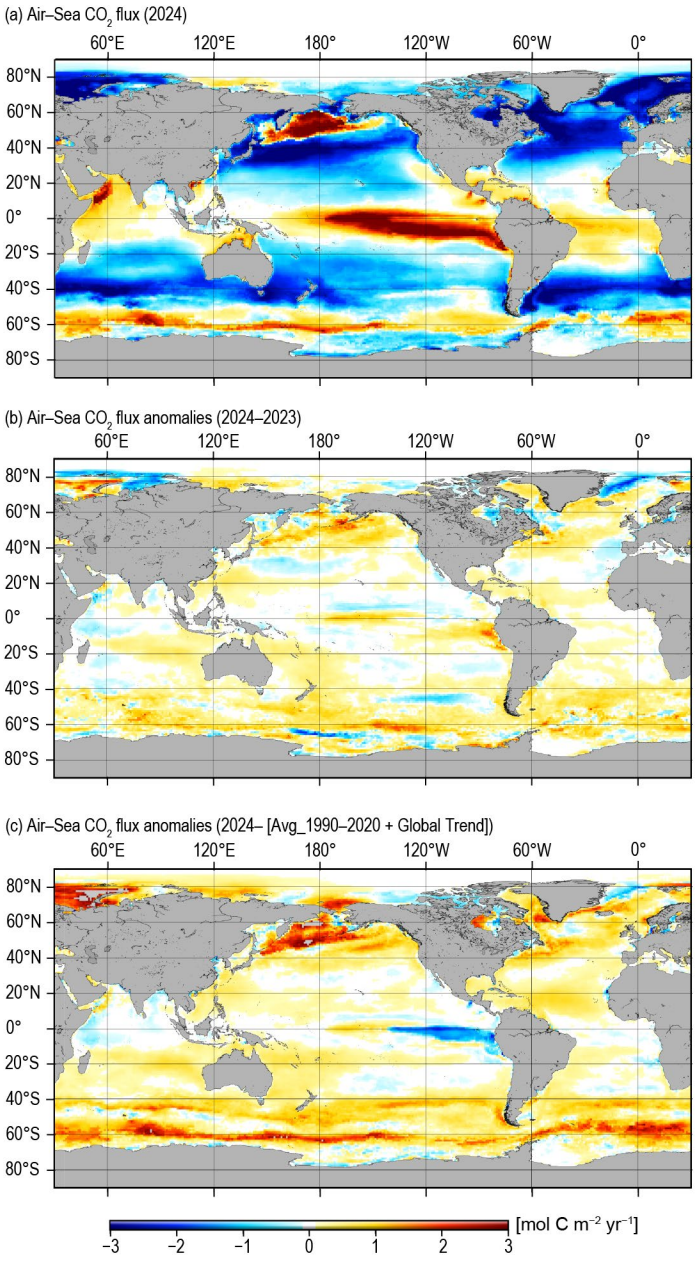

Fig. 3.29. Global map of (a) net air–sea carbon dioxide (CO_2) fluxes for 2024, (b) net air–sea CO_2 flux anomalies for 2024 minus 2023, and (c) net air–sea CO_2 flux anomalies for 2024 relative to 1990–2020 average values, adjusted for the 20-year trend using the Flanders Marine Institute (VLIZ) self-organizing maps feed-forward neural network (SOM-FNN) approach. Units are all mol C m^2 yr^{-1}. Ocean CO_2 uptake regions are shown in blue. For reference, a global ocean CO_2 uptake of 2.8 Pg C yr^{-1} equals a flux density of –0.65 mol C m^2 yr^{-1}.

These ocean inventory change estimates show substantial seasonal variability attributable to C_{nat} (Fig. 3.30a). There is a maximum in the rate of estimated $C_{inventory}$ accumulation each austral winter when the larger ocean areas of the Southern Hemisphere are cooling, followed by warming and release of CO_2 to the atmosphere in the austral summer. Substantial interannual variability in the $C_{inventory}$ can still be seen when the changes are averaged over annual cycles (Fig. 3.30b). This variability is also attributable to C_{nat} variability. The C_{ant} changes are relatively steady from year to year, and the variations generally oppose the much larger variations in the C_{nat}. This

anticorrelation results when increases in ocean overturning generate anomalous loss of deep carbon accumulated from organic matter respiration and anomalous uptake of C_{ant} with ventilation of older waters (DeVries et al. 2017).

The changes in the $C_{inventory}$ are primarily attributable to the air–sea CO_2 flux and riverine inorganic carbon inputs, allowing a comparison to be made between the black bars in Fig. 3.30b and the green line in Fig. 3.28. These methods suggest several differences: the mean inventory uptake estimate is lower over the 2014–23 period at a rate of 2.9 Pg C yr^{-1} compared to the 3.7 (±0.31) Pg C yr^{-1} estimate from air–sea fluxes. The seasonal and interannual variability in the estimates is also notably greater in the inventory estimates, yet the inventory estimates do not show the recent (post-2016) relaxation of ocean CO_2 uptake. There is also an indication that there was an anomalously low $C_{inventory}$ increase in 2023 of 0.8 Pg C yr^{-1}, consistent with strong upwelling from the persistent La Niña that concluded in that year, whereas 2024 shows an increase of 3.9 Pg C that is similar to the estimated 2024 C_{ant} accumulation of 3.7 Pg C.

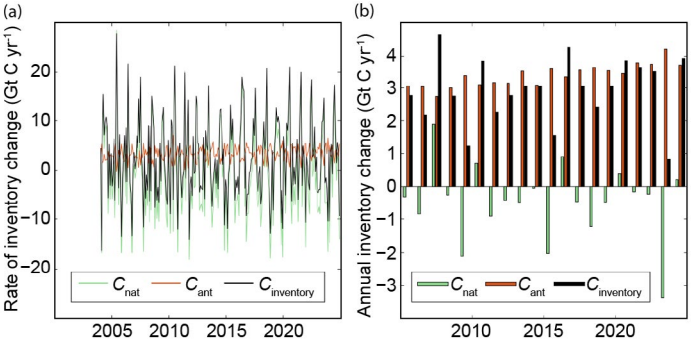

Fig. 3.30. Time series of the rate of inventory change in the total dissolved inorganic carbon ocean inventory ($C_{inventory}$), the change attributable to anthropogenic carbon accumulation (ΔC_{ant}), and the residual between these values attributed to natural processes (C_{nat}). Units are Gt C yr^{-1}.

Ocean interior inventory mapping can take advantage of regular updates to the underlying climatologies to provide timely and detailed information about ocean carbon inventory variations. However, as of yet, these estimates solely provide projections of expected patterns based on DIC measurements that predate 2024 and rely on the Argo-array-dominated temperature and salinity patterns from 2024 to generate the estimates for the most recent years. Furthermore, the methodological uncertainties for this approach have yet to be quantified.

Acknowledgments

Sandra Bigley provided invaluable assistance in assembling the sections of this chapter and copyediting.

Appendix 1: Acronyms

ACC	Antarctic Circumpolar Current
BASS	Blended Analysis of Surface Salinity
b_{bp}	particle backscattering coefficient
C_{ant}	anthropogenic CO_2
CAS	Chinese Academy of Sciences
Chl*a*	chlorophyll-*a*
$C_{inventory}$	changes in the total ocean inventory
C_{nat}	natural variations of CO_2
CO_2	carbon dioxide
C_{phy}	phytoplankton carbon
CTD	Conductivity-Temperature-Depth
DCENT	Dynamically Consistent ENsemble of Temperature
DIC	dissolved inorganic carbon
DOISST	Daily OISST
E	Evaporation
EEP	eastern equatorial Pacific
ENSO	El Niño–Southern Oscillation
ESPERs	Empirical Seawater Property Estimation Routines
FC	Florida Current
fCO_{2w}	surface ocean fugacity of CO_2
FLASHFlux	Fast Longwave And Shortwave Radiative Fluxes
GIA	glacial isostatic adjustment
GMSL	global mean sea level
GRACE	Gravity Recovery and Climate Experiment
GRACE-FO	GRACE Follow-On
GTMBA	Global Tropical Moored Buoy Array
HadSST	Hadley Centre Sea Surface Temperature
IAP	Institute of Atmospheric Physics
IOD	Indian Ocean dipole
ITCZ	Intertropical Convergence Zone
JP24	Johnson and Purkey 2024
JPL	Jet Propulsion Laboratory
LH	latent heat flux
LW	longwave radiation
MBT	mechanical bathythermograph
MCS	marine cold spell
MEI	Multivariate ENSO Index
MHT	meridional heat transport
MHW	marine heatwave
MOC	meridional overturning circulation
MODIS-A	Moderate Resolution Imaging Spectroradiometer on *Aqua*
MOVE	Meridional Overturning Variability Experiment
NECC	North Equatorial Countercurrent
NH	Northern Hemisphere
OHCA	ocean heat content anomaly
ORAS5	Ocean ReAnalysis System 5
OSNAP	Overturning in the Subpolar North Atlantic Program
P	precipitation
PACE	Plankton, Aerosol, Cloud, ocean Ecosystem

$_pCO_2$	partial pressure of CO_2
PDO	Pacific Decadal Oscillation
PMEL	Pacific Marine Environmental Laboratory
PSO	permanently stratified ocean
PSS-78	Practical Salinity Scale-78
Q_{net}	net surface heat flux
RFROM	Random Forest Regression Ocean Maps
SAMBA	South Atlantic MOC Basin-wide Array
SH	sensible heat
SH	Southern Hemisphere
SIO	Scripps Institution of Oceanography
SMAP	Soil Moisture Active Passive
SMOS	Soil Moisture and Ocean Salinity
SOCAT	Surface Ocean CO_2 Atlas
S_{ocean}	steady ocean CO_2 sink
SOM-FNN	self-organizing maps feed-forward neural network
SPCZ	South Pacific Convergence Zone
SSS	sea surface salinity
SST	sea surface temperature
SSTA	sea surface temperature anomaly
SW	shortwave radiation
TAO	Tropical Atmosphere Ocean
TIW	tropical instability waves
VIIRS-N20	Visible Infrared Imaging Radiometer Suite on NOAA-20
VLIZ	Flanders Marine Institute
W_{EK}	Ekman vertical velocity
WMO	World Meteorological Organization
WOA 2023	World Ocean Atlas 2023
XBT	Expendable Bathythermograph
ΔfCO_2	fCO_2 difference
ΔC_{ant}	anthropogenic accumulation
ΔC_{nat}	natural variations

Appendix 2: Datasets and sources

Section 3b Sea surface temperature

Sub-section	General Variable or Phenomenon	Specific Dataset or Variable	Source
3b	Sea Surface Temperature	ERSSTv5	https://doi.org/10.7289/V5T72FNM
3b	Sea Surface Temperature	Hadley Centre Sea Surface Temperature Dataset (HadSST) Version 4	https://www.metoffice.gov.uk/hadobs/hadsst4/
3b	Sea Surface Temperature	NOAA Daily Optimum Interpolated Temperature (DOISST) Version 2.1	https://doi.org/10.25921/RE9P-PT57
3b	Sea Surface Temperature	Dynamically Consistent ENsemble of Temperature (DCENT) Version 1.0	https://www.ospo.noaa.gov/products/ocean/sst/contour/

Section 3c Ocean heat content

Sub-section	General Variable or Phenomenon	Specific Dataset or Variable	Source
3c	Ocean Heat Content	Random Forest Regression Ocean Maps (RFROM) Version 2	https://www.pmel.noaa.gov/rfrom/
3c	Ocean Heat Content	Argo	http://doi.org/10.17882/42182#98916
3c	Ocean Heat Content	Argo Monthly Climatology	https://sio-argo.ucsd.edu/RG_Climatology.html
3c	Ocean Heat Content	CLIVAR and Carbon Hydrographic Data Office	https://cchdo.ucsd.edu/
3c	Ocean Heat Content	University of Colorado/ Carnegie Mellon University (CU/CMU)	https://zenodo.org/records/10645137
3c	Ocean Heat Content	Institute of Atmospheric Physics (IAP)/Chinese Academy of Sciences (CAS)	http://www.ocean.iap.ac.cn/pages/dataService/dataService.html
3c	Ocean Heat Content	Meteorological Research Institute (MRI)/Japan Meteorological Agency (JMA)	https://www.data.jma.go.jp/kaiyou/english/ohc/ohc_global_en.html
3c	Ocean Heat Content	NCEI	https://www.ncei.noaa.gov/access/global-ocean-heat-content/

Sub-section	General Variable or Phenomenon	Specific Dataset or Variable	Source
3c	Ocean Heat Content	Pacific Marine Environmental Laboratory (PMEL)/Jet Propulsion Laboratory (JPL)/ Cooperative Institute for Marine and Atmospheric Research (CIMAR)	https://www.pmel.noaa.gov/rfrom/
3c	Ocean Heat Content	UK Met Office EN4.2.2	https://www.metoffice.gov.uk/hadobs/en4/download-en4-2-2.html

Section 3d Salinity

Sub-section	General Variable or Phenomenon	Specific Dataset or Variable	Source
3d2	Ocean Salinity	Aquarius Version 3.0	http://podaac.jpl.nasa.gov/aquarius
3d2	Ocean Salinity	Argo	https://usgodae.org/argo/argo.html
3d2	Ocean Salinity	Blended Analysis for Surface Salinity	ftp://ftp.cpc.ncep.noaa.gov/precip/BASS
3d2	Ocean Salinity	Soil Moisture Active Passive (SMAP)	https://podaac.jpl.nasa.gov/SMAP
3d2	Ocean Salinity	Soil Moisture Ocean Salinity (SMOS)	https://earth.esa.int/eogateway/missions/smos
3d2	Ocean Salinity	World Ocean Atlas 2023	https://www.ncei.noaa.gov/products/world-ocean-atlas
3d3	Ocean Salinity	NCEI Salinity Anomaly	https://www.ncei.noaa.gov/access/global-ocean-heat-content/

Section 3e Global ocean heat, freshwater, and momentum flux

Sub-section	General Variable or Phenomenon	Specific Dataset or Variable	Source
3e1	Air–Sea Fluxes (Shortwave/Longwave Radiation)	Clouds and the Earth's Radiant Energy System (CERES) Energy Balanced and Filled (EBAF) Version 4.2	https://asdc.larc.nasa.gov/project/CERES/CERES_EBAF_Edition4.2
3e1	Air–Sea Fluxes (Shortwave/Longwave Radiation)	CERES FlashFlux	https://cmr.earthdata.nasa.gov/search/concepts/C1719147151-LARC_ASDC.html
3e1	Air–Sea Fluxes (Latent Heat/Sensible Heat)	Objectively Analyzed Air–Sea Heat Fluxes (OAFlux2)	https://oaflux.whoi.edu/
3e2	Evaporation	OAFLux2	https://oaflux.whoi.edu/

Sub-section	General Variable or Phenomenon	Specific Dataset or Variable	Source
3e2	Precipitation	GPCPv2.3	https://psl.noaa.gov/data/gridded/data.gpcp.html
3e3	Wind Stress	OAFlux2	https://oaflux.whoi.edu/

Section 3f Sea Level variability and change

Sub-section	General Variable or Phenomenon	Specific Dataset or Variable	Source
3f	Ocean Heat Content	Argo Monthly Climatology	https://sio-argo.ucsd.edu/RG_Climatology.html
3f	Ocean Mass	Gravity Recovery and Climate Experiment (GRACE)/Grace Follow-On (GRACE-FO)	https://grace.jpl.nasa.gov/data/get-data
3f	Sea Level / Sea Surface Height	Argo	https://usgodae.org/argo/argo.html
3f	Sea Level / Sea Surface Height	NASA Making Earth Science Data Records for Use in Research Environments (MEaSURES)	https://podaac.jpl.nasa.gov/dataset/SEA_SURFACE_HEIGHT_ALT_GRIDS_L4_2SATS_5DAY_6THDEG_V_JPL2205
3f	Sea Level / Sea Surface Height	NASA Sea Level Change and Ocean Surface Topography Program	https://sealevel.nasa.gov/data_tools/16/
3f	Sea Level / Sea Surface Height	Copernicus Climate Change Service (C3S) Altimetry Data	https://climate.copernicus.eu/sea-level
3f	Sea Level / Sea Surface Height	Tide Gauge	http://uhslc.soest.Hawai'i.edu/

Section 3g Surface currents

Sub-section	General Variable or Phenomenon	Specific Dataset or Variable	Source
3g	Ocean Currents	Global Tropical Moored Buoy Array (GTMBA)	https://www.pmel.noaa.gov/gtmba/
3g3	Ocean Currents	Atlantic Ocean Monitoring	https://www.aoml.noaa.gov/phod/altimetry/cvar/
3g	Surface Velocity	Drifter/Altimetry/Wind Synthesis Product	https://www.aoml.noaa.gov/ftp/pub/phod/lumpkin/decomp/

Section 3h Meridional overturning circulation and heat transport in the Atlantic Ocean

Sub-section	General Variable or Phenomenon	Specific Dataset or Variable	Source
3h	Ocean Currents	Atlantic Ship of Opportunity Expendable Bathythermograph (XBT)	https://www.aoml.noaa.gov/phod/goos/xbt_network/
3h	Ocean Currents	Argo	https://usgodae.org/argo/argo.html
3h	Ocean Currents	Florida Current Transport	https://www.aoml.noaa.gov/phod/floridacurrent/data_access.php
3h	Ocean Currents	Global Temperature and Salinity Profile Program (GTSPP)	https://www.ncei.noaa.gov/products/global-temperature-and-salinity-profile-programme
3h	Ocean Currents	Meridional Overturning Variability Experiment (MOVE) array	https://mooring.ucsd.edu/move/
3h	Ocean Currents	Overturning in the Subpolar North Atlantic Program (OSNAP)	https://www.o-snap.org/
3h	Ocean Currents	RAPID–Meridional Overturning Circulation and Heat-flux Array–Western Boundary Time Series (RAPID)	https://rapid.ac.uk/rapidmoc/
3h	Ocean Currents	South Atlantic MOC Basin-wide Array (SAMBA)	https://www.aoml.noaa.gov/phod/research/moc/samoc/sam/

Section 3i Global ocean phytoplankton

Sub-section	General Variable or Phenomenon	Specific Dataset or Variable	Source
3i	Daytime Sea Surface Temperature	Moderate Resolution Imaging Spectroradiometer on *Aqua* (MODIS-A) Version R2022.0	https://oceancolor.gsfc.nasa.gov/data/reprocessing/r2022/aqua/
3i	Phytoplankton Chlorophyll Particle Backscattering Coefficient	MODIS-A	https://modis.gsfc.nasa.gov/data/dataprod/chlor_a.php
3i	Phytoplankton Chlorophyll Particle Backscattering Coefficient	Sea-viewing Wide Field-of-view Sensor (SeaWiFS) Version R2022.0	https://oceancolor.gsfc.nasa.gov/data/reprocessing/r2022/seawifs/
3i	Phytoplankton Chlorophyll Particle Backscattering Coefficient	Visible Infrared Imaging Radiometer Suite (VIIRS)-NOAA20 Version R2022.0	https://data.nasa.gov/dataset/noaa-20-viirs-global-mapped-chlorophyll-chl-nrt-data-version-r2022-0

Section 3j Global ocean carbon cycle			
Sub-section	**General Variable or Phenomenon**	**Specific Dataset or Variable**	**Source**
3j2	Atmospheric Carbon Dioxide	NOAA Greenhouse Gas Marine Boundary Layer Reference	https://gml.noaa.gov/ccgg/mbl/mbl.html
3j2	Chlorophyll	GlobColour	https://www.globcolour.info/
3j2	Mixed Layer Depth	de Boyer Montegut (2004; 2023 update); Monthly Isopycnal & Mixed-layer Ocean Climatology (MMOC)	https://www.seanoe.org/data/00806/91774/; https://www.pmel.noaa.gov/mimoc/
3j2	Ocean Carbon	Surface Ocean CO_2 Atlas (SOCAT) Version 2024	https://socat.info/index.php/data-access/
3j2	Ocean Salinity	Hadley Center EN4	https://www.metoffice.gov.uk/hadobs/en4/
3j3	Ocean Salinity	Argo Monthly Climatology	https://sio-argo.ucsd.edu/RG_Climatology.html
3j3	Ocean Temperature	Argo Monthly Climatology	https://sio-argo.ucsd.edu/RG_Climatology.html
3j2	Sea Surface Temperature	NOAA OISST Version 2.1	https://www.ncei.noaa.gov/products/optimum-interpolation-sst
3j2	Winds [Near] Surface	ERA5	https://www.ecmwf.int/en/forecasts/dataset/ecmwf-reanalysis-v5

References

Adler, R. F., and Coauthors, 2018: The Global Precipitation Climatology Project (GPCP) monthly analysis (new version 2.3) and a review of 2017 global precipitation. *Atmosphere*, **9**, 138, https://doi.org/10.3390/atmos9040138.

Bakker, D. C. E., and Coauthors, 2016: A multi-decade record of high-quality fCO_2 data in version 3 of the Surface Ocean CO_2 Atlas (SOCAT). *Earth Syst. Sci. Data*, **8**, 383–413, https://doi.org/10.5194/essd-8-383-2016.

——, and Coauthors, 2024: Surface Ocean CO_2 Atlas Database Version 2024 (SOCATv2024) (NCEI Accession 0293257), NOAA National Centers for Environmental Information [data set], https://doi.org/10.25921/9wpn-th28.

Balaguru, K., P. Chang, R. Saravanan, L. R. Leung, Z. Xu, M. Li, and J. S. Hsieh, 2012: Ocean barrier layers' effect on tropical cyclone intensification. *Proc. Natl. Acad. Sci. USA*, **109**, 14343–14347, https://doi.org/10.1073/pnas.1201364109.

Baringer, M. O., and J. C. Larsen, 2001: Sixteen years of Florida Current transport at 27°N. Geophys. *Res. Lett.*, **28**, 3179–3182, https://doi.org/10.1029/2001GL013246.

——, and Coauthors, 2015: Meridional overturning circulation observations in the North Atlantic Ocean [in "State of the Climate in 2014"]. *Bull. Amer. Meteor. Soc.*, **96**, S78–S80, https://doi.org/10.1175/2015BAMSStateoftheClimate.1.

Barroso, A., T. Wahl, S. Li, A. Enriquez, J. Morim, S. Dangendorf, C. Piecuch, and P. Thompson, 2024: Observed spatiotemporal variability in the annual sea level cycle along the global coast. *J. Geophys. Res. Oceans*, **129**, e2023JC020300, https://doi.org/10.1029/2023JC020300.

Beckley, B., and Coauthors, 2024: Global mean sea level trend from integrated multi-mission ocean altimeters TOPEX/Poseidon, Jason-1, OSTM/Jason-2, Jason-3, and Sentinel-6 version 5.2. PO.DAAC, accessed 5 February 2025, https://doi.org/10.5067/GMSLM-TJ152.

Behrenfeld, M. J., and Coauthors, 2001: Biospheric primary production during an ENSO transition. *Science*, **291**, 2594–2597, https://doi.org/10.1126/science.1055071.

——, and Coauthors, 2006: Climate-driven trends in contemporary ocean productivity. *Nature*, **444**, 752–755, https://doi.org/10.1038/nature05317.

——, and Coauthors, 2016: Revaluating ocean warming impacts on global phytoplankton. *Nat. Climate Change*, **6**, 323–330, https://doi.org/10.1038/nclimate2838.

Caron, L., and E. R. Ivins, 2020: A baseline Antarctic GIA correction for space gravimetry. *Earth Planet. Sci. Lett.*, **531**, 115957, https://doi.org/10.1016/j.epsl.2019.115957.

Carter, B. R., and Coauthors, 2021: New and updated global empirical seawater property estimation routines. *Limnol. Oceanogr. Methods*, **19**, 785–809, https://doi.org/10.1002/lom3.10461.

——, J. Schwinger, R. Sonnerup, A. J. Fassbender, J. D. Sharp, and L. M. Dias, 2025: Tracer-based Rapid Anthropogenic Carbon Estimation (TRACE). *Earth Syst. Sci. Data*, https://doi.org/10.5194/essd-2024-560, in press.

Cetinić, I., M. J. Perry, N. T. Briggs, E. Kallin, E. A. D'Asaro, and C. M. Lee, 2012: Particulate organic carbon and inherent optical properties during 2008 North Atlantic Bloom Experiment. *J. Geophys. Res.*, **117**, C06028, https://doi.org/10.1029/2011JC007771.

——, and Coauthors, 2024: Phytoplankton composition from sPACE: Requirements, opportunities, and challenges. *Remote Sens. Environ.*, **302**, 113964, https://doi.org/10.1016/j.rse.2023.113964.

Chambers, D. P., A. Cazenave, N. Champollion, H. Dieng, W. Llovel, R. Forsberg, K. von Schuckmann, and Y. Wada, 2017: Evaluation of the global mean sea level budget between 1993 and 2014. *Surv. Geophys.*, **38**, 309–327, https://doi.org/10.1007/s10712-016-9381-3.

Chan, D., G. Gebbie, P. Huybers, and E. C. Kent, 2024: A Dynamically Consistent ENsemble of Temperature at the Earth surface since 1850 from the DCENT dataset. *Sci. Data*, **11**, 953, https://doi.org/10.1038/s41597-024-03742-x.

Chavez, F. P., M. Messié, and J. T. Pennington, 2011: Marine primary production in relation to climate variability and change. *Ann. Rev. Mar. Sci.*, **3**, 227–260, https://doi.org/10.1146/annurev.marine.010908.163917.

Cheng, L., J. Zhu, R. Cowley, T. Boyer, and S. Wijffels, 2014: Time, probe type, and temperature variable bias corrections to historical expendable bathythermograph observations. *J. Atmos. Oceanic Technol.*, **31**, 1793–1825, https://doi.org/10.1175/JTECH-D-13-00197.1.

——, and Coauthors, 2025: Record high temperatures in the ocean in 2024. *Adv. Atmos. Sci.*, **42**, 1092–1109, https://doi.org/10.1007/s00376-025-4541-3.

de Boyer Montégut, C., G. Madec, A. S. Fischer, A. Lazar, and D. Ludicone, 2004: Mixed layer depth over the global ocean: An examination of profile data and a profile-based climatology. *J. Geophys. Res.*, **109**, C12003, https://doi.org/10.1029/2004JC002378.

Deser, C., M. A. Alexander, S. P. Xie, and A. S. Phillips, 2010: Sea surface temperature variability: Patterns and mechanisms. *Ann. Rev. Mar. Sci.*, **2**, 115–143, https://doi.org/10.1146/annurev-marine-120408-151453.

DeVries, T., M. Holzer, and F. Primeau, 2017: Recent increase in oceanic carbon uptake driven by weaker upper-ocean overturning. *Nature*, **542**, 215–218, https://doi.org/10.1038/nature21068.

Dierssen, H. M., 2010: Perspectives on empirical approaches for ocean color remote sensing of chlorophyll in a changing climate. *Proc. Natl. Acad. Sci. USA*, **107**, 17073–17078, https://doi.org/10.1073/pnas.0913800107.

Domingues, R., G. Goni, M. Baringer, and D. L. Volkov, 2018: What caused the accelerated sea level changes along the United States East Coast during 2010–2015? *Geophys. Res. Lett.*, **45**, 13367–13376, https://doi.org/10.1029/2018GL081183.

Dong, S., G. Goni, R. Domingues, F. Bringas, M. Goes, J. Christophersen, and M. Baringer, 2021: Synergy of in situ and satellite ocean observations in determining meridional heat transport in the Atlantic Ocean. *J. Geophys. Res. Oceans*, **126**, e2020JC017073, https://doi.org/10.1029/2020JC017073.

Donohoe, A., R. Fajber, T. Cox, K. C. Armour, D. S. Battisti, and G. H. Roe, 2024: Model biases in the atmosphere–ocean partitioning of poleward heat transport are persistent across three CMIP generations. *Geophys. Res. Lett.*, **51**, e2023GL106639, https://doi.org/10.1029/2023GL106639.

Durack, P. J., and S. E. Wijffels, 2010: Fifty-year trends in global ocean salinities and their relationship to broad-scale warming. *J. Climate*, **23**, 4342–4362, https://doi.org/10.1175/2010JCLI3377.1.

——, ——, and R. J. Matear, 2012: Ocean salinities reveal strong global water cycle intensification during 1950 to 2000. *Science*, **336**, 455–458, https://doi.org/10.1126/science.1212222.

Fablet, R., B. Chapron, J. Le Sommer, and F. Sévellec, 2024: Inversion of sea surface currents from satellite-derived SST-SSH synergies with 4DVarNets. *J. Adv. Model. Earth Syst.*, **16**, e2023MS003609, https://doi.org/10.1029/2023MS003609.

Fairall, C. W., E. F. Bradley, J. E. Hare, A. A. Grachev, and J. B. Edson, 2003: Bulk parameterization of air–sea fluxes: Updates and verification for the COARE algorithm. *J. Climate*, **16**, 571–591, https://doi.org/10.1175/1520-0442(2003)016<0571:BPOAS-F>2.0.CO;2.

Fasullo, J., R. Nerem, and B. Hamlington, 2016: Is the detection of accelerated sea level rise imminent?. *Sci. Rep.*, **6**, 31245, https://doi.org/10.1038/srep31245.

Field, C. B., M. J. Behrenfeld, J. T. Randerson, and P. Falkowski, 1998: Primary production of the biosphere: Integrating terrestrial and oceanic components. *Science*, **281**, 237–240, https://doi.org/10.1126/science.281.5374.237.

Fofonoff, N. P., and E. L. Lewis, 1979: A practical salinity scale. *J. Oceanogr. Soc. Japan*, **35**, 63–64, https://doi.org/10.1007/BF02108283.

Font, J., and Coauthors, 2013: SMOS first data analysis for sea surface salinity determination. *Int. J. Remote Sens.*, **34**, 3654–3670, https://doi.org/10.1080/01431161.2012.716541.

Fore, A. G., S. H. Yueh, W. Q. Tang, B. W. Stiles, and A. K. Hayashi, 2016: Combined active/passive retrievals of ocean vector wind and sea surface salinity with SMAP. *IEEE Trans. Geosci. Remote Sens.*, **54**, 7396–7404, https://doi.org/10.1109/TGRS.2016.2601486.

Frajka-Williams, E., and Coauthors, 2019: Atlantic meridional overturning circulation: Observed transport and variability. *Front. Mar. Sci.*, **6**, 260, https://doi.org/10.3389/fmars.2019.00260.

Franz, B. A., I. Cetinic, M. Gao, A. Siegel, and T. K. Westberry, 2024a: Global ocean phytoplankton [in "State of the Climate in 2023"]. *Bull. Amer. Meteor. Soc.*, **105**, S194–S197, https://doi.org/10.1175/BAMS-D-24-0100.1

—— , —— , A. Ibrahim, and A. M. Sayer, 2024b: Anomalous trends in global ocean carbon concentrations following the 2022 eruptions of Hunga Tonga-Hunga Ha'apa. *Commun. Earth Environ.*, **5**, 247, https://doi.org/10.1038/s43247-024-01421-8.

Friedlingstein, P., and Coauthors, 2025: Global carbon budget 2024. *Earth Syst. Sci. Data*, **17**, 965–1039, https://doi.org/10.5194/essd-17-965-2025.

Geider, R. J., H. L. MacIntyre, and T. M. Kana, 1997: Dynamic model of phytoplankton growth and acclimation: Responses of the balanced growth rate and the chlorophyll *a*: Carbon ratio to light, nutrient-limitation and temperature. *Mar. Ecol. Prog. Ser.*, **148**, 187–200, https://doi.org/10.3354/meps148187.

Giglio, D., T. Sukianto, and M. Kuusela, 2025: Global ocean heat content anomalies and ocean heat uptake based on mapping Argo data using local Gaussian processes (4.0.0). Zenodo, accessed 22 January 2025, https://doi.org/10.5281/zenodo.14720478.

Good, S. A., M. J. Martin, and N. A. Rayner, 2013: EN4: Quality controlled ocean temperature and salinity profiles and monthly objective analyses with uncertainty estimates. *J. Geophys. Res. Oceans*, **118**, 6704–6716, https://doi.org/10.1002/2013JC009067.

Gouretski, V., and L. Cheng, 2020: Correction for systematic errors in the global dataset of temperature profiles from mechanical bathythermographs. *J. Atmos. Oceanic Technol.*, **37**, 841–855, https://doi.org/10.1175/JTECH-D-19-0205.1.

Graff, J. R., T. K. Westberry, A. J. Milligan, M. B. Brown, G. Dall'Olmo, V. V Dongen-Vogels, K. M. Reifel, and M. J. Behrenfeld, 2015: Analytical phytoplankton carbon measurements spanning diverse ecosystems. *Deep-Sea Res. I*, **102**, 16–25, https://doi.org/10.1016/j.dsr.2015.04.006.

Hamlington, B. D., C. G. Piecuch, J. T. Reager, H. Chandanpurkar, T. Frederikse, R. S. Nerem, J. T. Fasullo, and S.-H. Cheon, 2020: Origin of interannual variability in global mean sea level. *Proc. Natl. Acad. Sci. USA*, **117**, 13983–13990, https://doi.org/10.1073/pnas.1922190117.

—— ., and Coauthors, 2024: The rate of global sea level rise doubled during the past three decades. *Commun. Earth Environ.*, **5**, 601, https://doi.org/10.1038/s43247-024-01761-5.

Hauck, J., and Coauthors, 2023: The Southern Ocean carbon cycle 1985–2018: Mean, seasonal cycle, trends, and storage. *Global Biogeochem. Cycles*, **37**, e2023GB007848, https://doi.org/10.1029/2023GB007848.

Held, I. M., and B. J. Soden, 2006: Robust responses of the hydrological cycle to global warming. *J. Climate*, **19**, 5686–5699, https://doi.org/10.1175/JCLI3990.1.

Hersbach, H., and Coauthors, 2018: ERA5 hourly data on single levels from 1959 to present. Copernicus Climate Change Service (C3S) Climate Data Store (CDS), accessed 2 January 2024, https://doi.org/10.24381/cds.adbb2d47.

Hobbs, W. R., and J. K. Willis, 2012: Midlatitude North Atlantic heat transport: A time series based on satellite and drifter data. *J. Geophys. Res.*, **117**, C01008, https://doi.org/10.1029/2011JC007039.

Hobday, A. J., and Coauthors, 2016: A hierarchical approach to defining marine heatwaves. *Prog. Oceanogr.*, **141**, 227–238, https://doi.org/10.1016/j.pocean.2015.12.014.

—— , and Coauthors, 2018: Categorizing and naming marine heatwaves. *Oceanography*, **31** (2), 162–173, https://doi.org/10.5670/oceanog.2018.205.

Hu, C., Z. Lee, and B. A. Franz, 2012: Chlorophyll *a* algorithms for oligotrophic oceans: A novel approach based on three-band reflectance difference. *J. Geophys. Res.*, **117**, C01011, https://doi.org/10.1029/2011JC007395.

—— , L. Feng, Z. Lee, B. A. Franz, S. W. Bailey, P. J. Werdell, and C. W. Proctor, 2019: Improving satellite global chlorophyll *a* data products through algorithm refinement and data recovery. *J. Geophys. Res. Oceans*, **124**, 1524–1543, https://doi.org/10.1029/2019JC014941.

Hu, Z.-Z., M. J. McPhaden, B. Huang, J. Zhu, and Y. Liu, 2024: Accelerated warming in the North Pacific since 2013. *Nat. Climate Change*, **14**, 929–931, https://doi.org/10.1038/s41558-024-02088-x.

Huang, B., and Coauthors, 2015: Extended Reconstructed Sea Surface Temperature version 4 (ERSST.v4). Part I: Upgrades and intercomparisons. *J. Climate*, **28**, 911–930, https://doi.org/10.1175/JCLI-D-14-00006.1.

—— , and Coauthors, 2017: Extended Reconstructed Sea Surface Temperature, version 5 (ERSSTv5): Upgrades, validations, and intercomparisons. *J. Climate*, **30**, 8179–8205, https://doi.org/10.1175/JCLI-D-16-0836.1.

—— , and Coauthors, 2020: Uncertainty estimates for sea surface temperature and land surface air temperature in NOAAGlobalTemp version 5. *J. Climate*, **33**, 1351–1379, https://doi.org/10.1175/JCLI-D-19-0395.1.

—— , C. Liu, V. Banzon, E. Freeman, G. Graham, B. Hankins, T. Smith, and H.-M. Zhang, 2021: Improvements of the Daily Optimum Interpolation Sea Surface Temperature (DOISST) version 2.1. *J. Climate*, **34**, 2923–2939, https://doi.org/10.1175/JCLI-D-20-0166.1.

—— , X. Yin, J. A. Carton, L. Chen, G. Graham, P. Hogan, T. Smith, and H.-M. Zhang, 2024: Record high sea surface temperatures in 2023. *Geophys. Res. Lett.*, **51**, e2024GL108369, https://doi.org/10.1029/2024GL108369.

Hughes, T. P., and Coauthors, 2017: Global warming and recurrent mass bleaching of corals. *Nature*, **543**, 373–377, https://doi.org/10.1038/nature21707.

Ishii, M., Y. Fukuda, S. Hirahara, S. Yasui, T. Suzuki, and K. Sato, 2017: Accuracy of global upper ocean heat content estimation expected from present observational data sets. *SOLA*, **13**, 163–167, https://doi.org/10.2151/sola.2017-030.

Jiang, N., C. Zhu, Z.-Z. Hu, M. J. McPhaden, T. Lian, C. Zhou, W. Qian, and D. Chen, 2025: El Niño and sea surface temperature pattern effects lead to historically high global mean surface temperatures in 2023. *Geophys. Res. Lett.*, **52**, e2024GL113733, https://doi.org/10.1029/2024GL113733.

Johns, W. E., S. Elipot, D. A. Smeed, B. Moat, B. King, D. L. Volkov, and R. H. Smith, 2023: Towards two decades of Atlantic Ocean mass and heat transports at 26.5°N. *Philos. Trans. Roy. Soc.*, **A381**, 20220188, https://doi.org/10.1098/rsta.2022.0188.

Johnson, G. C., and J. M. Lyman, 2012: Sea surface salinity [in "State of the Climate in 2011"]. *Bull. Amer. Meteor. Soc.*, **93** (7), S68–S69, S72, https://doi.org/10.1175/2012BAMSStateoftheClimate.1.

—— , and S. G. Purkey, 2024: Refined estimates of global ocean deep and abyssal decadal warming trends. *Geophys. Res. Lett.*, **51**, e2024GL111229, https://doi.org/10.1029/2024GL111229.

—— , J. M. Lyman, J. K. Willis, T. Boyer, J. Antonov, S. A. Good, C. M. Domingues, and N. Bindoff, 2014: Ocean heat content [in "State of the Climate in 2013"]. *Bull. Amer. Meteor. Soc.*, **95** (7), S54–S57, https://doi.org/10.1175/2014BAMSStateoftheClimate.1.

—— , and Coauthors, 2024: Ocean heat content [in "State of the Climate in 2023"]. *Bull. Amer. Meteor. Soc.*, **105** (8), S167–S172, https://doi.org/10.1175/BAMS-D-24-0100.1.

—— , J. Reagan, J. M. Lyman, T. Boyer, C. Schmid, and R. Locarnini, 2020: Salinity [in "State of the Climate in 2019"]. *Bull. Amer. Meteor. Soc.*, **101** (8), S129–S183, https://doi.org/10.1175/BAMS-D-20-0105.1.

—— , and Coauthors, 2024: Ocean heat content [in "State of the Climate in 2023"]. *Bull. Amer. Meteor. Soc.*, **105** (8), S169–S172, https://doi.org/10.1175/BAMS-D-24-0100.1.

Kato, S., and Coauthors, 2018: Surface irradiances of edition 4.0 Clouds and the Earth's Radiant Energy System (CERES) Energy Balanced and Filled (EBAF) data product. *J. Climate*, **31**, 4501–4527, https://doi.org/10.1175/JCLI-D-17-0523.1.

Kendon, M., and Coauthors, 2024: State of the UK climate 2023. *Int. J. Climatol.*, **44** (S1), 1–117, https://doi.org/10.1002/joc.8553.

Kennedy, J. J., N. A. Rayner, C. P. Atkinson, and R. E. Killick, 2019: An ensemble data set of sea surface temperature change from 1850: The Met Office Hadley Centre HadSST.4.0.0.0 data set. *J. Geophys. Res. Atmos.*, **124**, 7719–7763, https://doi.org/10.1029/2018JD029867.

Keppler, L., P. Landschützer, S. K. Lauvset, and N. Gruber, 2023: Recent trends and variability in the oceanic storage of dissolved inorganic carbon. *Global Biogeochem. Cycles*, **37**, e2022GB007677, https://doi.org/10.1029/2022GB007677.

Kugusheva, A., H. Bull, E. Moschos, A. Ioannou, B. Le Vu, and A. Stegner, 2024: Ocean satellite data fusion for high-resolution surface current maps. *Remote Sens.*, **16**, 1182, https://doi.org/10.3390/rs16071182.

Kumar, P., B. Hamlington, S.-H. Cheon, W. Han, and P. Thompson, 2020: 20th century multivariate Indian Ocean regional sea level reconstruction. *J. Geophys. Res. Oceans*, **125**, e2020JC016270, https://doi.org/10.1029/2020JC016270.

Lan, X., P. Tans, and K. Thoning, 2023: NOAA greenhouse gas marine boundary layer reference: CO_2. NOAA Global Monitoring Laboratory, accessed 15 January 2025, https://doi.org/10.15138/DVNP-F961.

Landschützer, P., N. Gruber, D. C. E. Bakker, U. Schuster, S. Nakaoka, M. R. Payne, T. P. Sasse, and J. Zeng, 2013: A neural network-based estimate of the seasonal to inter-annual variability of the Atlantic Ocean carbon sink. *Biogeosciences*, **10**, 7793–7815, https://doi.org/10.5194/bg-10-7793-2013.

—— , —— , —— , and —— , 2014: Recent variability of the global ocean carbon sink. *Global Biogeochem. Cycles*, **28**, 927–949, https://doi.org/10.1002/2014GB004853.

Lauvset, S. K., and Coauthors, 2016: A new global interior ocean mapped climatology: The 1° × 1° GLODAP version 2. *Earth Syst. Sci. Data*, **8**, 325–340, https://doi.org/10.5194/essd-8-325-2016.

Leuliette, E. W., and J. K. Willis, 2011: Balancing the sea level budget. *Oceanography*, **24** (2), 122–129, https://doi.org/10.5670/oceanog.2011.32.

Le Vine, D. M., E. P. Dinnat, G. S. E. Lagerloef, P. de Matthaeis, S. Abraham, C. Utku, and H. Kao, 2014: Aquarius: Status and recent results. *Radio Sci.*, **49**, 709–720, https://doi.org/10.1002/2014RS005505.

Levitus, S., and Coauthors, 2012: World ocean heat content and thermosteric sea level change (0–2000 m), 1955. *Geophys. Res. Lett.*, **39**, L10603, https://doi.org/10.1029/2012GL051106.

Li, G., L. Cheng, J. Zhu, K. Trenberth, M. Mann, and J. Abraham, 2020: Increasing ocean stratification over the past half-century. *Nat. Climate Change*, **10**, 1116–1123, https://doi.org/10.1038/s41558-020-00918-2.

Li, L., R. W. Schmitt, C. C. Ummenhofer, and K. B. Karnauskas, 2016: North Atlantic salinity as a predictor of Sahel rainfall. *Sci. Adv.*, **2**, e1501588, https://doi.org/10.1126/sciadv.1501588.

Li, S., T. Wahl, A. Barroso, S. Coats, S. Dangendorf, C. Piecuch, Q. Sun, P. Thompson, and L. Liu, 2022: Contributions of different sea-level processes to high-tide flooding along the U.S. Coastline. *J. Geophys. Res. Oceans*, **127**, e2021JC018276, https://doi.org/10.1029/2021JC018276.

Loeb, N. G., and Coauthors, 2018: Clouds and the Earth's Radiant Energy System (CERES) Energy Balanced and Filled (EBAF) Top-of-Atmosphere (TOA) edition-4.0 data product. *J. Climate*, **31**, 895–918, https://doi.org/10.1175/JCLI-D-17-0208.1.

—— , G. C. Johnson, T. J. Thorsen, J. M. Lyman, F. G. Rose, and S. Kato, 2021: Satellite and ocean data reveal marked increase in Earth's heating rate. *Geophys. Res. Lett.*, **48**, e2021GL093047, https://doi.org/10.1029/2021GL093047.

Long, X., M. J. Widlansky, F. Schloesser, P. R. Thompson, H. Annamalai, M. A. Merrifield, and H. Yoon, 2020: Higher Sea Levels at Hawaii Caused by Strong El Niño and Weak Trade Winds. *J. Climate*, **33**, 3037–3059, https://doi.org/10.1175/JCLI-D-19-0221.1.

Lumpkin, R., G. Goni, and K. Dohan, 2012: Surface currents [in "State of the Climate in 2011"]. *Bull. Amer. Meteor. Soc.*, **93** (7), S75–S78, https://doi.org/10.1175/2012BAMSStateoftheClimate.1.

—— , F. Bringas, and R. Perez, 2024: Surface currents [in "State of the Climate in 2023"]. *Bull. Amer. Meteor. Soc.*, **105** (8), S23–S27, https://doi.org/10.1175/BAMS-D-24-0100.1.

Lyman, J. M., and G. C. Johnson, 2014: Estimating global ocean heat content changes in the upper 1800 m since 1950 and the influence of climatology choice. *J. Climate*, **27**, 1946–1958, https://doi.org/10.1175/JCLI-D-12-00752.1.

—— , and G. C. Johnson, 2023: Global high-resolution random forest regression maps of ocean heat content anomalies using in situ and satellite data. *J. Atmos. Oceanic Technol.*, **40**, 575–586, https://doi.org/10.1175/JTECH-D-22-0058.1.

Maritorena, S., O. H. Fanton d'Andon, A. Mangin, and D. A. Siegel, 2010: Merged satellite ocean color data products using a bio-optical model: Characteristics, benefits and issues. *Remote Sens. Environ.*, **114**, 1791–1804, https://doi.org/10.1016/j.rse.2010.04.002.

Martin, S. A., G. E. Manucharyan, and P. Klein, 2024: Deep learning improves global satellite observations of ocean eddy dynamics. *Geophys. Res. Lett.*, **51**, e2024GL110059, https://doi.org/10.1029/2024GL110059.

McCarthy, G. D., and Coauthors, 2015: Measuring the Atlantic meridional overturning circulation at 26°N. *Prog. Oceanogr.*, **130**, 91–111, https://doi.org/10.1016/j.pocean.2014.10.006.

McKinna, L. I. W, P. J. Werdell, and B. A. Franz, 2016: An update on NASA's generalized inherent optical properties algorithm framework. *Proc. Ocean Optics XXIII*, Victoria, B.C., Canada, The Oceanography Society.

—— , I. Cetinic, and J. Werdell, 2024: The status of NASA IOP data products for the PACE era. *Ocean Sciences Meeting 2024*, New Orleans, LA, Amer. Geophys. Union, OT24F-156.

McPhaden, M. J., K. J. Connell, G. R. Foltz, R. C. Perez, and K. Grissom, 2023: Tropical ocean observations for weather and climate: A decadal overview of the Global Tropical Moored Buoy Array. *Oceanography*, **36** (2–3), 32–43, https://doi.org/10.5670/oceanog.2023.211.

Meinen, C. S., M. O. Baringer, and R. F. Garcia, 2010: Florida Current transport variability: An analysis of annual and longer-period signals. *Deep-Sea Res. I*, **57**, 835–846, https://doi.org/10.1016/j.dsr.2010.04.001.

—— , and Coauthors, 2013: Temporal variability of the meridional overturning circulation at 34.5°S: Results from two pilot boundary arrays in the South Atlantic. *J. Geophys. Res. Oceans*, **118**, 6461–6478, https://doi.org/10.1002/2013JC009228.

—— , and Coauthors, 2018: Meridional overturning circulation transport variability at 34.5°S during 2009–2017: Baroclinic and barotropic flows and the dueling influence of the boundaries. *Geophys. Res. Lett.*, **45**, 4180–4188, https://doi.org/10.1029/2018GL077408.

Mishonov, A. V., and Coauthors, 2024: World Ocean Database 2023. NOAA Atlas NESDIS 97, 206 pp., https://doi.org/10.25923/z885-h264.

Moat, B. I., and Coauthors, 2020: Pending recovery in the strength of the meridional overturning circulation at 26°N. *Ocean Sci.*, **16**, 863–874, https://doi.org/10.5194/os-16-863-2020.

—— , and Coauthors, 2024: Atlantic meridional overturning circulation observed by the RAPID-MOCHA-WBTS (RAPID-Meridional Overturning Circulation and Heatflux Array-Western Boundary Time Series) array at 26N from 2004 to 2023 (v2023.1). British Oceanographic Data Centre, Natural Environment Research Council, accessed 17 January 2025, https://doi.org/10.5285/223b34a3-2dc5-c945-e063-7086abc0f274.

Nerem, R. S., D. P. Chambers, E. W. Leuliette, G. T. Mitchum, and B. S. Giese, 1999: Variations in global mean sea level associated with the 1997–1998 ENSO event: Implications for measuring long term sea level change. *Geophys. Res. Lett.*, **26**, 3005–3008, https://doi.org/10.1029/1999GL002311.

—— , B. D. Beckley, J. T. Fasullo, B. D. Hamlington, D. Masters, and G. T. Mitchum, 2018: Climate-change-driven accelerated sea-level rise detected in the altimeter era. *Proc. Natl. Acad. Sci. USA*, **115**, 2022–2025, https://doi.org/10.1073/pnas.1717312115.

Oliver, E. C. J., J. A. Benthuysen, S. Darmaraki, M. G. Donat, A. J. Hobday, N. J. Holbrook, R. W. Schlegel, and A. Sen Gupta, 2021: Marine heatwaves. *Ann. Rev. Mar. Sci.*, **13**, 313–342, https://doi.org/10.1146/annurev-marine-032720-095144.

O'Reilly, J. E., and P. J. Werdell, 2019: Chlorophyll algorithms for ocean color sensors - OC4, OC5 & OC6. *Remote Sens. Environ.*, **229**, 32–47, https://doi.org/10.1016/j.rse.2019.04.021.

Pahlevan, N., B. Smith, C. Binding, D. Gurlin, L. Li, M. Bresciani, and C. Giardino, 2021: Hyperspectral retrievals of phytoplankton absorption and chlorophyll-*a* in inland and nearshore coastal waters. *Remote Sens. Environ.*, **253**, 112200, https://doi.org/10.1016/j.rse.2020.112200.

Palmer, M. D., K. Haines, S. F. B. Tett, and T. J. Ansell, 2007: Isolating the signal of ocean global warming. *Geophys. Res. Lett.*, **34**, L23610, https://doi.org/10.1029/2007GL031712.

Purkey, S. G., and G. C. Johnson, 2010: Warming of global abyssal and deep Southern Ocean waters between the 1990s and 2000s: Contributions to global heat and sea level rise budgets. *J. Climate*, **23**, 6336–6351, https://doi.org/10.1175/2010JCLI3682.1.

Qiu, B., and S. Chen, 2021: Revisit of the occurrence of the Kuroshio large meander south of Japan. *J. Phys. Oceanogr.*, **51**, 3679–3694, https://doi.org/10.1175/JPO-D-21-0167.1.

—— , —— , N. Schneider, E. Oka, and S. Sugimoto, 2020: On the reset of the wind-forced decadal Kuroshio extension variability in late 2017. *J. Climate*, **33**, 10813–10828, https://doi.org/10.1175/JCLI-D-20-0237.1.

Rayner, N. A., D. E. Parker, E. B. Horton, C. K. Folland, L. V. Alexander, D. P. Rowell, E. C. Kent, and A. Kaplan, 2003: Global analyses of sea surface temperature, sea ice, and night marine air temperature since the late nineteenth century. *J. Geophys. Res.*, **108**, 4407, https://doi.org/10.1029/2002JD002670.

Reagan, J., T. Boyer, C. Schmid, and R. Locarnini, 2022: State of the Climate in 2021. *Bull. Amer. Meteor. Soc.*, **103** (8), S1–S465, https://doi.org/10.1175/2022BAMSStateoftheClimate.1.

—— , —— , —— , and —— , 2023: Subsurface salinity [in "State of the Climate in 2022"]. *Bull. Amer. Meteor. Soc.*, **104** (9), S165–S167, https://doi.org/10.1175/BAMS-D-23-0076.2.

—— , —— , —— , and —— , 2024: Subsurface salinity [in "State of the Climate in 2023"]. *Bull. Amer. Meteor. Soc.*, **105** (8), S175–S187, https://doi.org/10.1175/BAMS-D-24-0100.1.

Reagan, J. R., and Coauthors, 2024: Salinity. Vol. 2, World Ocean Atlas 2023, NOAA Atlas NESDIS 90, 52 pp., https://doi.org/10.25923/70qt-9574.

Regnier, P., L. Resplandy, R. G. Najjar, and P. Ciais, 2022: The land-to-ocean loops of the global carbon cycle. *Nature*, **603**, 401–410, https://doi.org/10.1038/s41586-021-04339-9.

Ren, L., K. Speer, and E. P. Chassignet, 2011: The mixed layer salinity budget and sea ice in the Southern Ocean. *J. Geophys. Res.*, **116**, C08031, https://doi.org/10.1029/2010JC006634.

Riser, S. C., and Coauthors, 2016: Fifteen years of ocean observations with the global Argo array. *Nat. Climate Change*, **6**, 145–153, https://doi.org/10.1038/nclimate2872.

Rödenbeck, C., and Coauthors, 2015: Data-based estimates of the ocean carbon sink variability – First results of the Surface Ocean pCO_2 Mapping intercomparison (SOCOM). Biogeosciences, **12**, 7251–7278, https://doi.org/10.5194/bg-12-7251-2015.

Roemmich, D., and J. Gilson, 2009: The 2004–2008 mean and annual cycle of temperature, salinity, and steric height in the global ocean from the Argo Program. *Prog. Oceanogr.*, **82**, 81–100, https://doi.org/10.1016/j.pocean.2009.03.004.

Schlesinger, M. E., and N. Ramankutty, 1994: An oscillation in the global climate system of period 65–70 years. *Nature*, **367**, 723–726, https://doi.org/10.1038/367723a0.

Schmidtko, S., G. C. Johnson, and J. M. Lyman, 2013: MIMOC: A global monthly isopycnal upper-ocean climatology with mixed layers. *J. Geophys. Res. Oceans*, **118**, 1658–1672, https://doi.org/10.1002/jgrc.20122.

Schmitt, R. W., 1995: The ocean component of the global water cycle. *Rev. Geophys.*, **33**, 1395–1409, https://doi.org/10.1029/95RG00184.

Siegel, D. A., S. Maritorena, N. B. Nelson, M. J. Behrenfeld, and C. R. McClain, 2005: Colored dissolved organic matter and its influence on the satellite-based characterization of the ocean biosphere. *Geophys. Res. Lett.*, **32**, L20605, https://doi.org/10.1029/2005GL024310.

——, and Coauthors, 2013: Regional to global assessments of phytoplankton dynamics from the SeaWiFS mission. *Remote Sens. Environ.*, **135**, 77–91, https://doi.org/10.1016/j.rse.2013.03.025.

——, T. DeVries, I. Cetinić, and K. M. Bisson, 2023: Quantifying the ocean's biological pump and its carbon cycle impacts on global scales. *Ann. Rev. Mar. Sci.*, **15**, 329–356, https://doi.org/10.1146/annurev-marine-040722-115226.

Skliris, N., R. Marsh, S. A. Josey, S. A. Good, C. Liu, and R. P. Allan, 2014: Salinity changes in the World Ocean since 1950 in relation to changing surface freshwater fluxes. *Climate Dyn.*, **43**, 709–736, https://doi.org/10.1007/s00382-014-2131-7.

Smeed, D. A., and Coauthors, 2018: The North Atlantic Ocean is in a state of reduced overturning. *Geophys. Res. Lett.*, **45**, 1527–1533, https://doi.org/10.1002/2017GL076350.

Stackhouse, P. W., D. P. Kratz, G. R. McGarragh, S. K. Gupta, and E. B. Geier, 2006: Fast Longwave and Shortwave Radiative Flux (FLASHFlux) products from CERES and MODIS measurements. *Proc. 12th Conf. on Atmospheric Radiation*, Amer. Meteor. Soc., P1.10, https://ams.confex.com/ams/pdfpapers/113479.pdf.

Sweet, W. V., J. Park, J. J. Marra, C. Zervas, and S. Gill, 2014: Sea level rise and nuisance flood frequency changes around the United States. NOAA Tech. Rep. NOS CO-OPS 073, 66 pp.

Sweet, W. V., A. S. Genz, M. Menendez, J. J. Marra, and J. Obeysekera, 2024: Implications of variability and trends in coastal extreme water levels. *Geophys. Res. Lett.*, **51**, e2024GL108864, https://doi.org/10.1029/2024GL108864.

Tamisiea, M. E., and J. X. Mitrovica, 2011: The moving boundaries of sea level change: Understanding the origins of geographic variability. *Oceanography*, **24** (2), 24–39, https://doi.org/10.5670/oceanog.2011.25.

Tan, W., Z.-Z. Hu, M. J. McPhaden, C. Zhu, X. Li, and Y. Liu, 2024: On the divergent evolution of ENSO after the coastal El Niños in 2017 and 2023. *Geophys. Res. Lett.*, **51**, e2024GL108198, https://doi.org/10.1029/2024GL108198.

Tuchen, F. P., R. C. Perez, G. R. Foltz, M. J. McPhaden, and R. Lumpkin, 2024: Strengthening of the equatorial Pacific upper-ocean circulation over the past three decades. *J. Geophys. Res. Oceans*, **129**, e2024JC021343, https://doi.org/10.1029/2024JC021343.

Twedt, K., N. Lei, X. Xiong, A. Angal, S. Li, T. Chang, and J. Sun, 2022: On-orbit calibration and performance of NOAA-20 VIIRS reflective solar bands. *IEEE Trans. Geosci. Remote Sens.*, **60**, 1–13, https://doi.org/10.1109/TGRS.2021.3108970.

Volkov, D. L., S.-K. Lee, R. Domingues, H. Zhang, and M. Goes, 2019: Interannual sea level variability along the southeastern seaboard of the United States in relation to the gyre-scale heat divergence in the North Atlantic. *Geophys. Res. Lett.*, **46**, 7481–7490, https://doi.org/10.1029/2019GL083596.

——, and Coauthors, 2021: Meridional overturning circulation and heat transport in the Atlantic Ocean [in "State of the Climate in 2020"]. *Bull. Amer. Meteor. Soc.*, **102**, S176–S179, https://doi.org/10.1175/BAMS-D-21-0083.1.

——, K. Zhang, W. E. Johns, J. K. Willis, W. Hobbs, M. Goes, H. Zhang, and D. Menemenlis, 2023: Atlantic meridional overturning circulation increases flood risk along the United States southeast coast. *Nat. Commun.*, **14**, 5095, https://doi.org/10.1038/s41467-023-40848-z.

——, R. H. Smith, R. F. Garcia, D. A. Smeed, B. I. Moat, W. E. Johns, and M. O. Baringer, 2024a: Florida Current transport observations reveal four decades of steady state. *Nat. Commun.*, **15**, 7780, https://doi.org/10.1038/s41467-024-51879-5.

——, and Coauthors, 2024b: Meridional overturning circulation and heat transport in the Atlantic Ocean [in "State of the Climate in 2023"]. *Bull. Amer. Meteor. Soc.*, **105** (8), S191–S193, https://doi.org/10.1175/BAMS-D-24-0100.1.

von Schuckmann, K., and Coauthors, 2023: Heat stored in the Earth system 1960–2020: Where does the energy go? *Earth Syst. Sci. Data*, **15**, 1675–1709, https://doi.org/10.5194/essd-15-1675-2023.

Von Storch, H., and F. W. Zwiers, 1999: *Statistical Analysis in Climate Research*. Cambridge University Press, 484 pp.

Wahl, T., F. M. Calafat, and M. E. Luther, 2014: Rapid changes in the seasonal sea level cycle along the US Gulf coast from the late 20th century. *Geophys. Res. Lett.*, **41**, 491–498, https://doi.org/10.1002/2013GL058777.

Walsh, K. J. E., and Coauthors, 2016: Tropical cyclones and climate change. *Wiley Interdiscip. Rev.: Climate Change*, **7**, 65–89, https://doi.org/10.1002/wcc.371.

Wang, M., S.-P. Xie, H. Sasaki, M. Nonaka, and Y. Du, 2024: Intensification of Pacific tropical instability waves over the recent three decades. *Nat. Climate Change*, **14**, 163–170, https://doi.org/10.1038/s41558-023-01915-x.

Wanninkhof, R., 2014: Relationship between wind speed and gas exchange over the ocean revisited. *Limnol. Oceanogr. Methods*, **12**, 351–362, https://doi.org/10.4319/lom.2014.12.351.

Werdell, P. J., and L. I. McKinna, 2019: Sensitivity of inherent optical properties from ocean reflectance inversion models to satellite instrument wavelength suites. *Front. Earth Sci.*, **7**, 54, https://doi.org/10.3389/feart.2019.00054.

——, and Coauthors, 2013: Generalized ocean color inversion model for retrieving marine inherent optical properties. *Appl. Opt.*, **52**, 2019–2037, https://doi.org/10.1364/AO.52.002019.

—— , and Coauthors, 2019: The Plankton, aerosol, cloud, ocean ecosystem mission: Status, science, advances. *Bull. Amer. Meteor. Soc.*, **100**, 1775–1794, https://doi.org/10.1175/BAMS-D-18-0056.1.

—— , J. O'Reilly, C. Hu, L. Feng, Z. Lee, B. Franz, S. Bailey, and C. Proctor, 2023: Chlorophyll *a*. NASA Algorithm Publication Tool, v1.1, accessed 22 January 2025, https://doi.org/10.5067/JCQB8QALDOYD.

Westberry, T. K., P. Schultz, M. J. Behrenfeld, J. P. Dunne, M. R. Hiscock, S. Maritorena, J. L. Sarmiento, and D. A. Siegel, 2016: Annual cycles of phytoplankton biomass in the subarctic Atlantic and Pacific Ocean. *Global Biogeochem. Cycles*, **30**, 175–190, https://doi.org/10.1002/2015GB005276.

Widlansky, M. J., A. Timmermann, S. McGregor, M. F. Stuecker, and W. Cai, 2014: An interhemispheric tropical sea level seesaw due to El Niño Taimasa. *J. Climate*, **27**, 1070–1081, https://doi.org/10.1175/JCLI-D-13-00276.1.

Wiese, D. N., D.-N. Yuan, C. Boening, F. W. Landerer, and M. M. Watkins, 2022: JPL GRACE and GRACE-FO Mascon ocean, ice, and hydrology equivalent HDR water height RL06.1M CRI filtered version 3.0. PO.DAAC, accessed 13 February 2024, https://doi.org/10.5067/TEMSC-3MJ62.

Willis, J., and W. Hobbs, 2025: Atlantic meridional overturning circulation near 41N from altimetry and argo observations (2025_01). Zenodo, accessed 18 January 2025, https://doi.org/10.5281/zenodo.14681441.

—— , 2010: Can in situ floats and satellite altimeters detect long-term changes in Atlantic Ocean overturning? *Geophys. Res. Lett.*, **37**, L06602, https://doi.org/10.1029/2010GL042372.

Wolter, K., and M. S. Timlin, 1998: Measuring the strength of ENSO events: How does 1997/98 rank? *Weather*, **53**, 315–324, https://doi.org/10.1002/j.1477-8696.1998.tb06408.x.

Wüst, G., 1936: Oberflächensalzgehalt, Verdunstung und Niederschlag auf dem Weltmeere. Länderkundliche Forschung: Festschrift zur Vollendung des sechzigsten Lebensjahres Norbert Krebs, J. Engelhorns Nachfahren, 347–359.

Xie, P., and Coauthors, 2014: An in situ—satellite blended analysis of global sea surface salinity. *J. Geophys. Res. Oceans*, **119**, 6140–6160, https://doi.org/10.1002/2014JC010046.

Yang, J., and K. Chen, 2025: Profound changes in the seasonal cycle of sea level along the United States mid-Atlantic coast. *Geophys. Res. Lett.*, **52**, e2024GL112273, https://doi.org/10.1029/2024GL112273.

Yin, X., B. Huang, J. A. Carton, L. Chen, G. Graham, C. Liu, T. Smith, and H.-M. Zhang, 2024: The 1991–2020 sea surface temperature normals. *Int. J. Climatol.*, **44**, 668–685, https://doi.org/10.1002/joc.8350.

Yu, L., 2011: A global relationship between the ocean water cycle and near-surface salinity. *J. Geophys. Res.*, **116**, C10025, https://doi.org/10.1029/2010JC006937.

—— , 2019: Global air-sea fluxes of heat, fresh water, and momentum: Energy budget closure and unanswered questions. *Ann. Rev. Mar. Sci.*, **11**, 227–248, https://doi.org/10.1146/annurev-marine-010816-060704.

—— , and R. A. Weller, 2007: Objectively analyzed air–sea heat fluxes for the global ice-free oceans (1981–2005). *Bull. Amer. Meteor. Soc.*, **88**, 527–540, https://doi.org/10.1175/BAMS-88-4-527]